



# **Control of aberrant TDP-43 phase transitions by the selective autophagy machinery**

**Dissertation**

Zur Erlangung des Grades

“Doktor der Naturwissenschaften“

(Dr. rer. nat.)

Am Fachbereich Biologie

der Johannes Gutenberg-Universität Mainz

**Yongwon Suk**

Geboren am 10.03.1993 in Bad Cannstatt

Oktober 2025

Dekan: Prof. Dr. Eckhard Thines

1<sup>st</sup> examiner: Prof. Dr. Dorothee Dormann

2<sup>nd</sup> examiner: Prof Dr. Helle Ulrich



## **Declaration**

I, Yongwon Suk, declare that the work presented in this thesis is my own. I confirm that any information or data obtained from other sources is appropriately indicated in the thesis



## Abstract

Neurodegenerative diseases such as amyotrophic lateral sclerosis (ALS) and frontotemporal dementia (FTD) converge on the failure of neuronal proteostasis. A central hallmark of these diseases is the cytoplasmic aggregation of TAR DNA binding protein of 43 kDa (TDP-43), a ubiquitously expressed RNA-binding protein whose physiological role in RNA processing and stress responses is essential for neuronal health. How cells normally surveil and clear aberrant TDP-43 assemblies, and how this fails in disease, remains insufficiently understood.

In the first part of this thesis (Part A), I investigated how proteasome dysfunction precipitates TDP-43 pathology and how the cell responds to such assemblies. Using stable cell lines expressing GFP-tagged TDP-43 variants, I found that acute proteasome inhibition rapidly drives the condensation of cytosolic TDP-43, in particular C-terminal fragments (CTFs) of TDP-43, into liquid-like puncta that progressively “age” into undynamic aggregate-like structures that become partially detergent-insoluble and acquire hallmarks of pathological TDP-43 inclusions, such as ubiquitination and S409/410 phosphorylation. TDP-43 CTF condensates induced by proteasome inhibition were distinct from stress granules or aggresomes, indicating a unique condensation pathway intrinsic to TDP-43 CTFs. Live-cell experiments revealed that these assemblies are not irreversible endpoints but can be cleared upon washout of the proteasome inhibitor. Their clearance required both Hsp70 chaperone activity, which likely fragments and remodels TDP-43 aggregates, and the autophagy–lysosome system, which engulfs and degrades them. Functional perturbations uncovered distinct contributions: p62/SQSTM1 promotes TDP-43 CTF condensate formation by clustering ubiquitylated TDP-43 species, whereas WIPI2 is essential for phagophore initiation and TDP-43 CTF clearance. Proximity proteomics mapped this sequence of events at molecular resolution, revealing a state-dependent hand-off: diffuse TDP-43 CTF species engage the proteasome, while condensed intermediates recruit autophagy factors including p62, NBR1, WIPI2, and VCP. Immunohistochemistry in FTLD-TDP brain tissue confirmed p62 co-localizes with TDP-43 inclusions and revealed NBR1 as a new aggregating protein in FTLD-TDP patients, underscoring the disease relevance of this pathway. Together, Part A establishes that proteasome failure is sufficient to trigger a regulated condensation of TDP-43, and that successful resolution depends on a coordinated chaperone–autophagy program.

In the second part of this thesis (Part B), I examined the role of UBQLN2, a proteostasis factor genetically linked to ALS/FTD. I optimized its purification and demonstrated that UBQLN2 enhances RNA binding of both TDP-43 and FUS and modulates FUS phase separation behavior. These findings suggest that UBQLN2 might have a dual protective role: stabilizing the RNA-bound state of RNA-binding proteins to raise the threshold for aberrant condensation, and routing ubiquitylated clients toward degradation once condensates form. Disease-linked UBQLN2 mutations may impair both protective mechanisms, thereby accelerating the accumulation of pathological TDP-43 and FUS assemblies.

Taken together, this work outlines a mechanistic framework that helps to explain how TDP-43 pathology emerges from proteasome dysfunction and progresses through a liquid-to-amorphous trajectory that can still be cleared if chaperones and autophagy engage efficiently. It also positions UBQLN2 as a critical modulator at the intersection of phase behavior and proteostasis routing. These insights highlight key molecular checkpoints: proteasomal throughput, chaperone licensing, and autophagic capture, where therapeutic interventions could possibly reinforce proteostasis mechanisms and thus delay disease progression in ALS and FTD.



## Zusammenfassung

Neurodegenerative Erkrankungen wie Amyotrophic lateral sclerosis (ALS) und Frontotemporal Dementia (FTD) konvergieren auf dem Versagen der neuronalen Proteostase. Ein zentrales Kennzeichen dieser Erkrankungen ist die zytoplasmatische Aggregation des TAR-DNA-binding Protein of 43 kDa (TDP-43), eines ubiquitär exprimierten RNA-bindenden Proteins, dessen physiologische Rolle in der RNA-Prozessierung und in Stressantworten für die neuronale Gesundheit essenziell ist. Wie Zellen normalerweise fehlerhafte TDP-43-Assemblies überwachen und beseitigen und wie dieser Prozess in der Krankheit fehlschlägt ist bislang nur unzureichend verstanden.

Im ersten Teil dieser Dissertation (Teil A) habe ich untersucht, wie eine Proteasom-Dysfunktion TDP-43-Pathologie auslöst und wie die Zelle auf solche Assemblies reagiert. Mithilfe stabiler Zelllinien, die GFP-markierte TDP-43-Varianten exprimieren, konnte ich zeigen, dass eine akute Proteasom-Inhibition rasch zur Kondensation von zytosolischem TDP-43, insbesondere C-terminalen Fragmenten (CTFs) von TDP-43, in „liquid-like“ Punktate führt, die sich schrittweise zu undynamischen, aggregatähnlichen Strukturen „verfestigen“. Diese werden teilweise detergens unlöslich und weisen charakteristische Merkmale pathologischer TDP-43-Inklusionen auf, darunter Ubiquitinierung und Phosphorylierung an S409/410. Durch Proteasom-Inhibition induzierte TDP-43-CTF-Kondensate unterschieden sich sowohl von Stress granula als auch von Aggresomen und zeigten damit einen eigenständigen Kondensationsweg, der den TDP-43-CTFs spezifisch ist. Live-Cell-Experimente belegten, dass es sich hierbei nicht um irreversible Endpunkte handelt, sondern dass diese Assemblies nach Absetzen des Proteasom-Inhibitors wieder abgebaut werden können. Ihr Abbau erforderte sowohl die Aktivität des Hsp70-Chaperons, das vermutlich TDP-43-Aggregate fragmentiert und umgestaltet, als auch das Autophagie-Lysosom-System, das sie umschließt und abbaut. Funktionelle Störungen verdeutlichten dabei unterschiedliche Beiträge: p62/SQSTM1 fördert die Bildung von TDP-43-CTF-Kondensaten durch Clustering ubiquitiniertes TDP-43-Varianten, während WIPI2 für die Initiierung des Phagophors und die Clearance von TDP-43-CTFs essenziell ist. Proximity-Proteomic zeigte diese Abfolge von Ereignissen auf molekularer Ebene und offenbarte ein zustandsabhängiges „Hand-off“: Diffuse TDP-43-CTF-Varianten interagieren mit dem Proteasom, während kondensierte

Zwischenformen Autophagie-Faktoren wie p62, NBR1, WIPI2 und VCP rekrutieren. Immunhistochemie in FTLD-TDP-Gehirngewebe bestätigte, dass p62 mit TDP-43-Inklusionen kolokalisiert, und identifizierte NBR1 als neues aggregierendes Protein in FTLD-TDP-Patienten, was die Krankheitsrelevanz dieses Weges unterstreicht. Zusammengefasst zeigt Teil A, dass Proteasom-Versagen ausreicht, um eine regulierte Kondensation von TDP-43 auszulösen, und dass eine erfolgreiche Auflösung von einem koordinierten Chaperon–Autophagie-Programm abhängt.

Im zweiten Teil dieser Dissertation (Teil B) untersuchte ich die Rolle von UBQLN2, eines Proteostase-Faktors, der genetisch mit ALS/FTD verknüpft ist. Ich optimierte die Aufreinigung und konnte zeigen, dass UBQLN2 die RNA-Bindung sowohl von TDP-43 als auch von FUS verstärkt und das Phase Separation Verhalten von FUS moduliert. Diese Befunde deuten darauf hin, dass UBQLN2 eine doppelte Schutzfunktion haben könnte: Zum einen stabilisiert es den RNA-gebundenen Zustand RNA-bindender Proteine, wodurch die Schwelle für aberrante Kondensation erhöht wird, zum anderen leitet es ubiquitinierte Substrate zum Abbau weiter, sobald sich Kondensate gebildet haben. Krankheitsassoziierte UBQLN2-Mutationen könnten beide Schutzmechanismen beeinträchtigen und damit die Akkumulation pathologischer TDP-43- und FUS-Assemblies beschleunigen.

Insgesamt zeigt diese Arbeit ein mechanistisches Rahmenmodell, das erklärt, wie TDP-43-Pathologie aus einer Proteasom-Dysfunktion hervorgeht und sich über einen flüssig-zu-amorphen Verlauf entwickelt, die jedoch noch abgebaut werden kann, wenn Chaperone und Autophagie effizient eingreifen. Gleichzeitig positioniert sie UBQLN2 als einen kritischen Modulator an der Schnittstelle zwischen Phasenverhalten und Proteostase-Routing. Diese Erkenntnisse heben zentrale molekulare Kontrollpunkte hervor: Proteasom-Durchsatz, Chaperon-Lizenzierung und autophagische Erfassung, an denen therapeutische Interventionen die Proteostase-Mechanismen verstärken und damit den Krankheitsverlauf bei ALS und FTD verzögern könnten.



# Contents

1. Abbreviations .....	1
2. Introduction:.....	4
2.1 From Neuron Vulnerability to Proteinopathy.....	4
2.1.1 Epidemiology and Spectrum of ALS/FTD .....	4
2.1.2 Shared Molecular Hallmarks of ALS/FTD .....	6
2.2 Proteostasis Machinery .....	8
2.2.1 The Ubiquitin Conjugation Cascade: Writers, Readers, and Erasers .....	9
2.2.2 The 26S Proteasome: Architecture and Substrate Processing .....	10
2.2.3 Macroautophagy, Microautophagy, and Chaperone-Mediated Autophagy .....	12
2.2.4 Selective Autophagy: Aggrephagy, Mitophagy, and More .....	14
2.2.5 UPS–Autophagy Crosstalk and Stress-Response Switches .....	16
2.2.6 Chaperones and Disaggregase Function .....	17
2.3 Quality-Control Factors Linked to ALS/FTD .....	19
2.3.1 Genetic mutations linked to ALS/FTD .....	19
2.3.2 p62/SQSTM1, NBR1, OPTN, TAX1BP1, UBQLN2 and Other Important Factors .....	20
2.4 Phase Separation: From Physiology to Pathology .....	22
2.4.1 Biophysics of LLPS and Prion-Like Low-Complexity Domains .....	22
2.4.2 Stress Granules and other Membraneless Organelles .....	23
2.4.3 Maturation Trajectories: Liquid → Gel → Amyloid .....	24
2.4.4 Cellular Sensors of Aberrant Condensates.....	25
2.5 RNA-Binding Proteins in ALS/FTD .....	27
2.5.1 TDP-43: nuclear functions vs Cytosolic functions.....	27
2.5.2 ALS/FTD linked TDP-43: Toxic Gain vs Loss of Function.....	29
2.5.3 TDP-43 Domain Organization, Post-translational Modifications, And Disease-Associated Properties. ....	31
2.5.4 Proteolytic Cleavage and C-Terminal Fragments of TDP-43 .....	34
2.5.5 Chaperones in TDP-43 Pathology .....	35
2.5.6 FUS: similarities and differences to TDP-43 .....	36
2.5.7 Comparative pathology of TDP-43 versus FUS inclusions .....	37
2.6 UBQLN2 at the UPS–Autophagy Interface .....	37
2.6.1 Shuttle Function: Proteasome Escort vs. Autophagy Adaptor .....	37

2.6.2 ALS/FTD-Linked UBQLN2 Mutations: Toxic Gain vs. Loss of Function ....	38
2.6.3 UBQLN2 Interaction with RNA-Binding Proteins (FUS, TDP-43).....	39
2.6.4 UBQLN2 in Proteostasis Control .....	39
2.7 Therapeutic Target Space .....	40
2.7.1 Proteasome Enhancers and the Risk of Off-Target Proteotoxicity .....	40
2.7.2 Autophagy Inducers: mTOR-Dependent versus Independent Routes .....	41
2.7.3 Chaperone / Heat-Shock Pathway Activators .....	42
2.7.4 Targeted Degraders: PROTACs and AUTACs .....	44
3. Aims of this Study .....	46
4 Material and Methods .....	49
4.1 Generation of Stable Cell Lines and Cell Culture and inhibitor treatment .....	49
4.2 Protein Stability Assay and Analysis by Flow Cytometry .....	50
4.3 Immunofluorescence Staining.....	50
4.4 Confocal Microscopy.....	51
4.5 Image quantification and analysis .....	51
4.6 Fluorescence Recovery After Photobleaching (FRAP) and FRAP analysis ....	52
4.7 Biochemical Fractionation .....	52
4.8 Quantification of soluble fraction .....	53
4.9 Live-Cell Imaging .....	53
4.10 siRNA Knockdown.....	53
4.11 Cell lysates and Western blot .....	53
4.12 Sample preparation for BioID samples.....	54
4.13 MS data acquisition for BioID of TDP-43 WT and TDP-43 CTF .....	55
4.14 MS data acquisition for BioID of TDP-43 CTF treated with BZT and BafA1 ..	55
4.15 Data analysis for BioID of TDP-43 WT and TDP-43 CTF .....	55
4.16 Data analysis for BioID of TDP-43 CTF treated with BTZ and BafA1.....	56
4.17 Immunohistochemistry (IHC) Staining.....	57
4.18 Correlative Cryo-ET .....	58
4.19 Tomogram reconstruction, segmentation and template matching .....	59
4.20 Electrophoretic mobility shift assays .....	60
4.21 Protein expression and purification .....	60
4.21.1 UBQLN2 .....	60
4.21.2 TDP-43-MBP-His6 .....	60
4.21.3 MBP-FUS-His6/MBP-FUS-EGFP-His6.....	61

4.22 Microscopic condensate assay .....	61
5. Results – Part A.....	63
5.1 Cytosolically mislocalized TDP-43 and TDP-43 C-terminal fragments form cytosolic condensates upon proteasome inhibition .....	63
5.2 Proteasome inhibition induces amorphous non-fibrillar TDP-43 CTF condensates that acquire markers of TDP-43 pathology .....	66
5.3 TDP-43 CTF condensates are cleared by the autophagy-lysosome pathway requiring Hsp70 activity.....	69
5.4 Proximity proteomics reveals dynamic changes in the proteasome and autophagy network during TDP-43 CTF condensation and clearance.....	72
5.5 Autophagy receptor p62/SQSTM1 promotes TDP-43 CTF condensate formation, while WIPI2 is necessary for condensate clearance .....	77
5.6 p62/SQSTM1 and NBR1 show inclusion pathology in post mortem brains of FTD-TDP patients .....	80
5.7 p62/SQSTM1 and NBR1 show inclusion pathology in post mortem brains of FTD-TDP patients .....	81
5.8 Supplementary Figures .....	83
6. Results – Part B.....	88
6.1 Optimized Purification of UBQLN2 Variants with Minimal RNA Contamination	88
6.2 UBQLN2 Modulates RNA Binding and Phase Separation of FUS and TDP-43 .....	89
7. Discussion .....	92
7.1 Summary of findings described in Part A .....	92
7.2 Proteasome dysfunction selectively drives TDP-43 condensation distinct from stress granules or aggresomes.....	93
7.3 From liquid to amorphous: early pathological intermediates in cells and human tissue.....	95
7.4 Chaperone and autophagy cooperation in TDP-43 clearance (p62, WIPI2, KEAP1) .....	97
7.5 A proteostasis pathway switch: autophagy receptors and co-factor modules..	99
7.7 Broader implications and translational relevance.....	102
7.8 Summary of findings described in Part B .....	104
7.9 Mechanistic interpretation and disease context .....	105
7.10 UBQLN2 at the RNA/phase-separation interface.....	107
8. Scientific Acknowledgment .....	110
9. Contributions .....	111

10. Acknowledgment .....	112
11. References .....	113
12. Curriculum Vitae .....	150



# 1. Abbreviations

AAA+	ATPases Associated with diverse cellular Activities
ALS	Amyotrophic Lateral Sclerosis
ATG	Autophagy-related protein
BAG2	BCL2-associated athanogene 2
BTZ	Bortezomib
CHX	Cycloheximide
CMA	Chaperone-Mediated Autophagy
CTD	C-Terminal Domain
CTF	C-Terminal Fragment
CTF-25	~25 kDa C-terminal fragment of TDP-43
ER	Endoplasmic Reticulum
ESCRT	Endosomal Sorting Complex Required for Transport
FTD	Frontotemporal Dementia
FTLD	Frontotemporal Lobar Degeneration
FTLD-TDP	Frontotemporal Lobar Degeneration with TDP-43 pathology
FRAP	Fluorescence Recovery After Photobleaching
FUS	Fused in Sarcoma
G3BP1	Ras GTPase-activating protein-binding protein 1
GOF	Gain of Function
Hsc70	Heat Shock Cognate 70
Hsp	Heat Shock Protein
HSPB1 (Hsp27)	Heat Shock Protein Family B (small) Member 1
HSPB8	Heat Shock Protein Family B (small) Member 8
HSF1	Heat Shock Factor 1
IBMPFD	Inclusion Body Myopathy with Paget's disease and Frontotemporal Dementia
KD	Knockdown
KEAP1	Kelch-like ECH-associated Protein 1
LCD	Low-Complexity Domain
LC3	Microtubule-Associated Protein 1A/1B Light Chain 3
LIR	LC3-Interacting Region
LLPS	Liquid-Liquid Phase Separation
LOF	Loss of Function
MAPT	Microtubule Associated Protein Tau
mRNA	Messenger RNA
mRNP	Messenger Ribonucleoprotein
mTOR	Mechanistic Target of Rapamycin
NBR1	Neighbor of BRCA1 Gene 1
NLS	Nuclear Localization Signal
NLSm	Nuclear Localization Signal mutant
NTD	N-Terminal Domain

OPTN	Optineurin
PB1	Phox and Bem1 domain
PI3P	Phosphatidylinositol 3-phosphate
PNKP	Polynucleotide Kinase Phosphatase
PXX	Proline-rich repeat region of UBQLN2
PTM	Post-Translational Modification
PY-NLS	Proline-Tyrosine Nuclear Localization Signal
RBP	RNA-Binding Protein
RNP	Ribonucleoprotein
RRM	RNA Recognition Motif
SG	Stress Granule
SOD1	Superoxide Dismutase 1
SQSTM1 (p62)	Sequestosome 1
TAX1BP1	Tax1 Binding Protein 1
TBK1	TANK-Binding Kinase 1
TDP-43	TAR DNA-binding Protein 43
UB	Ubiquitin
UBA	Ubiquitin-Associated Domain
UBL	Ubiquitin-Like Domain
UBQLN2	Ubiquilin-2
UPS	Ubiquitin-Proteasome System
USP14	Ubiquitin-Specific Protease 14
VCP (p97)	Valosin-Containing Protein
WIP1 / WIPI2	WD Repeat Domain, Phosphoinositide-Interacting proteins 1 and 2



## **2. Introduction:**

### **2.1 From Neuron Vulnerability to Proteinopathy**

ALS is a progressive motor neuron disease marked by the degeneration of upper and lower motor neurons in the motor cortex, brainstem, and spinal cord<sup>1</sup>. Patients typically develop muscle weakness, spasticity, dysarthria, and dysphagia, with progressive paralysis leading to death from respiratory failure within 3–5 years of onset<sup>1</sup>. FTD, by contrast, is the second most common form of early-onset dementia after Alzheimer's disease, and is characterized by neuronal loss in the frontal and temporal lobes<sup>2</sup>. Clinically, patients present with behavioral variant FTD (including disinhibition, apathy, or compulsivity) or with primary progressive aphasia, involving language decline<sup>2,3</sup>. Disease progression is gradual with median survival ranging from 6–10 years depending on the subtype<sup>2</sup>.

Against this clinical backdrop, ALS and FTD are increasingly recognized as points along a disease spectrum: selective populations of neurons gradually lose proteostatic balance, allowing normally dynamic ribonucleoprotein assemblies to harden into toxic inclusions<sup>4,5</sup>. In this introductory chapter, I trace that journey from clinical and epidemiological observations to molecular pathology, setting the stage for deeper mechanistic questions in later sections.

#### **2.1.1 Epidemiology and Spectrum of ALS/FTD**

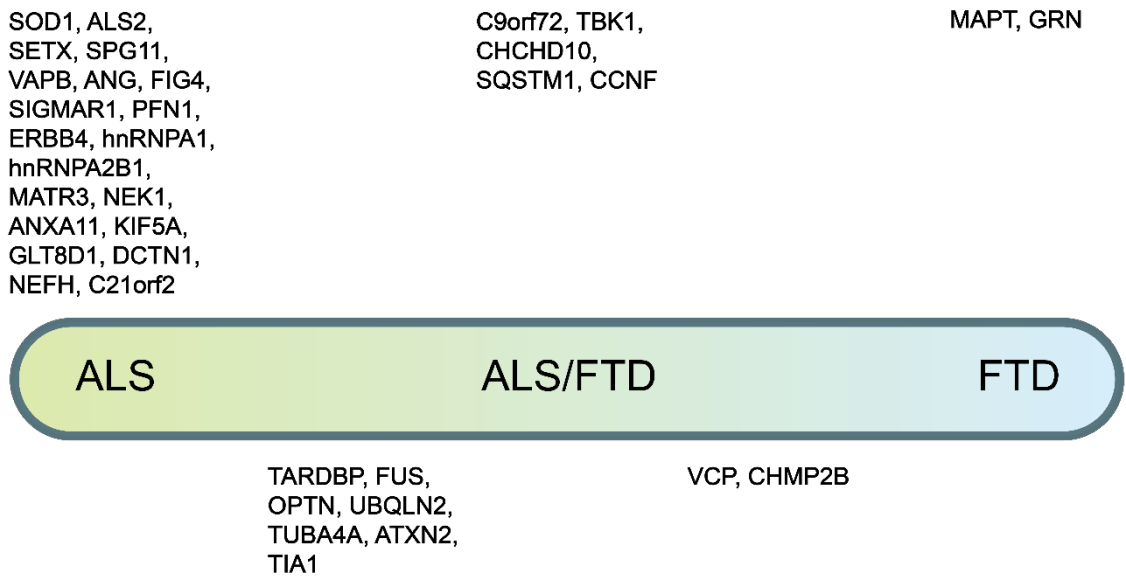
ALS is rare but measurable and, in some regions, rising. Long-running European registries estimate approx. 2.5–3.5 cases per 100,000 person-years, a recent Danish registry reports approx. 3.4/100,000 and a near-threefold increase since 1980<sup>6,7</sup>. This translates to point prevalence of approx. 5–10 per 100,000 in Western countries. Globally, prevalence varies widely, under 2 per 100,000 in some regions and up to approx. 11 per 100,000 in North America<sup>8</sup>. FTD is less common overall yet a leading cause of early-onset dementia (<65 years), with incidence approx. 2–4 per 100,000 person-years in midlife and prevalence approx. 15–22 per 100,000 at ages 45–64<sup>9</sup>. Both are relatively infrequent, but societal burden is amplified by younger onset, rapid disability, high caregiver cost, and the absence of disease-modifying therapy.

Although most cases present as sporadic, heritability is substantial. Meta-analyses indicate familial ALS accounts for approx. 8–9% of cases worldwide (slightly higher in Europe)<sup>10</sup>, leaving approx. 90% as sporadic, even though common variants and

polygenic risk likely contribute. FTD shows a stronger familial signal: approx. 30–40% report a family history, and approx. 10–15% carry autosomal-dominant pathogenic variants<sup>9</sup>. Mutations in a number of different genes are linked to either ALS, FTD, or both, underscoring their shared genetic basis (Fig. 1A). For example C9orf72, TARDBP (TDP-43), FUS, and UBQLN2 were first identified through familial ALS, while GRN and MAPT were discovered in familial FTD, yet all of these genes can give rise to either syndrome in different families or even in different members of the same family<sup>11,12</sup>. These genetic lesions converge on a limited set of cellular pathways (including RNA metabolism, protein quality control, nucleocytoplasmic transport, and autophagy) providing a mechanistic explanation for why ALS and FTD form a continuum rather than entirely separate diseases<sup>11,12</sup>.

Clinical boundaries blur as well. Roughly 15% of people with ALS meet diagnostic criteria for FTD (most often the behavioral variant), and a similar proportion of FTD patients later develop signs of motor-neuron disease, beyond categorical overlap, up to 50% of ALS patients have milder executive or cognitive deficits, while many FTD patients without overt ALS show subclinical motor-neuron involvement<sup>13,14</sup>. The GGGGCC repeat expansion in C9orf72 exemplifies this continuum: it is the most common known genetic cause of both disorders, ~40% of familial ALS and ~25% of familial FTD in some cohorts and can present with ALS, FTD, or mixed phenotypes<sup>15</sup>. Other genes show comparable pleiotropy: TDP-43 and FUS mutations may manifest as ALS with or without cognitive change, and X-linked UBQLN2 mutations often include dementia<sup>16,17</sup>. Recognizing an ALS–FTD spectrum has shifted research and trial design toward convergent mechanisms and shared endpoints across the continuum.

A



B

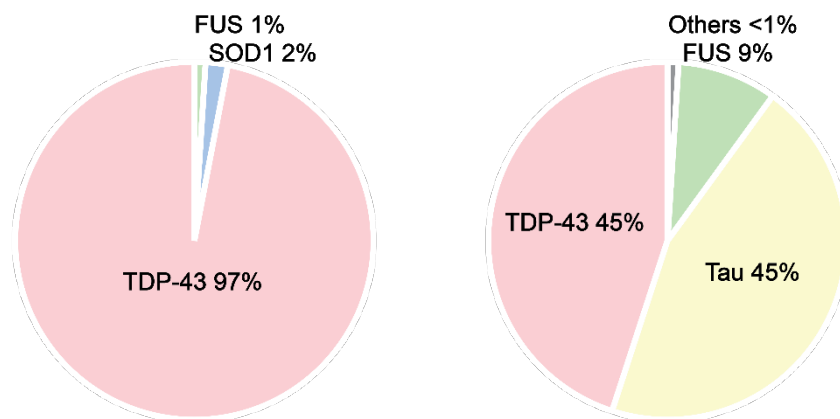


Figure 1 **Overlap of ALS and FTD**

**A** ALS and FTD mark opposite ends of a shared neurodegenerative spectrum

**B** Summary of key proteins found in pathological inclusions in the nervous system in ALS and FTD. Adapted from Ling et al. (2013)<sup>11</sup>

### 2.1.2 Shared Molecular Hallmarks of ALS/FTD

In addition to the clinical overlap, ALS and FTD converge by displaying ubiquitin- and p62-positive neuronal inclusions whose cores contain aggregated RNA-binding proteins (RBPs)<sup>18</sup> (Fig. 1B). A breakthrough study in 2006 identified TDP-43 as the major protein in ubiquitin-positive, tau-negative inclusions of ALS and FTD. The pathologic species is abnormally phosphorylated, ubiquitinated and cleaved, thereby establishing TDP-43 as a novel pathological protein in these diseases and linking them through a shared molecular phenotype<sup>19</sup>. In 2009, missense mutations in another

RNA-binding protein, Fused in Sarcoma (FUS) were identified in familial ALS patients, and FUS was subsequently shown to form inclusions in subsets of ALS<sup>16,20</sup>. TDP-43 aggregation is widespread (~97% of ALS and ~45% of FTD) making it a unifying hallmark. FUS inclusions are less common but mechanistically analogous<sup>20,21</sup>.

In addition to these RBP inclusions, a striking commonality is their consistent decoration with ubiquitin and the autophagy receptor p62/SQSTM1, indicating persistent engagement of protein quality-control pathways<sup>19</sup>. Beyond pathology, ALS and FTD also converge genetically: several causative genes can produce either ALS, FTD, or mixed phenotypes within families. The most prominent example is the hexanucleotide repeat expansion in *C9orf72*, but mutations in *TARDBP* and *FUS*, as well as in proteostasis-related factors such as *UBQLN2* and *SQSTM1*, are also linked to both disorders<sup>11,12</sup>. Together, these findings highlight that ALS and FTD share molecular hallmarks at both pathological and genetic levels, with convergence on impaired RNA metabolism and disrupted proteostasis as central disease mechanisms.

Another commonality between ALS and FTD is that neuronal RBP inclusions almost universally stain positive for ubiquitin and the autophagy receptor p62/SQSTM1, indicating that protein quality-control pathways are consistently recruited to these aggregates<sup>19,22</sup>. This pathological signature is echoed by genetics: several ALS/FTD genes encode key proteostasis factors. *UBQLN2* functions as a shuttle linking ubiquitylated clients to the proteasome and autophagy, and when mutated, it forms inclusions and impairs both pathways<sup>23</sup>. *SQSTM1/p62* acts as an autophagy receptor that scaffolds ubiquitylated cargo, *OPTN* is activated by TBK1-dependent phosphorylation to bind LC3, *VCP/p97* is an AAA+ segregase that extracts ubiquitylated substrates from membranes and condensates and *TBK1* itself is a kinase required for receptor activation. Mutations in these genes were first described in familial ALS/FTD, including *OPTN* in 2010, *TBK1* truncations in 2015, and *VCP*, initially linked to inclusion-body myopathy with Paget's disease, but later shown to cause familial ALS in ~1–2% of cases<sup>11,22,24,25</sup>. Taken together, these findings indicate that proteostasis is chronically overloaded or compromised in ALS/FTD, setting the stage for the mixed ubiquitin- and p62-positive skeins that typify pathology and providing a natural entry point into the broader theme of proteostasis failure. Together, pathology and genetics support a common endpoint: Proteostasis may be compromised or challenged in ALS/FTD, either as a cause or consequence of TDP-43 and FUS proteinopathy. This

puts proteostasis dysfunction in the spotlight as a common disease mechanisms in ALS/FTD.

## **2.2 Proteostasis Machinery**

The neurons most affected in ALS and FTD are among the longest-lived human cells (spinal  $\alpha$ -motor neurons and select frontotemporal cortical neurons) and must function for a lifetime<sup>26</sup>. Their longevity, large size, and anatomy place them at a proteostasis “edge case”<sup>27</sup>: unlike dividing cells, they cannot dilute damaged proteins, so misfolded species must be continually removed. A single motor axon can span over a meter, imposing logistical challenges because degradative organelles such as proteasomes and lysosomes are concentrated near the soma. Distal axons therefore depend on active transport and local protein turnover, with degradative vesicles formed at the periphery and ferried back to the cell body<sup>28</sup>. Proteasome activity in neurites can be rate-limiting for synaptic protein turnover<sup>29</sup>.

Metabolically, these neurons are highly active: they demand large amounts of ATP for oxidative metabolism, ion pumping, and continuous neurotransmission<sup>30</sup>. With aging, the efficiency of chaperones, proteasomes, and lysosomes declines<sup>31–33</sup>. Proteasomal peptidase activities decrease under oxidative stress<sup>34</sup>, and lysosomal degradation becomes less effective as membrane composition and pH control are altered. In practice, even modest hits to degradation capacity, shortfalls in energy supply, or inflammatory insults can accumulate into lasting cellular damage over decades.

Consequently, neuronal proteostasis operates with a narrow safety margin compared with other cell types<sup>35</sup>. For years these cells can compensate for the burden of misfolded, aggregation-prone proteins, but eventually a tipping point is reached. This framework helps explain why motor and cortical projection neurons are selectively vulnerable in ALS/FTD: the combination of extreme cell longevity, high metabolic load, and gradual age-related decline in quality-control systems creates a background in which genetic or environmental stressors more easily push the system into disease.

Maintaining proteostasis, folding, and degradation is particularly crucial in neurons. This section provides an overview of the cellular machinery that regulates protein turnover, focusing on aspects especially relevant to neuronal function and ALS/FTD pathogenesis. This reviews the ubiquitin conjugation system, the 26S proteasome, the autophagy-lysosome pathways, and points of crosstalk between these systems.

### 2.2.1 The Ubiquitin Conjugation Cascade: Writers, Readers, and Erasers

Ubiquitin (Ub) is a 76-amino-acid protein that is covalently attached to lysine residues on substrate proteins to dictate their fate<sup>36</sup>. Attachment proceeds through a three-step enzymatic cascade. First, a Ub-activating enzyme (E1) adenylates the C-terminus of ubiquitin in an ATP-dependent reaction and forms a thioester bond with its active-site cysteine. The activated Ub is then transferred to a Ub-conjugating enzyme (E2), which carries Ub via a similar thioester linkage. Finally, a Ub ligase (E3) recognizes specific target proteins and catalyzes transfer of Ub from the E2 to a lysine side chain (or occasionally the N-terminus) of the substrate. Mechanistically, HECT and RBR-type E3 ligases form a transient thioester intermediate with Ub before passing it on, whereas RING-type E3s act as scaffolds that juxtapose the E2-Ub conjugate and the substrate to promote direct transfer<sup>36–38</sup>. The human ubiquitin system comprises only two E1 enzymes, but roughly ~35 E2 conjugating enzymes and over 600 distinct E3 ligases, providing the breadth and specificity needed to ubiquitylate thousands of different substrates<sup>37</sup>. This cascade generates a spectrum of Ub modifications ranging from mono-ubiquitylation to diverse chain topologies (e.g., K48, K63, M1, or mixed linkages), each functioning as a molecular signal that can trigger proteasomal degradation, endocytosis, DNA-damage repair, or selective autophagy<sup>39</sup>. Proteins can be monoubiquitylated or decorated with poly-Ub chains. Ub itself bears seven lysines (K6, K11, K27, K29, K33, K48, K63) plus an N-terminal Met (M1), allowing linear or lysine-linked chains that constitute a “ubiquitin code.” Monoubiquitination frequently modulates interactions or localization, such as triggering receptor endocytosis<sup>39</sup>. K48- or K11-linked chains are canonical tags for proteasomal degradation by the 26S proteasome<sup>40,41</sup>. By contrast, K63 and linear M1 chains channel substrates into signaling networks, DNA-damage responses, and selective autophagy pathways<sup>41,42</sup>. On protein aggregates, K63 chains recruit autophagy “licensing” factors and cargo receptors to ensure sequestration into autophagosomes<sup>41</sup>. Less common linkages (K6, K27, K29, K33) control DNA repair, mitophagy, and other processes<sup>43,44</sup>. Mixed and branched chains (where a single Ub carries multiple linkages) further expand information density and tuning<sup>45,46</sup>.

This code is read by ubiquitin-binding domains (UBDs) in receptor and adaptor proteins. Ubiquitin-Associated domain (UBA), Ubiquitin-Interacting Motif (UIM), Npl4 Zinc Finger (NZF) and related modules recognize specific linkages or chain architectures<sup>47,48</sup>. Many readers are also routers: p62/SQSTM1 and NBR1 combine UBDs with LC3-

interacting regions (LIRs) to couple ubiquitylated cargo to the autophagy machinery, thereby bridging the ubiquitin signal to membrane sequestration<sup>49,50</sup>. In proteasomal routes, Rad23/HR23-like shuttles use UBA domains to bind chains and UBL domains to dock at the proteasome, handing off cargo for degradation, an arrangement mirrored by ubiquilins in neurons.

Balancing the writers are ~100 deubiquitylating enzymes (DUBs) that recycle Ub and edit Ub chains, preserving homeostasis and rescuing mis-tagged proteins<sup>51,52</sup>. At the proteasome, the DUBs USP14 and RPN11 shape flux: chain trimming or removal can either accelerate a protein's irreversible engagement with the proteasome for degradation or spare proteins from destruction. Pharmacologic inhibition of USP14 (e.g. by IU1) increases degradation of aberrant proteins and boosts resistance to proteotoxic stress in cells and mammalian models<sup>53,54</sup>. These interventions underscore how dosage-sensitive the code is. Too little ubiquitylation and substrates escape quality control. Too much, or the wrong linkage on the wrong target and essential proteins risk premature turnover.

In summary, E1–E3 “writers” install linkage-specific Ub patterns, UBD “readers” decode and route cargo to proteasome, lysosome, or signaling complexes and DUB “erasers” ensure reversibility. This information-rich code underlies how proteasome and autophagy pathways recognize and clear substrates in neurons, as will be explained in the next sections.

### **2.2.2 The 26S Proteasome: Architecture and Substrate Processing**

The 26S proteasome is a 2.5 MDa processive protease that selectively degrades proteins bearing ubiquitin chains. Functionally it behaves like a self-compartmentalized shredder: a barrel-shaped 20S core capped on one or both ends by a 19S regulatory particle<sup>55</sup>. The 20S core is a stack of four heptameric rings ( $\alpha$ 7- $\beta$ 7- $\beta$ 7- $\alpha$ 7). The two inner  $\beta$  rings house three catalytic subunits ( $\beta$ 1,  $\beta$ 2,  $\beta$ 5) with caspase-like, trypsin-like, and chymotrypsin-like specificities. These active sites face the lumen<sup>56</sup>. An  $\alpha$ -ring gate normally occludes the pore so only unfolded polypeptides can enter. Gate opening is tightly controlled so nonspecific proteins are excluded<sup>57</sup>. Together, core and caps assemble into the 26S holoenzyme that executes selective, compartmentalized proteolysis<sup>55</sup>.

The 19S regulatory particle (RP) is the gatekeeper and unfolding engine. It comprises a base : six AAA+ ATPases (Rpt1–Rpt6), ubiquitin receptors Rpn10/Rpn13, and scaffold Rpn1 and a lid with non-ATPase subunits including the metalloprotease DUB Rpn11<sup>58</sup>. Rpn11 sits near the entry to cleave ubiquitin chains en bloc as substrates become committed to degradation, salvaging Ub and allowing passage into the proteolytic chamber<sup>58,59</sup>. A second DUB, USP14 (Ubp6 in yeast), associates peripherally to trim chains before engagement and, when overactive, can stall commitment and delay degradation<sup>60</sup>.

Substrate processing follows a coordinated sequence. A substrate bearing a suitable K48-linked polyubiquitin chain (typically  $\geq 4$  Ub units) is captured by Rpn10/Rpn13 or delivered via shuttles such as Rad23 or ubiquilins<sup>40,61,62</sup>. Commitment triggers deubiquitylation (often Rpn11's en bloc removal) followed by mechanical unfolding and translocation of the substrate protein<sup>59</sup>: The AAA+ ring grips an unstructured segment and, through ATP hydrolysis cycles, feeds the polypeptide through the opened  $\alpha$ -gate into the 20S core for stepwise proteolysis<sup>57,63</sup>. High-resolution cryo-EM has visualized multiple functional states of the human proteasome, revealing a rotary “staircase” of ATPase subunits around the translocating chain. Distinct nucleotide-binding and hydrolysis states couple to substrate pulling, pore opening, and the timing of Rpn11 activity<sup>63,64</sup>. Seven conformations have been described, capturing successive snapshots of engagement, deubiquitylation, and hand-off into the core for structural support for a processive “pumping” mechanism<sup>64</sup>.

Neurons add distance and compartmentalization challenges. Misfolded proteins arise in distal axons and synapses, whereas most proteasomes cluster near the nucleus<sup>29,65</sup>. Shuttle factors such as HR23/Rad23 and ubiquilin-2 (UBQLN2), which carry a UBL domain to dock to the proteasome and a UBA domain to bind ubiquitylated substrates in the periphery, keep them soluble during transport, and escort them to perinuclear proteasomes<sup>62,66</sup>. This minimizes off-pathway capture by autophagy and reduces aggregation risk en route. In ALS, mutant UBQLN2 accumulates at synapses and fails to deliver cargo efficiently, producing distal proteostasis defects and leaving axonal proteins vulnerable to aggregation<sup>17,66</sup>. Beyond cargo shuttling, proteasome transport and local regulation in neurites are active research areas. Accumulating evidence suggests axonal/synaptic proteasomes are tightly controlled, dynamically positioned, and may become functionally compromised under disease conditions<sup>29,65,67</sup>.

In sum, the 26S proteasome recognizes polyubiquitin tags, edits them at the gate, unfolds substrates via its AAA+ motor, and cleaves them into peptides within the 20S core<sup>55,63</sup>. It performs most soluble protein turnover in partnership with the autophagy-lysosome system<sup>55</sup>. When load exceeds capacity, or when subunits are mutated, gates fail to open properly, or when protein aggregates hijack receptors, misfolded proteins accumulate, a particular hazard for long-lived neurons<sup>35</sup>. Conversely, boosting proteasome activity (e.g. by inhibiting USP14 to speed commitment, or by activating 20S gating to increase flux) is being explored therapeutically in ALS/FTD<sup>54,57,68</sup>.

### **2.2.3 Macroautophagy, Microautophagy, and Chaperone-Mediated Autophagy**

Macroautophagy (often just “autophagy” in general usage) is the best-studied autophagy pathway (Fig. 2A). In macroautophagy, a double-membrane vesicle called an autophagosome forms de novo to sequester cargo, then fuses with lysosomes<sup>69</sup>. The process begins with activation of the ULK1 kinase complex (ULK1–ATG13–FIP200–ATG101) in response to nutrient stress or other signals (classically, inhibition of mTORC1 is a key trigger). ULK1 phosphorylates downstream targets and leads to nucleation of an isolation membrane (phagophore) through the class III PI3-kinase complex I which consists of Vps34 (PIK3C3), Beclin1, ATG14L, and Vps15 (p150). Two ubiquitin-like conjugation systems (ATG8 and ATG12 systems) then act to expand the membrane: ATG8 (LC3/GABARAP in mammals) is lipidated and inserted into the autophagosome membrane<sup>70</sup>. This LC3 decoration is crucial, because LC3-family proteins on the inner membrane serve as docking sites for selective cargo receptors (such as p62/SQSTM1 or NBR1)<sup>71</sup>. The growing autophagosome eventually encloses its contents and then fuses with a late endosome or lysosome, where acidic hydrolases degrade the inner membrane and cargo<sup>69</sup>. Neurons rely on basal macroautophagy for routine turnover of organelles and proteins, and impaired autophagosome transport or fusion has been implicated in ALS (for example, mutations in dynactin, or in autophagy genes like TBK1)<sup>72</sup>.

Microautophagy involves the direct invagination of the lysosomal membrane to engulf cytosolic material (Fig.2A). It is a more direct, constitutive process compared to macroautophagy. In microautophagy, late endosomes or lysosomes bud inward, capturing small volumes of cytosol or even organelle fragments<sup>73–75</sup>. This process requires the ESCRT (endosomal sorting complex required for transport) machinery, particularly ESCRT-III components, to mediate membrane scission, and the Vps4

ATPase for recycling the ESCRT polymers<sup>76,77</sup>. Microautophagy was long considered mainly non-selective (a way to sample cytosol under starvation), but recent work has revealed selective microautophagy pathways<sup>73,74</sup>. A striking example is the endosomal microautophagy of ubiquitinated proteins: a 2025 study showed that components of ESCRT-I and an accessory protein PTPN23 can capture ubiquitylated tau aggregates directly into endosomal invaginations for degradation<sup>78</sup>. In this pathway, ESCRT-I (via its subunit TSG101) binds K63-ubiquitinated tau, and PTPN23 bridges ESCRT-I to ESCRT-III (bypassing ESCRT-II) to drive intraluminal vesicle formation and tau clearance<sup>42,78</sup>. This finding extends microautophagy's relevance beyond nutrient starvation to proteinopathy: even large aggregate-prone proteins like tau can be handled via micropinocytic engulfment by late endosomes<sup>75,78</sup>. It also highlights how ubiquitin signals are read by the endo-lysosomal system (TSG101 has a ubiquitin-binding UEV domain) analogous to how macroautophagy receptors use ubiquitin signals<sup>42,71,79</sup>.

Chaperone-mediated autophagy (CMA) is the most selective of the three. It does not involve any vesicle budding or double membranes<sup>80</sup> (Fig. 2A). Instead, specific proteins bearing a KFERQ-like pentapeptide motif are recognized by a cytosolic chaperone, Hsc70 (heat shock cognate 70)<sup>81</sup>. Hsc70 (and co-chaperones) unfold the target protein if necessary and deliver it to the lysosomal membrane, where a receptor called LAMP2A binds the substrate<sup>82</sup>. LAMP2A then assembles into a multimeric translocation complex, effectively a protein-conducting channel through which the unfolded substrate is threaded into the lysosomal lumen and degraded<sup>83</sup>. Importantly, the rate of CMA depends on LAMP2A levels and stability on the lysosomal membrane<sup>84</sup>. CMA is upregulated under prolonged mild stress (e.g. extended starvation) to selectively degrade certain enzymes and regulators, thereby fine-tuning metabolism<sup>80</sup>. In aging and disease, CMA efficiency declines<sup>31</sup>. For example, aging rodent livers show decreased LAMP2A, leading to reduced CMA. Neurons too exhibit an age-related drop in LAMP2A<sup>84</sup>. In Parkinson's disease brains, as mentioned, LAMP2A is greatly reduced and CMA substrates (like  $\alpha$ -synuclein) accumulate abnormally<sup>32</sup>. There is also evidence tying CMA decline to ALS: some ALS-linked proteins (e.g. mutant SOD1) can be CMA substrates, and enhancing CMA has been proposed to help clear these misfolded variants<sup>72</sup>. Thus, CMA intersects with neurodegeneration at multiple points (its impairment can contribute to toxic protein buildup) and conversely, pharmacological upregulation of CMA (e.g. with compounds like arimoclomol or

through genetic overexpression of LAMP2A) has shown beneficial effects in models of neurodegenerative disease<sup>85,86</sup>.

#### **2.2.4 Selective Autophagy: Aggrephagy, Mitophagy, and More**

Autophagy is not purely bulk turnover. Many cargos are cleared by selective pathways steered by receptors that bind the target and LC3/GABARAP on nascent autophagosomes<sup>72</sup> (Fig. 2B). p62/SQSTM1 and NBR1 bridge ubiquitinated clients to forming autophagosomes, and this mechanism can target protein aggregates in a process termed “aggrephagy”. This mechanism appears to be disrupted in ALS/FTD<sup>72</sup>. p62 oligomerizes via its PB1 domain to cluster ubiquitinated proteins into condensates, while its C-terminal LIR tethers the cluster to LC3 inside the autophagosome. NBR1 cooperates through parallel UBA/LIR interactions and helps recruit cargo to the growing isolation membrane<sup>50</sup>. TAX1BP1 adds initiation power: beyond a UBD and LIR, it carries a FIP200-binding motif (ULK1 complex), so this receptor can both cluster cargo and nucleate autophagosome formation locally<sup>87</sup>. Structural snapshots show TAX1BP1’s LIR bound to GABARAP and a separable “FIR” motif engaging the FIP200 claw, an architecture that explains why p62/TAX1BP1 bodies become preferred sites for membrane growth<sup>88,89</sup>.

Notably, mutations in p62 that disrupt UBA or LIR motifs cause ALS/FTD in some families, underscoring that failed aggrephagy is pathogenic<sup>90</sup>.

Another form of selective autophagy is mitophagy, which clears damaged mitochondria. In the PINK1–Parkin pathway, depolarized mitochondria accumulate PINK1 on the outer membrane. PINK1 phosphorylates ubiquitin and Parkin, unleashing Parkin’s E3 activity to build K63-linked ubiquitin chains on numerous outer-membrane proteins<sup>91</sup>. These chains create docking sites for OPTN and NDP52, which after TBK1 phosphorylation bind ubiquitin, LC3, and FIP200 to seed autophagosome formation around the organelle<sup>92</sup>. In intact cells, double-membrane wraps can be seen within minutes of damage, often near ER contact sites that likely supply membrane. Neurons also deploy receptor-mediated routes using LIR-containing outer-membrane proteins BNIP3 or NIX under hypoxia or developmental cues, bypassing ubiquitin<sup>91</sup>. Genes in this axis (OPTN, TBK1, VCP) are ALS/FTD-linked, and impaired mitochondrial quality control is a recurring feature in models, pointing to defective mitophagy in motor-neuron loss<sup>22,72</sup>.

Other selective modes extend this logic. ER-phagy (reticulophagy) uses receptors such as CCPG1 to remove damaged ER. Ribophagy (via NUFIP1) trims ribosome load during stress and pexophagy clears peroxisomes. Many rely on p62-like adaptors plus dedicated receptors, and stress in one compartment can propagate to others<sup>93</sup>. For example, UBQLN2-related ER–Golgi defects increase misfolded cargo in the ER and load ER-phagy. Conversely, cytosolic TDP-43 inclusions can sequester autophagy factors and indirectly impair mitophagy or aggrephagy<sup>72</sup>. The unifying theme is modularity: cargo-specific receptors read ubiquitin or organelle-encoded signals and recruit a shared core autophagy machine to dispose of diverse cellular components. In neurons, where proteostasis margins are thin, tuning these selective routes may be crucial for therapy: Restoring aggrephagy and mitophagy could relieve the downstream stress that drives ALS/FTD progression<sup>72,93</sup>.

Across pathways, a simple code helps triage cargo: K63-linked ubiquitin and receptor oligomerization favor autophagic routing, whereas K48 linkages often mark clients for proteasomal turnover<sup>36,42</sup>. Receptor families engage distinct LC3/GABARAP isoforms and frequently phase-separate with cargo, creating high-affinity hubs that concentrate the core machinery. This design allows speed and specificity as damaged structures are tagged, clustered, wrapped, and delivered to lysosomes before their toxic by-products spread<sup>87,93</sup>.

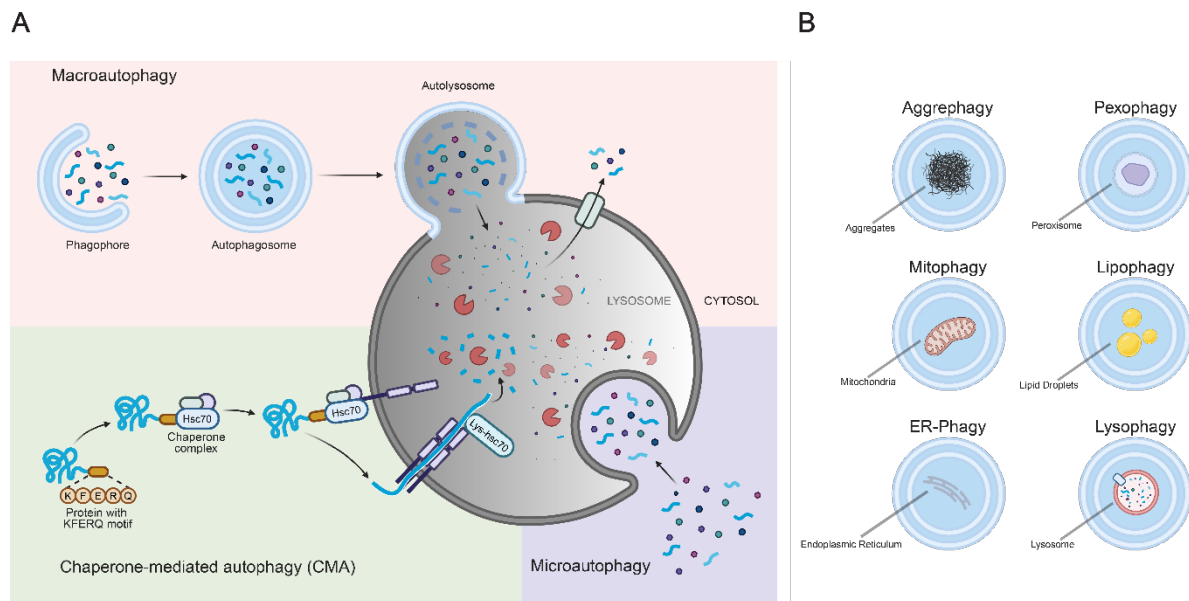


Figure 2 **Overview of autophagy pathways**

**A** Schematic representation of macroautophagy, chaperone-mediated autophagy (CMA), and microautophagy. For further description, see text in chapter 2.3 and 2.4

**B** Summary of the major forms of selective autophagy. Aggrephagy degrades aggregates, Mitophagy degrades mitochondria, Endoplasmic Reticulum (ER)-Phagy degrades ER, Pexophagy degrades peroxisomes, Lipophagy degrades lipid droplets and Lysophagy degrades lysosomes.

### 2.2.5 UPS–Autophagy Crosstalk and Stress-Response Switches

The UPS and the autophagy–lysosome system operate as a layered safety net with extensive crosstalk<sup>93</sup>. When proteasomes are inhibited or genetically weakened, ubiquitinated proteins accumulate. Cells sense this through several nodes. Keap1 becomes sequestered on ubiquitin-rich aggregates, freeing Nrf2 to enter the nucleus and induce a proteostasis program that elevates proteasome subunits together with p62 and other autophagy factors, broadening clearance capacity<sup>94</sup>. In parallel, proteasome stress eases mTORC1 restraint and allows TFEB to translocate to the nucleus, expanding lysosomal biogenesis and autophagy gene expression<sup>95</sup>. At the mesoscale, misfolded clients are hauled along microtubules by HDAC6 into perinuclear aggresomes that compartmentalize toxicity. These structures recruit p62 and TAX1BP1 to encapsulate cargo and deliver it into autophagosomes<sup>96</sup>. Consistent with this, chemical proteasome blockade rapidly raises p62 levels via Nrf2 and drives assembly of p62-positive autophagosomes destined to clear ubiquitinated clients<sup>94,95</sup>.

The feedback also runs in reverse. When lysosomes are impaired by for instance drugs that neutralize lysosomal pH or by storage disorders, autophagic cargo accumulates and ubiquitinated species leak back to the cytosol. Signaling via AMPK and mTOR then shifts toward proteasomal degradation to compensate<sup>93</sup>. p62, which builds up

when autophagy stalls, can bind directly to proteasomes through UBA–UBL contacts and re-route specific substrates away from the blocked pathway<sup>97</sup>. K48-linked chains generally point to proteasomal turnover, whereas K63 linkages favor aggregate handling and autophagy, giving receptors a code to triage cargo<sup>36,42</sup>. This “alternative routing” is still being mapped but fits the observation that many clients possess both proteasomal and autophagic options, with traffic reassigned according to load, localization, and physical state (monomeric versus aggregate-prone)<sup>93</sup>.

In neurons, these compensations are essential yet fragile. They defend an irreplaceable proteome spread across long axons by buffering local failures so they do not immediately trigger catastrophe. Spatial constraints matter: autophagosomes often form distally and undergo retrograde transport, while proteasomes concentrate in the soma (making hand-off and signaling especially important)<sup>35</sup>. With chronic stress and aging, both arms erode. ALS spinal neurons frequently display ubiquitin-rich inclusions alongside p62 accumulation and dysfunctional autolysosomes, pointing to a feed-forward loop in which aggregates spread, sequester key factors, and exhaust clearance capacity. Mutations in adaptors such as UBQLN2, p62, or OPTN further tip the balance: Blunting hand-off between systems and accelerating the slide from homeostasis to proteinopathy<sup>17,22,72,90</sup>.

In sum, the UPS and autophagy are interwoven by a common ubiquitin signal, shared adaptors, and coordinated transcriptional control (notably Nrf2 and TFEB). This redundancy normally confers robustness. Disrupt the nodes, and the network unravels into the protein deposits and degenerative cascades that typify ALS/FTD<sup>93</sup>. Therapeutically, the most promising approaches strengthen this interplay (via timed augmentation of proteasome activity, autophagic flux, or both) while avoiding global overactivation that can harm healthy proteins. Transient, CNS-targeted boosters or combinations that bias K63-tagged aggregates toward autophagy and spare K48-tagged regulatory proteins exemplify strategies to bolster proteostasis and delay collapse, especially in neurons under chronic load, and maintain neuronal health and function over time<sup>42,54,72</sup>.

### **2.2.6 Chaperones and Disaggregase Function**

Neuronal quality control is not only about tagging and ferrying unwanted proteins. It also requires physically extracting or dissolving aggregates. Two key disaggregase

systems do this work: the AAA+ ATPase VCP/p97 and the Hsp70–Hsp110 chaperone module<sup>98,99</sup>.

VCP/p97 acts as a hexameric ATP-driven unfoldase, a molecular winch. Each subunit carries an adaptor-binding N-terminus and two ATPase engines (D1, D2). VCP recognizes polyubiquitylated clients trapped in membranes, chromatin, or biomolecular condensates and uses ATP to pull and unfold them, handing substrates to the proteasome or other disposal routes<sup>98</sup>. Context-specific adaptors (e.g., UFD1–NPL4, p47) help VCP in the context of ER-associated degradation, chromatin extraction, or condensate remodeling, respectively, making VCP a key protein involved in various proteostasis pathways<sup>98,100</sup>. Missense mutations in VCP cause Inclusion Body Myopathy with Early-Onset Paget Disease and Frontotemporal Dementia (IBMPFD), a multisystem disorder that often includes ALS/FTD. Many variants, clustered in the N-terminal/D1 regions, dysregulate ATPase coordination, some hyperactivate unfolding, others uncouple subunits so extraction becomes mistimed or uncontrolled. Either extreme can disrupt proteostasis. Clinically, mutation severity tracks with phenotype: highly disruptive alleles bring earlier, broader involvement (muscle, bone, brain), while milder ones present later or mainly with myopathy. In ALS/FTD, VCP mutations are rare (<1%) but penetrant after mid-life, producing motor neuron disease plus inclusion-body myopathy, Paget’s disease of bone, and frontotemporal impairment, reflecting VCP’s ubiquitous role in tissue quality control<sup>24,98</sup>. Functionally, both loss- and gain-of-function behaviors converge on the same problem: dysregulated, poorly timed extraction that destabilizes cellular compartments and burdens downstream clearance pathways. In practical terms, VCP’s D1 ring integrates communication while D2 provides most of the motor force, so “jamming the cork” between subunits can desynchronize the entire hexamer<sup>98,100</sup>.

Once protein aggregates have formed, the Hsp70–Hsp110 system can dissolve them directly. J-domain (Hsp40) co-chaperones first target aggregate surfaces and recruit ATP-bound Hsp70. Upon hydrolysis, Hsp70 clamps exposed polypeptide loops and extracts them from the core<sup>101</sup>. Upon hydrolysis, Hsp70 clamps exposed polypeptide loops and extracts them from the core. Hsp110, as a nucleotide-exchange factor, rapidly reloads Hsp70 with ATP so the cycle repeats. Iterative pulling can extract monomers from otherwise “irreversible” fibrils, after which clients are either refolded by chaperone networks or handed to the proteasome or autophagy for degradation.

Multiple Hsp40s provide substrate specificity, steering the triage between refolding and degradation<sup>99</sup>. Disaggregation can transiently increase soluble oligomers, but these intermediates are typically captured by ubiquitin ligases and receptors such as p62 and cleared downstream<sup>101,102</sup>. In ALS models, this machinery handles TDP-43, SOD1, FUS aggregates and related species, but chronic proteotoxic stress and age-related declines in chaperone capacity can overwhelm it<sup>34,65,99</sup>. Evidence from experimental systems is encouraging: elevating Hsp110 delays symptom onset and reduces  $\alpha$ -synuclein/TDP-43 aggregation in vivo. Increasing Hsp70 or Hsp40 mitigates aggregation and improves neuronal survival in cell and animal models<sup>99,103,104</sup>. Even though there are no disease-causing mutations in any of these chaperones, disease conditions can blunt chaperone function. For example, Hsp70 can be sequestered into stress granules, co-factors can be depleted, and oxidative damage can slow the cycle, hindering disaggregation just when it is most needed<sup>65</sup>.

Therapeutically, these pathways offer tangible entry points. For VCP, the goal is not simply “more activity,” but correctly timed extraction. Small molecules that tune ATPase coordination or bias adaptor usage could restore control without off-target unwinding<sup>98</sup>. For the Hsp70 axis, several levers exist: co-inducers to raise chaperone expression, Nucleotide Exchange Factor (NEF)-targeted strategies to boost the Hsp110 reset step, or gene-delivery approaches aimed at vulnerable neuronal populations<sup>99,103</sup>. Conceptually, reinforcing disaggregase capacity should slow aggregate seeding and propagation while improving the hand-off to refolding or degradation routes<sup>101</sup>. In a compartmentalized cell like a motor neuron, where long axons separate sites of damage from the soma, keeping these extraction and dissolution engines running smoothly may be decisive for maintaining proteostasis under chronic stress<sup>65</sup>.

Having outlined the general clearance systems, the next section discusses ALS/FTD-linked genetic mutations in these pathways

## **2.3 Quality-Control Factors Linked to ALS/FTD**

### **2.3.1 Genetic mutations linked to ALS/FTD**

A notable share of familial ALS/FTD stems from mutations in genes that play important roles in proteostasis: the balance of protein folding, clearance, and degradation<sup>4</sup>. Together, mutations in these quality-control genes explain about 10% of inherited

ALS/FTD cases<sup>105,106</sup>. Most ALS/FTD-linked variants weaken clearance through the proteasome or autophagy, illustrating how modest sequence changes can have outsized neuronal impact<sup>4,72</sup>.

### **2.3.2 p62/SQSTM1, NBR1, OPTN, TAX1BP1, UBQLN2 and Other Important Factors**

The selective autophagy receptors p62 (SQSTM1) and its paralog NBR1 assemble via PB1-domain dimerization into helical filaments and carry tandem C-terminal modules, a ubiquitin-binding UBA beside an LC3-interacting region (LIR) that let them clasp ubiquitylated aggregates and feed them into nascent autophagosomes<sup>50,50,107</sup>. In ALS/FTD, SQSTM1 mutations commonly strike the UBA or LIR, thus weakening cargo recognition or autophagosome engagement, so that ubiquitinated proteins build up<sup>90</sup>. p62 also tunes stress defenses via the KEAP1–NRF2 axis. When KEAP1 binding is impaired, antioxidant induction falters, neurons face greater oxidative injury, and TDP-43-rich stress granules increase<sup>65,94</sup>. NBR1 cooperates with p62, forming mixed helical filaments that scaffold autophagic membranes and facilitate cargo clustering<sup>49,50,107</sup>. This cooperation allows NBR1 to partly compensate when p62 levels are limited. However, effective cargo recruitment depends on the ubiquitin-binding UBA domains and the LC3-interacting regions (LIRs) present in both p62 and NBR1. When these recognition motifs are mutated or disrupted, the filaments can still assemble but fail to connect ubiquitinated substrates to LC3-positive membranes, thereby abolishing selective autophagy<sup>49,50,107</sup>. In practice this means aggregate-linked ubiquitylation is sensed but not effectively converted into autophagic capture, so inclusions linger and redox stress escalates. Clinically, SQSTM1 carriers often show slower, later-onset ALS/FTD with gradual bulbar involvement, consistent with a partial erosion of this buffering pathway rather than a complete block<sup>65,90,94</sup>.

OPTN and TAX1BP1 act as alternative selective-autophagy receptors, operating in parallel to p62 and NBR1 to couple ubiquitylated cargo to LC3-positive membranes<sup>24,72</sup>. In resting cells, OPTN's LC3-interacting region (LIR) has intrinsically low affinity for LC3. Upon cellular stress, the kinase TBK1 phosphorylates OPTN at multiple sites including its LIR, which induces a conformational change that markedly increases LC3 binding and stabilizes cargo recruitment<sup>24,72</sup>. Disease variants in OPTN either blunt this TBK1-dependent activation or weaken ubiquitin affinity, stalling delivery<sup>22</sup>. TBK1 itself is an ALS/FTD-linked gene (~1% of cases): loss-of-function removes the “license”

needed by OPTN and TAX1BP1 to initiate selective autophagy, preventing proper phosphorylation and recruitment to damaged cargo<sup>24,72</sup>. A representative example is TBK1 E696K, which disrupts the OPTN–TBK1 interface and blocks efficient autophagosome formation<sup>108</sup>. TAX1BP1 specializes in aggrephagy: its N-terminal SKICH domain recruits the ULK1 initiation complex to nucleate autophagic membranes directly on aggregates (including p62 or UBQLN2 condensates), providing an alternate clearance route when p62 is saturated or when aggregates are densely packed<sup>109,110</sup>. In cell models, loss of TBK1 or OPTN leaves ubiquitylated clients marooned at phagophore rims. Restoring TBK1 activity re-opens flux and reduces aggregate burden<sup>72,110</sup>. Loss-of-function mutations in TBK1 abolish the phosphorylation signals needed to activate OPTN and TAX1BP1, thereby blocking this selective-autophagy route. Phenotypically, OPTN or TBK1 mutations often produce a slowly progressive, adult-onset ALS (ALS12 in OPTN families) with prolonged survival and occasional extra-motor features (mild parkinsonism, sensory changes, or cognitive involvement) illustrating how disruption of a single node (the TBK1–OPTN/TAX1BP1 axis) yields diverse outcomes across the ALS–FTD spectrum<sup>22,24</sup>.

Ubiquilins bridge ubiquitin tags to degradation. Ubiquilins (UBQLN1–4) are UBL–STI1–UBA shuttles that couple ubiquitylated clients to proteasome and autophagy<sup>72,111</sup>. UBQLN2’s proline-rich PXX repeat region (~30 motifs; the site of all ALS/FTD mutations) tunes condensate behavior and pathway routing<sup>112,113</sup>. Briefly, disease variants bias UBQLN2 toward forming persistent, less dynamic granules that fail to dissolve efficiently, leading to mis-triage of ubiquitylated clients away from normal proteasomal or autophagic clearance. Instead, substrates accumulate in stress-granule–like inclusions that sequester additional proteostasis factors<sup>23,112,114,115</sup>. Clinically, this manifests in an X-linked dominant inheritance pattern, with affected men typically developing earlier and more severe disease, while heterozygous women show variable penetrance depending on X-inactivation. In many families, the phenotype extends beyond motor neuron degeneration to include prominent cognitive or behavioral changes, reflecting UBQLN2’s broad role in neuronal proteostasis<sup>17,65,66</sup>. The specific molecular mechanisms by which UBQLN2 regulates proteostasis and contributes to ALS/FTD pathology are discussed in detail in chapter 2.6.

## 2.4 Phase Separation: From Physiology to Pathology

An emerging theme in neurodegeneration is the concept of biomolecular phase separation: The ability of proteins and nucleic acids to demix into non-membrane-bound compartments (also called biomolecular condensates) inside cells. Many ALS/FTD-linked proteins (TDP-43, FUS, hnRNPA1, etc.) can undergo phase separation, and this property seems to underlie both their normal functions and their propensity to aggregate in disease<sup>119</sup>. This chapter examines the biophysical principles of liquid-liquid phase separation (LLPS), its functions in cellular organization, and the mechanisms by which it may become dysregulated, resulting in pathological aggregation<sup>65,120</sup>.

### 2.4.1 Biophysics of LLPS and Prion-Like Low-Complexity Domains

Liquid-liquid phase separation (LLPS) is the demixing of proteins and RNAs into a dense liquid droplet that coexists with a dilute phase, producing membraneless organelles such as stress granules (SGs), P-bodies, and nucleoli<sup>121</sup>. LLPS is driven by multivalent, weak interactions: many phase-separating proteins carry intrinsically disordered, low-complexity domains that engage in transient  $\pi$ - $\pi$ , cation- $\pi$  and hydrogen-bond networks. In the “sticker-and-spacer” view, aromatic/charged residues act as stickers while flexible segments act as spacers, providing fluidity<sup>122</sup>. RNA adds valency by bridging multiple proteins and RNAs. Repeated motifs as found in many low complexity domains (LCDs, e.g. glycine-rich or Q/N-rich) and multiple RNA-binding sites commonly encode this multivalency. The balance of sticker number and spacer length helps set droplet viscosity and exchange rates<sup>121,122</sup>.

LLPS emerges once the concentration of a component crosses a threshold ( $C_{sat}$  = saturation concentration or critical concentration) and is tuned by cellular inputs<sup>122</sup>. For example, post-translational modifications can reshape interaction networks: Phosphorylation often suppresses phase separation by adding charge or disrupting  $\pi$  contacts, whereas polyubiquitin chains can raise valency and promote droplets<sup>123,124</sup>. Temperature, pH, ionic strength and ATP levels also shift propensity, for example ATP can act as a weak hydrotrope<sup>121,125</sup>. Cells exploit these levers by inducing condensates under heat shock or energy depletion, and by stalling translation so free mRNA accumulates to drive stress-granule assembly<sup>126</sup>.

Under normal conditions LLPS is rapid and reversible. When the trigger resolves, droplets dissolve and components re-mix with the cytosol or nucleoplasm, aided by

ATP-dependent chaperones and disaggregases that actively remodel interactions<sup>127</sup>. In neurons, LLPS concentrates postsynaptic proteins, organizes RNA transport granules along axons, and enables on-demand local biochemistry<sup>128,129</sup>. In ALS/FTD, however, mutations or chronic stress can tilt this balance so that droplets do not fully revert and begin a liquid-to-solid trajectory toward pathological aggregates<sup>65</sup>.

#### **2.4.2 Stress Granules and other Membraneless Organelles**

Stress granules (SGs) are among the best-studied biomolecular condensates. They form in the cytosol when translation initiation is blocked (e.g. under heat shock, oxidative stress or after treatment of cells with sodium arsenite)<sup>127</sup>. Untranslated mRNAs together with G3BP1/2 form a scaffold, and many different RBPs sitting on the stalled mRNAs rapidly relocalize to the scaffold<sup>65,130</sup>. SGs concentrate mRNAs, 40S ribosomal subunits, initiation factors, and many LCD-bearing RBPs in a membrane-free compartment that promotes survival by pausing translation and sequestering pro-apoptotic factors. In healthy cells they are transient and after stress, helicases (e.g., DDX3X) drive disassembly and translation resumes, restoring normal ribonucleoprotein traffic. SG remodeling is ATP-dependent and tightly timed. Failure to resolve leaves residual granules that begin to age and stiffen<sup>127</sup>.

In ALS/FTD, stress granules (SGs) are proposed to facilitate the formation of pathological RBP aggregates rather than act as strict precursors. ALS-linked mutations in FUS and hnRNPA1/hnRNPA2 enhance recruitment of these proteins into SGs and promote their liquid-to-solid transitions, leading to less dynamic, persistent assemblies<sup>125,131</sup>. For TDP-43, the situation is less clear: while SG association is observed under stress, aggregation appears to require additional triggers beyond simple mutation-driven recruitment<sup>132–134</sup>. Chronic stress or impaired clearance allows a subset of SGs to “mature” into ubiquitin- and p62-enriched solids that are earmarked for aggrephagy but often persist. Not all SGs mature into solid aggregates. Risk rises with sustained stress, disease mutations, or impaired proteostasis. p62 and other selective-autophagy receptors flag persistent SGs for lysosomal turnover, yet this pathway can saturate in neurons<sup>135</sup>. Small-molecule screens identify agents that destabilize SGs, compounds disrupting G3BP interactions or redox-active molecules such as lipoamide and low-dose arsenite<sup>136</sup>. That reduce pathological persistence and are being explored as therapeutic leads<sup>65,137</sup>.

LLPS also organizes other numerous other membraneless compartments, both in the nucleus and the cytoplasm. The nucleolus (functioning in ribosome biogenesis) is a tri-phasic droplet, Cajal bodies and nuclear speckles coordinate RNP assembly and splicing, and neurons use transport granules to ferry mRNAs to dendrites and dissolve them for local translation. Synaptic active-zone/postsynaptic densities show droplet-like organization that concentrates neurotransmission proteins<sup>128</sup>. These droplets exchange components on second-to-minute timescales, providing rapid, reversible control of biochemistry without building membranes and letting cells match organization to demand<sup>121,128</sup>.

### **2.4.3 Maturation Trajectories: Liquid → Gel → Amyloid**

Phase-separated condensates are dynamic, not static assemblies. Newly formed biomolecular condensates are often liquid-like, showing rapid molecular exchange, as demonstrated by fluorescence recovery after photobleaching (FRAP) which is a microscopy technique in which a defined region is photobleached and the return of fluorescence reports on molecular mobility. FRAP analyses typically show near-complete recovery within seconds<sup>138</sup>. *In vitro*, the dynamics of such liquid-like droplets typically slow down and viscosity rises, giving rise to a gel-like intermediate that remains partly reversible. With time or perturbation, some droplets harden into solid-like amyloid aggregates<sup>139</sup>. TDP-43's low-complexity domain can convert from droplets to  $\beta$ -sheet fibers within hours *in vitro*, especially under agitation<sup>140,141</sup>. FUS behaves similarly: its Q/G/S/Y-rich N-terminus forms hydrogels that age into cross- $\beta$  structures<sup>142</sup>. Repeated stress-recovery cycles and prolonged residence within granules can further "age" droplets by gradually strengthening interaction. Early stages remain labile, offering windows for intervention<sup>139</sup>.

Several forces drive this maturation of liquid droplets into more solid, fiber-containing assemblies<sup>138</sup>. Shear forces and crowding can push components into tighter contact, fostering aberrant cross- $\beta$ -interactions<sup>125,143</sup>. Motor-driven transport and the dense environment of stress granules likely contribute<sup>140</sup>. Chemical changes such as oxidation (creating intermolecular disulfides) or spontaneous cross-linking in aging cells can lock condensates into less fluid states<sup>144</sup>. Loss of RNA partners removes a key spacer: when RNA is degraded, proteins collapse together and solidify and several RBPs were shown to readily aggregate once stripped of RNA<sup>145</sup>. Recent studies indicate that amyloid fibrils preferentially nucleate at the condensate surface rather

than within the bulk, where local ordering can initiate  $\beta$ -sheet formation and seed further growth<sup>146</sup>

#### **2.4.4 Cellular Sensors of Aberrant Condensates**

Cells have layered surveillance mechanisms to sense, remodel, and remove maladapted condensates<sup>147</sup>.

First comes the heat-shock axis. Hsp70 and small heat-shock proteins patrol misfolded clients and overly rigid granules<sup>65</sup>. Under transient stress, inactive HSF1 forms short-lived nuclear foci. If these persist, signaling chaperone overload HSF1 triggers a program that boosts chaperone capacity and proteostasis genes<sup>148</sup>. In ALS models, HSPB1 (Hsp27) partitions into TDP-43 droplets to keep them fluid. Loss of HSPB1 lets droplets harden into aggregates that then amplify the broader heat-shock response. This creates a feedback loop between granule stiffness and chaperone supply<sup>149</sup>.

Next are ubiquitin-based sentinels. TRIM E3 ligases accumulate at stress granules and, when stiffness persists, decorate clients with mixed K48/K63 chains. This “ubiquitin coat” serves as a clearance tag (K48 favoring proteasomal processing, K63 favoring autophagic routing) and recruits VCP/p97 and UBQLN2 to extract clients and hand them to proteasomes or phagophores<sup>150</sup>. In neurons, mutations in VCP or UBQLN2 blunt this hand-off so granules linger and pathology accelerates. TRIMs themselves, with coiled-coil and prion-like segments, may further scaffold these decisions<sup>17,98</sup>.

Post-translational modifications (PTMs) act as molecular switches or “fluidity gauges” that modulate the material state of biomolecular condensates<sup>124,151</sup>. For instance, disease-associated hyperphosphorylation of TDP-43 at S409/410 – a hallmark of ALS/FTD pathology – suppresses TDP-43 phase separation and aggregation, rendering TDP-43 condensates more liquid-like and dynamic<sup>152</sup>. This counterintuitive finding suggests phosphorylation can serve as a protective brake against irreversible TDP-43 solidification<sup>152</sup>. Likewise, arginine methylation of FUS RGG motifs dampens phase separation and reduces aberrant recruitment into stress granules, whereas loss of methylation promotes excessive cytoplasmic aggregation<sup>153</sup>. Cells dynamically regulate these PTMs via dedicated kinases, phosphatases and methyltransferases, allowing real-time tuning of condensate assembly versus disassembly. Moreover, ubiquitin and SUMO modifications add additional layers of control to condensate dynamics. SUMOylation can initially promote condensate assembly through SUMO–

SIM interactions, but polySUMOylation of condensate proteins recruits SUMO-targeted ubiquitin ligases (e.g. RNF4) that ubiquitylate those proteins and target them for proteolytic clearance – effectively triggering condensate dissolution<sup>154</sup>. Similarly, direct ubiquitination of condensate components (e.g. K48- or K63-linked polyubiquitin chains) serves as a signal for proteasome or autophagy-mediated removal, limiting droplet persistence<sup>155</sup>. Notably, ubiquitin frequently accumulates on aberrant RNP granules in neurodegenerative disease, underscoring the role of the ubiquitin-proteasome system in identifying and disposing of hardened condensates<sup>155</sup>. Through such reversible PTMs, cells finely tune which condensates remain fluid and reversible and which are earmarked for solidification and degradation.

ATP-driven remodelers provide another layer. RNA helicases such as DDX3X, DDX5, and DHX36 use ATP to loosen RNA packing and prevent over-tight clustering<sup>156,157</sup>. Energy deficits (common with mitochondrial dysfunction) stall helicases and favor gelation<sup>157</sup>. VCP/p97's segregase activity likewise assists stress-granule disassembly while ALS-linked VCP variants impair this function, slowing recovery from stress<sup>135,158</sup>.

Finally, RNA itself buffers condensates. High RNA:RBP ratios keep assemblies liquid by spacing proteins and saturating low-affinity sites. When RNA becomes scarce (for example, after cleavage or global splicing disruption from nuclear TDP-43 loss), RBPs self-associate into  $\beta$ -sheet-rich aggregates. Abundant rRNA and mRNA thus act as a chaperoning reservoir for RBP homeostasis<sup>133,159</sup>.

Pathology arises when several tiers fail together: chronic stress sustains stress granules, chaperones are insufficient or sequestered, ubiquitin-mediated clearance is suboptimal, stress-response transcription (NRF2/HSF1/TFEB) lags and ATP falls short. Liquid RBP droplets, then tip over a narrow threshold into irreversible solids that recruit additional clients and propagate damage<sup>65</sup>.

This framework motivates therapies that reinforce surveillance (e.g. boost chaperones, stabilize RNA buffering, energize helicases) or accelerate disposal (e.g. enhance VCP/UBQLN2 hand-off, promote autophagy).

## 2.5 RNA-Binding Proteins in ALS/FTD

### 2.5.1 TDP-43: nuclear functions vs Cytosolic functions.

Transactive response DNA-binding protein of 43 kDa (TDP-43) is a ubiquitously expressed RNA-binding protein that predominantly resides in the nucleus but shuttles continuously between nucleus and cytoplasm<sup>4</sup> (Fig. 3). In healthy cells, TDP-43 plays crucial nuclear roles in gene expression regulation<sup>160</sup>. It binds to UG-rich sequences on pre-mRNAs and is best known for its role in regulating pre-mRNA splicing, particularly repressing the inclusion of cryptic exons<sup>161,162</sup>. This splicing repression safeguards transcript integrity. Loss of nuclear TDP-43 leads to aberrant cryptic exons being spliced into mRNAs, often disrupting open reading frames or triggering nonsense-mediated decay<sup>162</sup>. Beyond splicing, TDP-43 regulates multiple other RNA-processing steps<sup>163</sup>: it binds and stabilizes long introns, regulates mRNA stability and transport, and even contributes to miRNA biogenesis. TDP-43 can also bind certain gene promoters, linking it to transcriptional repression in specific contexts<sup>164–166</sup>. These diverse activities illustrate that in the nucleus TDP-43 functions as an essential gene-expression regulator and genomic gatekeeper<sup>4</sup>. In addition, TDP-43 safeguards genomic stability. Recent work shows that TDP-43 prevents the accumulation of R-loops during transcription, thereby avoiding replication stress and DNA damage. Loss or cytoplasmic mislocalization of TDP-43 leads to R-loop buildup, replication fork stalling, and double-strand breaks, ultimately compromising genome integrity in both dividing and post-mitotic neurons.<sup>167</sup>

Although mostly nuclear, a fraction of TDP-43 is present in the cytoplasm under normal conditions, where it has additional roles<sup>4</sup>. TDP-43 associates with mRNP granules and is involved in mRNA transport into neurites and local translation at synapses, thereby influencing protein synthesis in distal cellular compartments<sup>165,168</sup>. It also contributes to maintaining mRNA stability in the cytoplasm and participates in the cellular stress response<sup>65,164</sup>. For example, under stress conditions TDP-43 transiently relocates to stress granules, suggesting a role in stress-granule assembly or dynamics<sup>65,169,170</sup>.. Thus, TDP-43's normal cytosolic functions include regulating RNA fate after export and responding to cellular stress, complementing its nuclear RNA-processing duties. The balanced nucleo-cytoplasmic shuttling of TDP-43 is critical for its function, and cells actively import TDP-43 into the nucleus via a classical bipartite nuclear localization signal (NLS) (residues 82–98) recognized by the nuclear import receptor importin-

$\alpha/\beta^{171}$ . In contrast, TDP-43 nuclear export occurs by passive diffusion through nuclear pores rather than via an active receptor pathway, as shown by experiments where enlargement of TDP-43 impaired its nuclear exit. Thus, nuclear localization is primarily determined by active import and passive export<sup>172,173</sup> In summary, TDP-43 is a shuttling RBP with essential nuclear functions (e.g. splicing regulation, mRNA stability, transcription regulation) and important cytoplasmic functions (mRNA transport, local translation control, stress response), all of which are crucial for neuronal homeostasis. Disruption proper TDP-43 localization can set the stage for pathology, as seen in ALS/FTD when this delicate nucleo-cytosolic balance is lost.

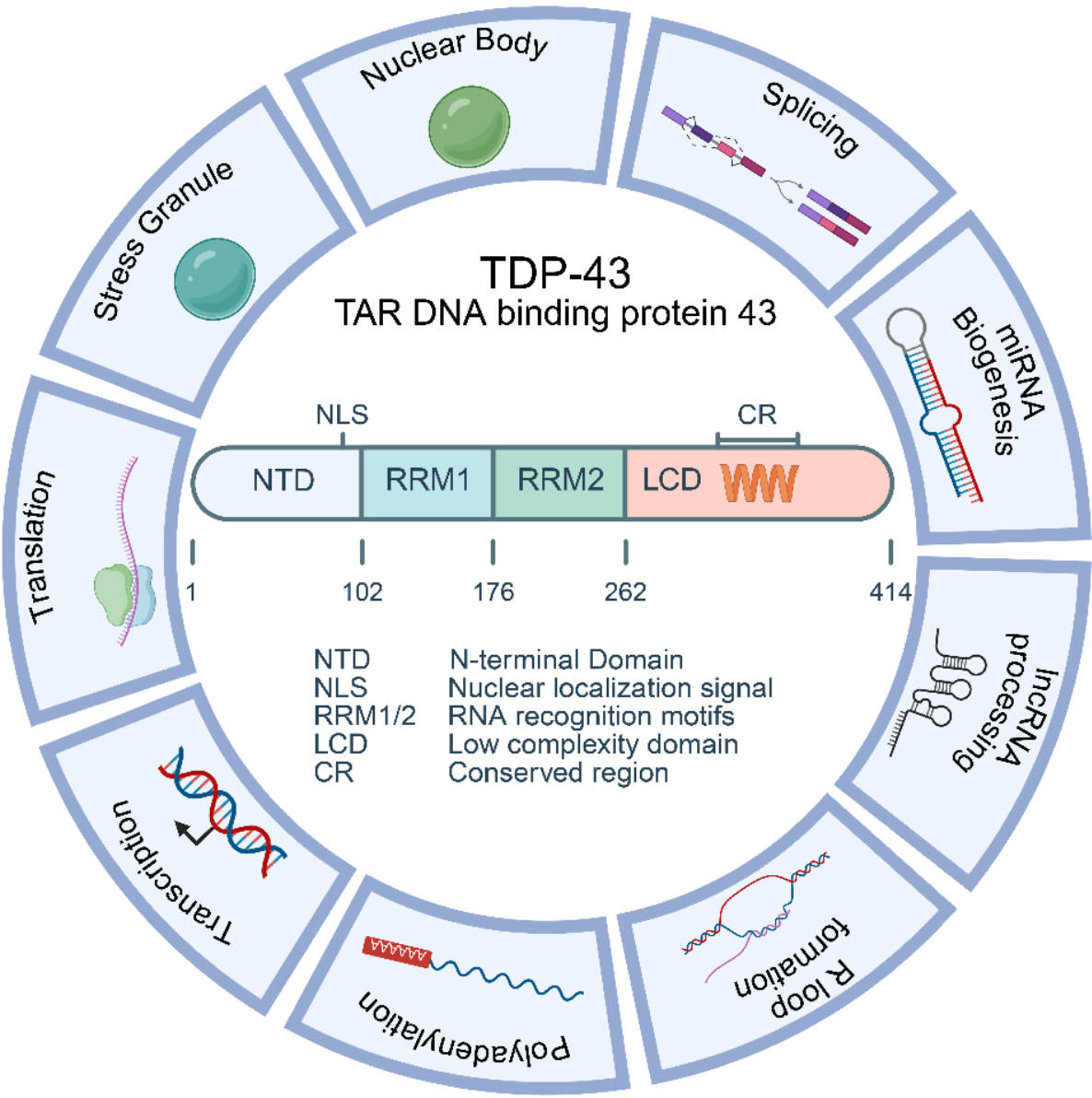


Figure 3: **TDP-43 as a regulator of RNA processing under physiological conditions.** Scheme in the middle displays the domain organization of TDP-43. Each box in the outer ring shows a functional role in which TDP-43 is involved

### 2.5.2 ALS/FTD linked TDP-43: Toxic Gain vs Loss of Function

A subset of ALS cases (and very rarely FTD) is caused by dominantly inherited TARDBP mutations. Dozens of pathogenic missense variants (over 50 by 2013) have been reported in familial and sporadic disease<sup>174–177</sup>. Most cluster in the C-terminal low-complexity domain that governs TDP-43's phase separation and aggregation behavior (see chapters 4.1 and 4.3) (a rare exception is D169G in RRM1)<sup>174,178</sup>. Clinically, TARDBP mutations account for ~1–5% of familial ALS, yet they are pivotal for understanding TDP-43 pathogenesis<sup>4</sup>. Common variants, A315T, M337V, Q331K, G348C, A382T generally preserve RNA binding but some have been shown to alter TDP-43's phase separation behavior or TDP-43 granule dynamics, thus biasing the protein towards more oligomerization and misfolding<sup>165,179,180</sup>. In neuronal models, these mutants more readily form perinuclear aggregates and trigger motor-neuron toxicity, whereas wild-type TDP-43 remains predominantly nuclear and less harmful<sup>181,182</sup>. Even subtle changes can tip the balance toward self-association<sup>183</sup>. Functional assays show that several variants accelerate oligomer formation, enhance stress-granule association, and increase detergent-insoluble species after heat or oxidative stress<sup>181</sup>. In vivo, spinal motor neurons expressing mutant TDP-43 display axon outgrowth defects, early synaptic loss, and progressive motor weakness<sup>184</sup>.

The relocalization of nuclear TDP-43 into cytoplasmic aggregates is thought to cause both toxic gain-of-function (GOF) and loss-of-function (LOF). In ALS and FTD, nuclear TDP-43 is frequently depleted, compromising its normal roles in RNA processing. Hallmark LOF readouts include the appearance of cryptic exons and the misprocessing of STMN2, which disrupt mRNA integrity and reduce the expression of key neuronal factors such as functional stathmin-2. These LOF signatures are consistently observed across iPSC-derived neuronal models and post-mortem patient tissue, underscoring their central role in disease mechanisms rather than being rare findings<sup>12,177</sup>. At the same time, cytoplasmic TDP-43 assemblies exert intrinsic toxicity: overexpression or seeded aggregation experiments show that inclusions perturb stress-response pathways and nucleocytoplasmic transport. Importantly, GOF aggregation and LOF are mechanistically linked, since the build-up of TDP-43 in cytoplasmic inclusions causes a depletion of nuclear TDP-43, thereby leading to splicing defects such as cryptic exon inclusion and STMN2 truncation. This coupling creates a feed-forward loop in which cytoplasmic aggregation drives nuclear loss, which further amplifies RNA dysregulation. Together, these findings highlight that both GOF and LOF contribute to

TDP-43 toxicity, and that their interplay is a defining feature of ALS and FTD pathogenesis<sup>12,177</sup>. Strikingly, depleting endogenous TDP-43 in model organisms phenocopies mutant overexpression, and deficits are rescued by reintroducing wild-type (but not mutant) TDP-43<sup>185</sup>. Human pathology mirrors this duality: cytoplasmic inclusions coexist with pronounced nuclear clearance across familial and sporadic cases<sup>186,187</sup>.

Together, these observations support a consensus that TDP-43 proteinopathy combines GOF and LOF, and that neuron survival requires a narrow window of TDP-43 activity: both overexpression and depletion are neurotoxic *in vivo*. Therapeutically, efforts follow two tracks<sup>188</sup>: (i) reduce aggregate-driven toxicity and spread, for example by enhancing autophagy/proteasomal flux or blocking seeding, and (ii) restore nuclear TDP-43 function by stabilizing protein levels, reinforcing nuclear import, or compensating key splicing programs. Seeding refers to the prion-like process in which preformed TDP-43 aggregates, either generated *in vitro* or derived from patient tissue, act as templates that recruit soluble TDP-43, promote its cytoplasmic aggregation, and propagate pathology to neighboring cells, thereby linking toxic gain-of-function with nuclear loss-of-function<sup>189,190</sup>.

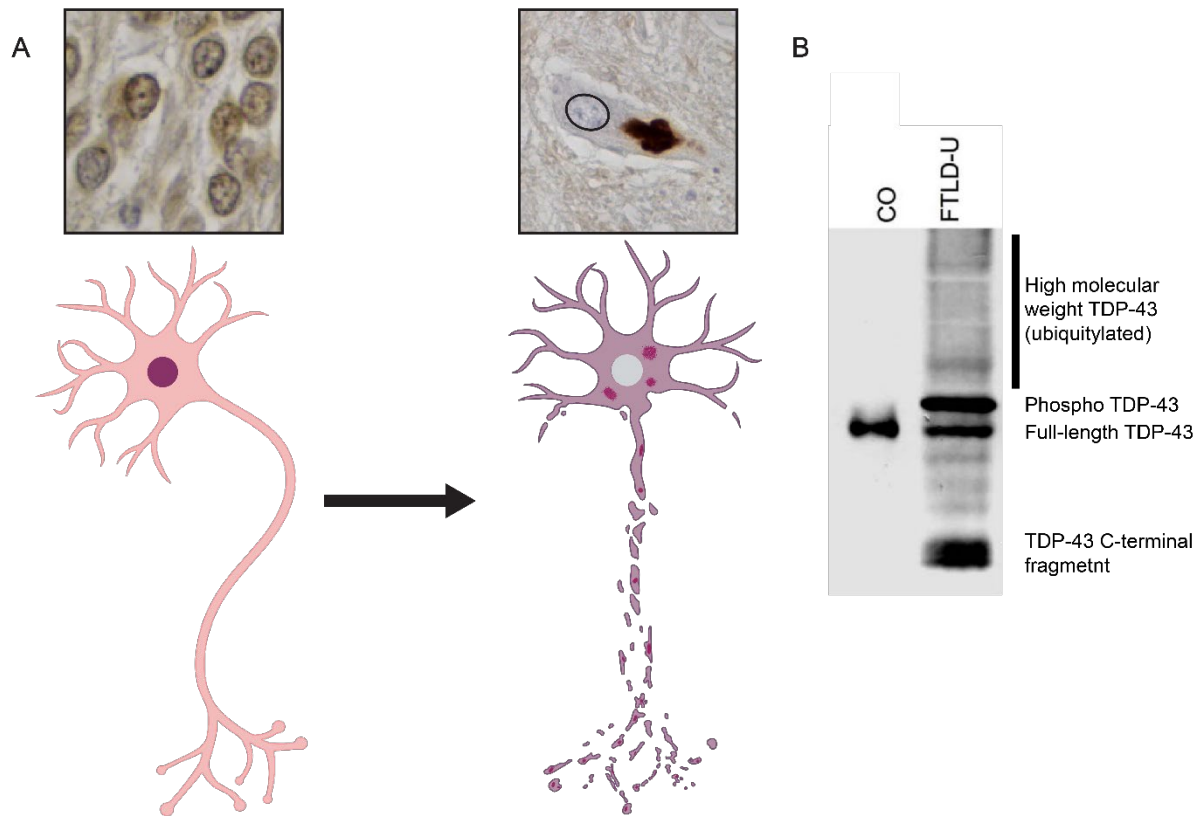


**Figure 4 TDP-43 pathology characterized by cytoplasmic inclusions and post-translational modifications**

**A** TDP-43 proteinopathies are defined by cytoplasmic aggregation and nuclear depletion of TDP-43.<sup>120,142</sup> See what is shown in the upper and lower images.

**B** Immunoblot analysis of frontal cortex tissue from healthy controls and FTLD-TDP patients, highlighting characteristic TDP-43 alterations. In controls, a single band corresponding to full-length TDP-43 is detected. In FTLD-TDP samples, additional features are observed: a higher shifted band corresponding to phosphorylated TDP-43, a high-molecular weight smear indicative of TDP-43 ubiquitination, and a lower-molecular weight band corresponding to TDP-43 C-terminal fragments<sup>191</sup>(with permission to reuse with CC-BY license).

### 2.5.3 TDP-43 Domain Organization, Post-translational Modifications, And Disease-Associated Properties.

TDP-43 (414 aa) is organized as a modular RNA-binding protein whose design enables physiological nucleic acid interaction and oligomerization, but also pathological self-assembly. At the N-terminus ( $\approx 1-77$ ), a structured N-terminal domain (NTD) adopts a ubiquitin-like fold that supports dimerization and higher-order oligomerization<sup>192</sup>. This multimerization is important for splicing repression because it helps recruit spliceosomal cofactors to selected pre-mRNAs<sup>193,194</sup>. Immediately downstream lies a classical bipartite nuclear localization signal (NLS, 82-98) with two basic clusters separated by a short spacer. Importin- $\alpha/\beta$  recognizes this NLS to drive efficient nuclear import and maintain the protein's predominantly nuclear steady state<sup>171</sup>.

The central region houses two RNA-recognition motifs: RRM1 ( $\approx$ 106–176) and RRM2 ( $\approx$ 191–257) that bind to UG- and TG-rich motifs in RNA (and DNA, respectively), enabling broad transcript engagement<sup>161,195</sup>. Together, the RRM s cooperate with flanking disordered segments to clamp RNA, influence exon choice, and help position TDP-43 within ribonucleoprotein (RNP) assemblies<sup>160,164</sup>. Beyond RRM2, the C-terminal region ( $\approx$ 274–414) is an intrinsically disordered low-complexity domain (LCD) enriched in glycine, serine, asparagine, glutamine and aromatic residues<sup>196</sup>. As mentioned above (chapter XXX), this C-terminal region provides the weak, multivalent interactions that drive liquid–liquid phase separation (LLPS), concentrating TDP-43 in biomolecular condensates, such as stress granules and other RNP granules, e.g. transport granules in axons and dendrites<sup>183,197</sup>

Biophysically, the LCD carries several amyloid-prone “cores” (286–331, 318–343, 342–366) that can adopt  $\beta$ -sheet structure and stack into filaments under aberrant conditions. Deleting or mutating these segments reduces aggregation propensity, emphasizing their role as nucleation elements<sup>198</sup>. More recently, high-resolution cryo-EM analyses of inclusions from ALS/FTD patient brains identified the amyloid core of TDP-43 to span approximately residues 277–414, showing that the LCD itself folds into ordered  $\beta$ -sheet assemblies that differ between disease subtypes, consistent with conformational polymorphism underlying clinical heterogeneity<sup>199–201</sup>. The LCD also was shown to form amyloid fibrils *in vitro* and can be used to create seeds that can elicit prion-like cell-to-cell propagation in model systems<sup>65,189,190</sup>. Reflecting this architecture, most ALS -linked missense variants are located in the C-terminal LCD region, consistent with the LCD’s central role in both reversible phase separation and irreversible fibrillization<sup>183,190</sup>. In short: TDP-43 contains an NTD for oligomerization, a NLS for nuclear localization, two RRM s for sequence-selective RNA/DNA-binding, and a prion-like tail that enables function yet seeds pathology when regulation fails.

TDP-43 also contains numerous disease-related post-translational modifications (PTMs)<sup>151</sup>. Hyperphosphorylation is the signature lesion. Cytoplasmic inclusions in ALS and FTLD-TDP are strongly labeled at Ser409/410 (sites rarely modified on normal nuclear TDP-43) making phospho-Ser409/410 a robust pathological marker used widely in tissue studies<sup>202</sup>. However, additional phospho-sites have been identified in ALS/FTD post-mortem brains, in particular on C-terminal serines<sup>203,204</sup>. Recent mechanistic work has challenged the long-standing view that phosphorylation

drives aggregation. *In vitro* and cell-based assays now show that casein kinase 1 $\delta$ -mediated hyperphosphorylation, or phosphomimetic substitutions mimicking disease-associated sites, suppress TDP-43 condensation and aggregation<sup>152</sup>. Instead, phosphorylation renders condensates more liquid-like, reduces recruitment into stress-induced membrane-less organelles, and enhances protein solubility in neurons<sup>152,205</sup>. Thus, rather than being a simple aggregation trigger, C-terminal hyperphosphorylation may represent a protective cellular response aimed at counteracting TDP-43 solidification<sup>206</sup>. Ubiquitination is equally pervasive. TDP-43 aggregates in ALS/FTD patients carry both K48- and K63-linked chains, signaling parallel clearance attempts<sup>207</sup>: K48 for proteasomal degradation and K63 for autophagic routing or inclusion organization. TDP-43 is a frequent target of ubiquitination in neurodegenerative disease, and several lysine residues have been identified as ubiquitin attachment sites, including K84 and K95 within the nuclear localization signal, K160, K181, and K263 in the RNA-binding regions, and Lys-408 near the pathological phosphorylation sites S409/410<sup>208</sup>. Modification at these sites can influence both nuclear import and aggregation propensity, underscoring the interplay between ubiquitination and phosphorylation. Multiple ubiquitin ligases mediate these modifications under stress or mislocalization conditions. For example, Parkin can attach both K48- and K63-linked chains to TDP-43, favoring its sequestration into cytoplasmic inclusions rather than degradation<sup>209</sup>, while RNF220 promotes polyubiquitination and proteasomal degradation of TDP-43, with haploinsufficiency causing cytoplasmic accumulation and ALS-like phenotypes in mice<sup>210</sup>. Patient tissue and model systems show that aggregated TDP-43 carries both K48- and K63-linked ubiquitin chains, consistent with parallel attempts at proteasomal and autophagic clearance<sup>208</sup>. In parallel, SUMOylation has emerged as another key modification. Recent studies demonstrated that SUMO2 attachment to Lys-408 is stress-inducible and protective: preventing this SUMOylation increased TDP-43 pathology and neuromuscular defects in knock-in mice<sup>211</sup>. Oxidative stress was shown to trigger PIAS4-dependent SUMO2/3 conjugation of cytoplasmic TDP-43, preventing irreversible aggregation and selectively modifying RNA-free protein<sup>212</sup>. In addition, SUMOylated TDP-43 in PML nuclear bodies was shown to attract SUMO-targeted ubiquitin ligases and engage p97/VCP, coupling SUMO to ubiquitin-mediated disaggregation and clearance<sup>213</sup>. Together, these findings highlight an intimate crosstalk where SUMOylation serves both to buffer TDP-43 against aggregation and

to prime it for ubiquitin-dependent processing. Disruption of either system tips the balance toward persistent TDP-43 inclusions, explaining why ubiquitin and SUMO signals are so consistently found on pathological TDP-43 in ALS and FTD.

A third PTM, lysine acetylation links loss of RNA binding to mislocalization. Acetylation within the NLS (K82/K84) weakens importin binding<sup>214,215</sup> and promotes cytoplasmic retention, while acetylation at RRM1 (e.g., K136, with nearby sites such as K145) directly diminishes RNA affinity because these lysines lie at or near the RNA-contact surface<sup>214–217</sup>. Acetyl-mimic substitutions (Lys→Gln) reproduce disease-like features in cells: K84Q drives cytosolic mislocalization, K136Q remains nuclear yet forms droplet-like foci and becomes aggregation-prone. By contrast, acetyl-blocking mutants (Lys→Arg) keep TDP-43 largely soluble<sup>216,217</sup>. Conceptually, acetylation “frees” TDP-43 from RNA/chaperone partners, increasing the pool available for aberrant phase transitions. The resulting inclusions are typically ubiquitin-positive and pS409/410-positive, mirroring patient tissue<sup>19,202</sup>.

#### **2.5.4 Proteolytic Cleavage and C-Terminal Fragments of TDP-43**

In addition to residue-specific post-translational modifications, proteolytic cleavage represents a distinct and highly pathogenic modification of TDP-43. Brains from ALS and FTD patients frequently contain C-terminal fragments (CTFs) of TDP-43, most prominently a ~35-kDa intermediate (CTF-35) and a protease-resistant ~25-kDa species (CTF-25)<sup>19,218,219</sup>. These fragments arise through sequential cleavage by caspases and calpains. At the endoplasmic reticulum, caspase-4 initiates cleavage at Asp174, located between the two RNA recognition motifs (RRM1 and RRM2), producing the ~35-kDa intermediate fragment. This is followed by caspase-3/7 and calcium-activated calpains, which cut within the low-complexity domain (LCD) to generate the ~25-kDa fragment<sup>220,221</sup>.

Biochemically, CTF-25 is stripped of the N-terminal nuclear localization signal (NLS) and the RNA-binding RRM. As a result, it is inefficiently imported into the nucleus and displays impaired RNA binding, while retaining the aggregation-prone LCD. These properties cause CTF-25 to mislocalize to the cytoplasm and aggregate at much lower concentrations than full-length TDP-43<sup>222</sup>. In cellular and animal models, chronic production of CTF-25 is sufficient to drive motor neuron degeneration and to nucleate co-aggregation of full-length TDP-43, a process consistent with pathological seeding<sup>189,190,219</sup>.

### 2.5.5 Chaperones in TDP-43 Pathology

In addition to the Hsp70/Hsp40/Hsp110 axis working on TDP-43 aggregates<sup>99,101,103</sup>, as mentioned above, work by David Cleveland and colleagues (2022) identified the small heat-shock protein HSPB1 (Hsp27) as a central regulator of TDP-43 aggregation. Acting as a “holdase,” HSPB1 binds cytoplasmic TDP-43 (engaging both its RNA-binding and low-complexity domains), partitions into TDP-43 condensates, and keeps them fluid and reversible<sup>149</sup>. In cell models, HSPB1 becomes enriched in stress granules and is required for their disassembly once stress resolves<sup>149,223</sup>. Depleting HSPB1 produces the opposite phenotype: droplets gelate and TDP-43 is trapped in the cytoplasm and depleted from the nucleus, and persistent inclusions form, recapitulating a hallmark of ALS. Consistently, motor neurons from ALS patients with TDP-43 aggregates show sharply reduced HSPB1 levels, suggesting that neurons unable to induce or maintain this chaperone are those in which TDP-43 pathology takes hold, as seen across multiple cell lines and stress paradigms<sup>149</sup>.

HSPB1 works within a broader chaperone module. Efficient clearance of TDP-43 condensates also requires the ATP-driven HSP70 system (HSPA1A) and the nucleotide-exchange factor BAG2<sup>149</sup>. The emerging division of labor is that HSPB1 stabilizes a remodelable, non-gelled state, while HSP70 together with BAG2 actively refold or extract TDP-43 so stress granules dissipate. If HSP70 is inhibited, TDP-43 droplets remain gelled even when HSPB1 is present, underscoring that the small HSP sets the stage but the HSP70 machinery performs the heavy lifting. Mechanistically, this module behaves like a two-step safeguard: HSPB1 prevents hardening, and HSP70/BAG2 resolve what remains, including under oxidative and osmotic stress challenges<sup>149</sup>.

Similar principles likely extend to other prion-like RNA-binding proteins. For example, the small heat-shock protein HSPB8 can chaperone FUS’s RNA-binding domain and restrain aberrant phase transitions, pointing to a generalized small-HSP defense against pathological condensation<sup>224,225</sup>. This broader context helps explain why some neurons succumb while others cope: cells with robust inducible small-HSP programs may keep droplets in a reversible state long enough for HSP70/BAG2 to complete clearance<sup>149,226</sup>.

These insights are mechanistic and actionable. They explain how neurons can actively counter TDP-43 aggregation, by maintaining liquid-like condensates and then

remodeling or removing their contents and they highlight why certain motor neurons might be especially vulnerable<sup>149</sup>: with age or chronic stress, HSPB1 reserves and inducible chaperone capacity can wane, pushing droplets past the point of return<sup>225</sup>. Therapeutically, two complementary strategies emerge. One is to increase HSPB1 expression or enhance its interaction with TDP-43 to prevent “going solid.” The other is to boost HSP70/BAG2 capacity to clear existing inclusions, especially during acute stress<sup>149</sup>. More broadly, the findings reinforce a central theme: when protein-quality-control systems falter (because of mutations or persistent stress) neurodegeneration follows, fortifying those pathways could slow or halt ALS/FTD progression<sup>4</sup>.

### **2.5.6 FUS: similarities and differences to TDP-43**

Fused-in-sarcoma (FUS) shares the same tripartite architecture, a structured RNA-binding core flanked by prion-like LCDs but arranges its elements differently<sup>227</sup>. An N-terminal QGSY-rich LCD (aa 1–214) drives LLPS and prion-like propagation<sup>153,228,229</sup>. In addition, the arginine-rich RGG regions distributed across the protein also strongly contribute to FUS phase separation.<sup>153,228</sup> Perturbation of these arginine residues by mutation, post-translational modification (such as arginine methylation), or pharmacological intervention strongly alters FUS condensate behavior, underscoring their importance for both LLPS and pathological aggregation. A central RRM (aa 285–370), multiple RGG boxes and a zinc-finger mediate promiscuous RNA/DNA binding and a C-terminal PY-NLS (aa 501–526) engages Transportin-1 rather than importin- $\alpha/\beta$ <sup>230–232</sup>. Both proteins shuttle constitutively between the nucleus and cytoplasm and they have similar functions in RNA processing<sup>233</sup>, but FUS is biased toward co-transcriptional splicing, DNA-damage sensing and mRNA transport into dendritic spines<sup>230,234,235</sup>. TDP-43 contributes to these processes as well, but its defining difference from FUS is its role in suppressing cryptic exon inclusion, a function essential for maintaining transcript integrity<sup>162,236</sup>. ALS-linked mutations in FUS cluster in the PY-NLS, weakening nuclear import and enhancing localization of FUS in cytoplasmic stress granules.<sup>20,230,237</sup> The nuclear-import receptor Transportin-1 can reverse aberrant FUS phase transitions *in vitro* and in cells<sup>153,202,238–240</sup>.

A further distinctive difference between the two proteins is that mislocalized FUS exerts a strong toxic gain-of-function, as demonstrated in multiple mouse models, making FUS lowering (e.g. with antisense oligonucleotides) a promising therapeutic strategy<sup>241,242</sup>. In contrast, TDP-43 toxicity is more strongly linked to nuclear loss-of-

function, since its role in splicing regulation cannot be compensated by other RBPs to the same extent as FUS, where the related proteins EWS and TAF15 can partially buffer nuclear loss<sup>243</sup>.

### **2.5.7 Comparative pathology of TDP-43 versus FUS inclusions**

TDP-43 inclusions dominate sporadic and familial ALS, appearing as cytoplasmic skeins in lower motor neurons, compact cortical inclusions, and oligodendroglial granules. They are ubiquitin- and p62-positive, heavily phosphorylated, and often coincide with nuclear-envelope fragmentation<sup>19,202,244</sup>. By contrast, FUS pathology is rarer (<1% ALS, ~10% sporadic FTL) and affected patients are frequently younger. FUS inclusions are also p62-positive, but only weakly ubiquitinated and there is no sign of hyperphosphorylation. FUS aggregates in FTD patients instead show a loss in arginine dimethylation and a co-deposition of the nuclear import receptor Transportin-1, whose affinity is regulated by FUS arginine methylation<sup>245–248</sup>.

## **2.6 UBQLN2 at the UPS–Autophagy Interface**

UBQLN2 is a multi-function quality control factor that interacts with both the proteasome and autophagy pathways<sup>66</sup>. Mutations in *UBQLN2* cause an X-linked dominantly inherited form of ALS/FTD (one of the rare instances of a single-gene cause in non-SOD1 ALS)<sup>4,17</sup>. Studying UBQLN2 gives insight into how neurons normally dispose of misfolded proteins and what happens when this process fails<sup>66</sup>.

### **2.6.1 Shuttle Function: Proteasome Escort vs. Autophagy Adaptor**

UBQLN2 functions as a ubiquitin/aggresome shuttle that links tagged clients to degradation<sup>114,117</sup>. Its N-terminal UBL domain docks on the 19S proteasome (via Rpn10/Rpn13), its C-terminal UBA domain binds polyubiquitin chains, and the intervening PXX and ST11 segments engage chaperones<sup>249–251</sup>. This architecture lets UBQLN2 grab a misfolded, ubiquitinated protein via UBA and deliver it to the proteasome by tethering UBL to the 19S cap. After hand-off the client is degraded and UBQLN2 is recycled for another round<sup>66,114</sup>. Under acute proteotoxic stress, UBQLN2 rapidly relocates to ubiquitylated inclusions, where it concentrates misfolded material and coordinates with proteasomes and autophagy machinery to clear debris. This dynamic redistribution is a hallmark of its first-response role. Together these interactions sustain clearance throughput during routine protein turnover<sup>66,114,252</sup>.

UBQLN2 is also an autophagy adaptor. A motif within its ST11 block binds LC3, allowing attachment to autophagosome membranes, and UBQLN2 engages initiation factors to tether ubiquitinated cargo to growing phagophores. Particularly when proteasomes are overloaded or the cargo is too bulky for efficient proteasomal threading<sup>252,253</sup>. Loss or mutation reduces LC3-positive autophagosomes and delivery to lysosomes, underscoring UBQLN2's position at the decision point between the UPS and autophagy: readily degradable clients go to proteasomes, whereas larger assemblies or overload conditions divert to autophagy for bulk removal<sup>66,254</sup>.

Bottom line: UBQLN2 keeps proteostasis efficient by ensuring misfolded proteins reach the right destruction pathway. In neurons, this escort-and-triage function is crucial for axon-to-soma logistics and long-range quality control. Without it, distal stress may not be relayed effectively, allowing peripheral aggregates to build and propagate.

### **2.6.2 ALS/FTD-Linked UBQLN2 Mutations: Toxic Gain vs. Loss of Function**

UBQLN2 mutations appear to act through both toxic gain and loss of function, a gain of toxic aggregation together with a dominant-negative loss of shuttle activity. Most ALS/FTD-linked variants are missense or small insertions in the PXX repeat (e.g., P497S, P506T) that make UBQLN2 more self-aggregating and prone to enter stress granules<sup>17,66</sup>. In cells, mutant UBQLN2 forms cytoplasmic inclusions that recruit p62, ubiquitin, and sometimes TDP-43, whereas wild-type UBQLN2 remains mostly diffuse<sup>114</sup>. These inclusions are not harmless bystanders: transgenic mice expressing mutant UBQLN2 develop motor-neuron degeneration and cognitive deficits, confirming toxicity *in vivo*<sup>255</sup>. At the same time, the same mutations weaken UBQLN2's normal protein-protein interactions, e.g. reduced LC3 engagement impairs autophagy. Moreover, association of mutant UBQLN2 with the proteasome is poor, including weakened contact with subunits such as RPN11 that support shuttle function<sup>63,66,256</sup>. The mutant behaves as a "jammed shuttle," clumping, sequestering binding partners, and failing to deliver cargo, thereby hindering any remaining wild-type protein<sup>66</sup>.

Multi-omic and pathological readouts reinforce this dual mechanism. Mitochondrial proteins accumulate, ER-stress markers rise, and ER–Golgi cargo (including synaptic receptors) mislocalizes, indicating a broad proteostasis failure across organelles<sup>254,257</sup>. The most vulnerable cells, notably long motor neurons, show distal axon die-back in models, consistent with poor clearance of misfolded synaptic proteins at nerve

terminals<sup>255</sup>. In sum, UBQLN2 mutations deliver a double blow: mutants seed abnormal condensates while the network loses a key shuttle, driving a cascade of mis-sorted and undegraded proteins that selectively injures neurons already at proteostatic risk.

### **2.6.3 UBQLN2 Interaction with RNA-Binding Proteins (FUS, TDP-43)**

UBQLN2 works closely with phase-separating RNA-binding proteins (RBPs) such as FUS and TDP-43. Under stress it enters stress granules and other RNP droplets that contain these RBPs and behaves like a “liquid chaperone,” helping condensates stay mobile and timely in their turnover<sup>23,112</sup>. UBQLN2 interacts with multiple RBPs including FUS, TDP-43, and hnRNPA1, and has been shown to regulate stress granule dynamics. It modulates the phase separation behavior of FUS–RNA complexes, keeping droplets smaller and more fluid, thereby preventing the formation of aberrant, solid-like condensates<sup>23</sup>. When UBQLN2 is mutated or depleted, those FUS granules gel and persist, recruiting ubiquitin and p62 and eventually seeding aggregates<sup>66</sup>. The relationship with TDP-43 appears less direct. UBQLN2 does not strongly bind TDP-43’s RNA-recognition motifs, but it can recognize ubiquitinated TDP-43 species or C-terminal fragments through its UBA domain<sup>256</sup>. In ALS tissue, where such fragments accumulate in inclusions decorated with ubiquitin and p62, UBQLN2 often co-localizes with TDP-43, consistent with an attempted clearance role<sup>17</sup>. When UBQLN2 is functional, overexpression can lower cytosolic TDP-43. When mutated, it fails to remove TDP-43 and can co-aggregate with it, producing mixed inclusions seen in patient neurons<sup>256</sup>. Overall, UBQLN2 may “guard” RBP condensates: sensing ubiquitylation as a removal tag, extracting misfolded clients for proteasomes, or steering entire droplets to autophagy when they become persistent or overgrown. When this guardian is compromised, FUS and TDP-43 slip the leash and their droplets harden and mislocalize, and toxic aggregates accumulate.

### **2.6.4 UBQLN2 in Proteostasis Control**

UBQLN2 appears to act as a rheostat for neuronal proteostasis, patrolling phase-separated RNP condensates such as stress granules and slipping in and out of the liquid phase via its proline-rich PXX region without self-aggregating. Once inside, its UBA domain reads the ubiquitin chain architecture on client proteins and triages them: when components are transient and carry short or K48-linked chains that signal routine turnover, UBQLN2 engages the proteasome through its UBL domain to extract

individual misfolded clients, pruning the droplet and preserving its fluidity<sup>36,66</sup>. When assemblies are larger, longer-lived, or coated with K63-linked chains typically associated with aggregation, UBQLN2 flips to an autophagic program. Its LC3-interacting region, together with partners such as FIP200, recruits the core autophagy machinery and hands off the entire condensate for macroautophagic clearance<sup>42,66,72</sup>. In practice, this creates a graded decision rule: modest, short-lived stress is handled locally by proteasomal pruning, whereas severe or prolonged stress triggers bulk removal<sup>66</sup>.

This switching behavior seems to be tuned by ubiquitin density. Occupancy of the UBA by polyubiquitin likely nudges UBQLN2 into conformations that favor oligomerization and adaptor engagement (for example LC3 and FIP200), so high-density tagging biases the system toward autophagic handoff while lower density favors selective extraction. Rather than a simple on/off switch, UBQLN2 scales its response to the state of the condensate<sup>42,66</sup>.

## **2.7 Therapeutic Target Space**

This section is dedicated for emerging therapeutic strategies aimed at the proteostasis and phase-separation abnormalities in ALS/FTD<sup>65,72</sup>. Given that no traditional approach (e.g. small molecules targeting a single enzyme or pathway) has yet yielded an approved ALS/FTD therapy, there is intense interest in novel targets and broadly acting strategies to bolster protein homeostasis. This chapter surveys several avenues: enhancing proteasome activity, inducing autophagy, activating chaperone responses, and deploying engineered “degraders” (PROTACs, AUTACs, etc.). Each is in experimental stages, but collectively they paint an optimistic picture of attack points against the otherwise intractable proteinopathy of ALS/FTD<sup>54,55,72,258–261</sup>.

### **2.7.1 Proteasome Enhancers and the Risk of Off-Target Proteotoxicity**

Boosting proteasome activity can accelerate clearance of misfolded proteins<sup>55</sup>. Small molecules allosterically activate the 20S core (TCH-165 and AM-404 bind the  $\alpha$ -ring and hold the gate open) raising peptide entry and degradation in cells<sup>57,262,263</sup>. Others act on the 19S regulatory particle and its associated DUBs: IU1 inhibits USP14 (a deubiquitinase that can pause degradation), and b-AP15/VLX1570 inhibits USP14 and UCH37, shortening substrate dwell time and promoting destruction<sup>54,264,265</sup>.

In Huntington's, Parkinson's, and ALS models, these gate-openers and DUB inhibitors lower toxic proteins (e.g., mutant huntingtin,  $\alpha$ -synuclein) and improve cellular phenotypes and viability<sup>54,262,266</sup>. But there's a fine line between benefit and harm. Chronic overactivation can deplete free ubiquitin, disrupting other ubiquitin signaling pathways, and accelerate turnover of short-lived regulators (e.g. tumor suppressors, cell-cycle proteins). Broad activation may destabilize normally fast-turned-over proteins and trigger stress responses, likely because excess peptide fragments burden downstream peptidases and antigen-presentation pathways<sup>55,267,268</sup>. Thus, dose and context matter: moderate enhancement helps under proteinopathy conditions, whereas excessive activation can backfire.

Current efforts focus on selectivity. One direction is compounds that bias degradation toward intrinsically disordered or aggregate-prone substrates (e.g., TDP-43) while sparing structured, short-lived enzymes. Another is targeted delivery e.g., viral vectors or tissue-specific promoters to elevate proteasome activity mainly in motor neurons, limiting systemic exposure. Medicinal chemistry is probing allosteric pockets to fine-tune catalytic activities (selectively boosting caspase-like activity or acting under oxidative conditions). The objective is to enhance selectivity toward aggregate-prone proteins while avoiding a widespread increase in degradation that compromises essential cellular components<sup>55,262</sup>.

In summary, proteasome enhancement is promising but double-edged: Success depends on selective mechanisms, careful dosing, and precise delivery to preserve proteostasis while clearing toxic proteins central to ALS/FTD.

### **2.7.2 Autophagy Inducers: mTOR-Dependent versus Independent Routes**

On the autophagy side, there's strong interest in inducing autophagy to clear protein aggregates and damaged organelles in ALS/FTD. Approaches fall into two categories.

mTOR-dependent inducers: Inhibiting mTORC1 releases the brake on autophagy initiation. Rapamycin and rapalogs (e.g., everolimus) increase autophagic flux<sup>69</sup>. In ALS models, rapamycin reduced misfolded SOD1 and improved motor-neuron survival *in vitro*<sup>223</sup>. A small Phase II ALS study found rapamycin safe and well-tolerated, with biomarker hints (e.g., slower CSF neurofilament rise) but no significant clinical benefit at that size. Larger, longer trials would be needed<sup>269</sup>. Because rapamycin suppresses immunity and affects metabolism (mTORC1 regulates insulin signaling), long-term use

can raise lipids, cause mouth ulcers, and increase infection risk. To avoid systemic effects, brain-penetrant, neuron-biased mTOR inhibitors are being explored, including Torin-1–like compounds, CNS-focused low-dose rapalogs, and early ideas such as nanoparticle or prodrug delivery. The goal is to elevate neuronal autophagy while minimizing lymphocyte suppression or diabetic-like states<sup>69</sup>.

mTOR-independent enhancers: These act downstream or parallel to mTOR. Trehalose, a disaccharide, promotes autophagy via AMPK and stabilizes lysosomes. In ALS mice it lowered TDP-43 and improved p62 clearance, though blood-brain barrier penetration is modest and oral dosing may limit exposure<sup>270</sup>. SMER28 likely acts at the Vps34/PI3P step to enhance autophagosome formation even when mTORC1 is active<sup>271</sup>. Rilmenidine, an imidazoline-receptor agonist, induces autophagy through distinct signaling that may engage CMA and macroautophagy. A small ALS trial is underway<sup>272</sup>. Repurposed agents like lithium, carbamazepine, valproic acid lower inositol/IP3 to trigger autophagy<sup>273,274</sup>. Early combination studies hinted at slower progression, but larger trials were inconclusive and toxicity (especially lithium's narrow window) limits dosing.

Newer concepts are based on the following: Tat-Beclin-1 peptides directly activate the Beclin1–Vps34 complex and have boosted autophagy and aggregate clearance in cell models, though in-vivo delivery and safety are open questions<sup>275</sup>. Phospho-ubiquitin mimetics aim to mimic PINK1-generated pSer65-ubiquitin to trigger mitophagy more broadly, potentially improving removal of damaged mitochondria in ALS<sup>276,277</sup>.

Many inducers are FDA-approved or relatively low-toxicity, but delivery to neurons and sustained target engagement remain hurdles. Autophagy is a double-edged sword (too much can worsen wasting) so moderate, well-timed induction is the goal. Intermittent dosing schedules may help. Ongoing trials (e.g., rilmenidine) will test clinical impact. If effective, autophagy enhancement could complement proteasome-directed therapies, jointly targeting large aggregates and soluble misfolded proteins in ALS, where both clearance systems are impaired. Monitoring biomarkers will be important.

### **2.7.3 Chaperone / Heat-Shock Pathway Activators**

Another therapeutic approach is to boost the cell's own protein-folding defenses, the molecular chaperones and heat-shock proteins (HSPs). In ALS, chaperones such as

HSPB1 and the HSP70 family help prevent TDP-43 and FUS aggregation, so drugs that raise chaperone levels or activity are attractive<sup>149,226</sup>.

A leading example is arimoclomol, a co-inducer of heat-shock proteins that prolongs HSF1's binding to DNA and increases HSP70, HSP40, and HSPB8<sup>278,279</sup>. It reached Phase III in ALS (with emphasis on SOD1-ALS) after Phase II showed brain penetration and elevated HSP70 in patients. Although the Phase III primary endpoint was not met, sub-analyses are ongoing and expanded-access use continues. Arimoclomol appeared safe and engaged its target, suggesting dosing or timing may need refinement<sup>280</sup>.

Other heat-shock activators include celastrol (a plant triterpene) and quercetin (a flavonoid). By disrupting the Hsp90 complex that keeps HSF1 inactive, they free HSF1 to induce HSPs<sup>278,281</sup>. Both have shown neuroprotective effects in animal models but raise concerns: celastrol can cause oxidative damage at high doses. Quercetin is promiscuous across kinases and both can induce weight loss which is problematic in ALS<sup>278</sup>.

High-throughput screens have yielded small molecules like HSF1A that stimulate HSF1 transcription without full heat shock and reduced polyQ-huntingtin toxicity in flies by elevating HSP70<sup>279</sup>. Another angle is HDAC6 inhibition: HDAC6 helps maintain Hsp90 in a state that sequesters HSF1. Inhibiting HDAC6 hyperacetylates Hsp90, weakens its grip on HSF1, and promotes HSP transcription. Several HDAC6 inhibitors are in Alzheimer's trials and could be repurposed for ALS if they improve proteostasis<sup>281</sup>.

Anecdotally, a few ALS cases on cancer immunotherapies (which can induce high fever) showed unusually slow progression, hinting that repeated fever (and thus transient HSP upregulation) might be beneficial. It is not a practical therapy, but it underscores that the heat-shock response can be harnessed<sup>278</sup>.

Overall, chaperone enhancers seem reasonable from a safety standpoint because they augment an intrinsic stress response, but success will depend on achieving sustained exposure in the brain. Arimoclomol's short half-life requires frequent dosing. Long-term chaperone induction also carries unknowns, as excess HSP70 can, for example, inhibit apoptosis with uncertain consequences. Even so, enhancing these

“cellular lifeguards” remains compelling, particularly for TDP-43 proteinopathy, which resembles an acquired protein-misfolding stress<sup>279,280</sup>.

#### **2.7.4 Targeted Degradation: PROTACs and AUTACs**

Perhaps the most advancement in recent years is the rise of targeted protein degraders, drugs that don't just inhibit a protein but tag it for destruction. The two main flavors are PROTACs (Proteolysis-Targeting Chimeras) and AUTACs (Autophagy-Tethering Compounds)<sup>282</sup>.

PROTACs are bifunctional molecules: one end binds a protein of interest and the other recruits an E3 ubiquitin ligase. By forcing proximity, the ligase ubiquitinates the target, sending it to the proteasome<sup>282</sup>. PROTACs against tau (an Alzheimer's protein) achieved over 70% reduction of insoluble tau in primary neuron models and even reversed synaptic deficits in a tauopathy mouse model<sup>258,283</sup>. Similar efforts for mutant huntingtin and  $\alpha$ -synuclein are moving toward animal testing. In ALS, the main hurdle is finding effective ligands for proteins like TDP-43 or FUS, which are hard to engage with small molecules, though kinases and other regulators along ALS pathways may be more tractable. A key advantage is that PROTACs act catalytically: a single molecule can trigger degradation of many targets, achieving removal rather than just inhibition<sup>282</sup>.

AUTACs use a similar tag-and-remove concept but route targets to the autophagy system. One end binds the target (or even an organelle), and the other carries a tag that recruits autophagy machinery. AUTAC4, for example, directs damaged mitochondria to autophagosomes for clearance and has reduced markers of oxidative stress in cell and zebrafish models<sup>284</sup>. Compared with PROTACs, which work best on soluble cytosolic proteins, AUTACs may be better for larger structures and aggregates (such as persistent TDP-43 inclusions or stress granules) by leveraging bulk autophagic removal<sup>282</sup>.

However, obstacles remain. These chimeras are often large (roughly 500–1000 Da), which can hinder pharmacokinetics and brain penetration. Off-target effects require careful assessment, since a PROTAC could recruit unintended proteins with similar binding features. Rapid decoration of proteins with ubiquitin or other tags might also trigger immune responses during chronic dosing. Nonetheless, momentum is strong:

at least one PROTAC targeting a cancer protein is already in clinical trials, showing the approach has moved beyond the lab<sup>282,285</sup>.

In summary, the therapeutic landscape for proteostasis diseases like ALS/FTD is expanding. Traditional single-target inhibitors have struggled in ALS, but these newer approaches, activating cellular cleanup systems, enhancing chaperones, and directly tagging harmful proteins for destruction offer fresh hope. Advancing mechanistic understanding enables the development of targeted interventions that restore equilibrium between protein synthesis and degradation, with the potential to halt or reverse neurodegenerative processes. Each strategy brings challenges, yet the groundwork laid by fundamental research is now translating into tangible clinical experimentation. The coming decade will show which of these bold approaches can make the leap from bench to bedside for ALS and FTD patients.

### 3. Aims of this Study

Disruption of proteostasis is a central hallmark of many neurodegenerative diseases, including amyotrophic lateral sclerosis (ALS) and frontotemporal dementia (FTD). Among these disorders, the aggregation of the RNA-binding protein TDP-43 is especially prominent, occurring in the majority of ALS cases and in a large fraction of FTD cases. Pathological TDP-43 assemblies might reflect a failure of the cellular quality-control machinery, most notably the ubiquitin–proteasome system (UPS) and the autophagy–lysosome pathway, which under physiological conditions cooperate to degrade misfolded proteins and prevent toxic aggregation<sup>286–290</sup>

However, it remains unclear how exactly aberrant TDP-43 assemblies are recognized and triaged by these degradation systems, and whether their material properties influence the clearance route. Moreover, while genetic studies have linked several autophagy receptors and their cofactors to ALS/FTD<sup>291</sup>, the precise sequence of events by which these proteins participate in TDP-43 aggregate turnover is not fully resolved. Understanding these mechanisms is essential, as they define critical decision points between successful aggregate disposal and persistent inclusion pathology.

Against this background, the present study pursued three overarching aims:

1. To determine how soluble TDP-43 as well as TDP-43 condensates and aggregates are degraded by the UPS and autophagy–lysosome system.
2. To identify the receptor proteins and regulatory factors that mediate recognition and disposal of TDP-43 assemblies.
3. To assess whether the biophysical state of TDP-43 condensates / aggregates influences their clearance route.

By addressing these aims, this work sought to define how cellular quality-control networks respond to TDP-43 pathology, to identify key molecular players that govern TDP-43 aggregate disposal, and to provide a mechanistic framework for therapeutic strategies that boost proteostasis mechanisms for the treatment of ALS and FTD.



## 4 Material and Methods

### 4.1 Generation of Stable Cell Lines and Cell Culture and inhibitor treatment

Stable HeLa cell lines with doxycycline-inducible expression of EGFP-tagged TDP-43 wild-type (WT), TDP-43 with a mutated nuclear localization signal (NLSm: K82A, R83A, K84A, K95A, K97A, R98A), the TDP-43 C-terminal fragment (CTF; residues 220-414), FUS wild-type (WT), FUS-P525L, TurboID-3xHA-tagged TDP-43 CTF or TurboID-3xHA-tagged TDP-43 WT were generated using the Flp-In T-REx system. Parental HeLa Flp-In T-REx cells were cultured in Dulbecco's Modified Eagle Medium (DMEM), supplemented with 10% Tet-System Approved fetal bovine serum (FBS, Thermo Fisher Scientific, A4736401) and 100 µg/mL zeocin in a humidified incubator with 5% CO<sub>2</sub> at 37°C. For stable line generation, cDNAs encoding for EGFP-TDP-43 WT, EGFP-TDP-43-NLSm<sup>152</sup> and EGFP-TDP-43 CTF (aa. 220 – 414) were cloned into the pcDNA5/FRT/TO vector (Thermo Fisher Scientific) using Gibson assembly. The plasmids were co-transfected with pOG44 (Flp recombinase expression vector) into HeLa Flp-In T-REx cells using Lipofectamine 2000 according to the manufacturer's protocol. Stable integrants were selected with 150 µg/ml Hygromycin B and 15 µg/ml Blasticidin for 2-3 weeks. To isolate clonal populations, bulk-selected cells were induced with 1 µg/ml doxycycline for 24 hours and subjected to cell sorting (Invitrogen Bigfoot, IMB Mainz Flow Cytometry core facility) to isolate single EGFP-positive cells using a 100µm nozzle with 30 psi. Cells were sorted into 96-well plates and expanded. Individual clones were screened for doxycycline-inducible EGFP expression by Flow Cytometry (Novocyte Quanteon, IMB Mainz Flow Cytometry core facility), and positive clones were validated by Western blotting using an anti-GFP antibody (Proteintech, 66002-1-Ig) and by confocal microscopy. Stable cell lines exhibiting consistent expression levels and appropriate localization of TDP-43 constructs were used for subsequent experiments. They were cultured in DMEM supplemented with 10% Tet-approved FBS and 150 µg/ml Hygromycin B and 15 µg/ml Blasticidin at 37°C in 5% CO<sub>2</sub>. Expression was induced with 1 µg/ml doxycycline for 24 hours prior to experiments. Where indicated, cells were treated with 100 nM Bortezomib (Sigma-Aldrich, 5043140001), 100 nM Bafilomycin A1 (Cell Signaling Technology, 54645S), VER-155008 (Sigma, SML0271) or Torin1 (MedChemExpress, HY-13003) for the specified time period.

## **4.2 Protein Stability Assay and Analysis by Flow Cytometry**

To assess protein stability, different EGFP-TDP-43 expressing cell lines were treated with 100 µg/ml cycloheximide (CHX; Sigma-Aldrich) to inhibit protein synthesis either alone or combined with 100 nM Bortezomib or 100 nM Bafilomycin A1. At 0, 3, 6 and 9 hours post-treatment, cells were gently washed with PBS and detached using 0.05% trypsin-EDTA, with trypsin activity subsequently neutralized by addition of DMEM containing 10% FBS. Cell suspensions were processed through a standardized preparation protocol optimized for flow cytometry analysis. Cells were first pelleted by centrifugation at 500 × g for 5 minutes at 4°C and resuspended in Resuspension Buffer #1 (1× PBS containing 10% FBS, 2 mM sodium azide as a preservative, and 2 mM EDTA to prevent cell clumping). After a second centrifugation step at 400 × g for 5 minutes at 4°C, cells were washed in Resuspension Buffer #2 (1× PBS with 3% BSA, 2 mM sodium azide, and 2 mM EDTA) and centrifuged again under identical conditions. The final cell pellet was resuspended in fresh Resuspension Buffer #2 for immediate analysis. Flow cytometry was performed using a Novocyte Quanteon (Agilent) (IMB Mainz, Flow Cytometry core facility) with 488 nm excitation and 530/30 nm emission filters for EGFP detection. For each sample, a minimum of 10,000 events were acquired at a controlled flow rate. Flow Cytometry results were analyzed using FlowJo™ v10.7.1 software (BD Life Sciences). Sequential gates were applied to identify intact cells, single cells, viable (DAPI-negative) cells, and EGFP-positive cells based on non-induced controls. Mean fluorescence values were normalized to the baseline (0 hour) time point for each experimental condition. Appropriate controls, including unstained cells and non-induced samples, were included in each experiment to establish background fluorescence levels and enable proper gating during data analysis.

## **4.3 Immunofluorescence Staining**

All steps were performed at room temperature (RT). Cells were fixed with 4% paraformaldehyde in PBS for 7 minutes, then permeabilized with 0.1% Triton X-100 in PBS for 5 minutes. Non-specific binding was blocked with 1% donkey serum in PBST (PBS with 0.1% Tween-20) for 10 minutes. Cells were incubated overnight at 4°C with primary antibodies diluted according to manufacturer's instructions in blocking solution. After three washes with PBST, a species-appropriate secondary antibody conjugated to Alexa Fluor 647 was applied at 1:1000 dilution PBST for 1 hour protected from light.

After three washes with PBST, DNA was stained with DAPI (Sigma, D9542) at 0.5 µg/ml in PBS for 5 min. After two washes with PBS, samples were ready for image acquisition in the Revvity Opera Phenix high-throughput confocal microscope system (see below under “Confocal Microscopy”).

The following primary antibodies were used: mouse anti-Ubiquitin antibody (Sigma-Aldrich, 04-263), rabbit anti-phospho-Ser409/410-TDP-43 (Proteintech, 80007-1-RR), rabbit anti-G3BP1 antibody (Proteintech, 13057-2-AP), rabbit anti-Vimentin antibody (Proteintech, 10366-1-AP), rabbit anti-LC3 antibody (Proteintech, 14600-1-AP), rabbit anti-Lamp1 antibody (Cell Signaling, 9091T), rabbit anti-NBR1 (Proteintech, 16004-1-AP), rabbit anti-p62/SQSTM1 (Proteintech, 80294-1-RR), -rabbit anti-WIP1 (Proteintech, 28820-1-AP) rabbit anti-Optineurin (Proteintech, 60293-1-Ig), rabbit anti-TAX1BP1 (Proteintech, 14424-1-AP), rabbit anti-VCP (Proteintech, 60316-1-Ig), rabbit anti-UBQLN2 (Proteintech, 23449-1-AP), rabbit anti-PSMA1 antibody (Proteintech, 11175-1-AP). The following secondary antibodies were used: anti-mouse-IgG-AI.647 (Invitrogen, A-31571), anti-rabbit-IgG-AI.647 (Invitrogen, A-31573).

#### **4.4 Confocal Microscopy**

For analysis by confocal microscopy, cells were plated in 96-well plates (Greiner Bio-One, 655090) and after experimental perturbations, they were fixed with 4% paraformaldehyde in PBS for 7 minutes at RT, then permeabilized with 0.1% Triton X-100 in PBS for 5 min. High-content imaging was performed on a Revvity Opera Phenix high-throughput confocal microscope system (IMB Mainz Microscopy core facility) using a 63× water immersion objective (NA 1.15). For each well, multiple non-overlapping fields were acquired using consistent laser power and exposure settings across all experimental conditions. Image acquisition parameters were optimized to avoid saturation while maintaining sufficient signal-to-noise ratio.

#### **4.5 Image quantification and analysis**

Quantitative analysis of condensate number and size was performed using ilastik (version 1.3.3) for automated image segmentation and object classification. Quantitative analysis of condensate fluorescence intensity was performed using Revvity Harmony™ Software. A minimum of 100 cells per condition were analyzed across four independent biological replicates. Statistical analysis of condensate

number and size distributions was performed using GraphPad Prism 9 using unpaired t-test.

#### **4.6 Fluorescence Recovery After Photobleaching (FRAP) and FRAP analysis**

FRAP experiments were performed on live HeLa cells expressing EGFP-TDP-43 CTF after 6 or 24 hours of treatment with 100 nM Bortezomib. Cells were plated on  $\mu$ -Slide 8-well glass-bottom chambers (Ibidi, 80827) and maintained at 37°C with 5% CO<sub>2</sub> during imaging. Experiments were conducted on a Leica Stellaris 8 Falcon confocal microscope (IMB Mainz Microscopy core facility) equipped with a 63 $\times$  oil immersion objective (NA 1.4). A circular region within condensates was photobleached using a 488 nm laser at 5% power (5 iterations). Fluorescence recovery was monitored every 2 seconds for 120 seconds.

Data were normalized to pre-bleach intensity using easyFRAP (<https://easyfrap.vmnnet.upatras.gr><sup>292</sup>), and the area under the recovery curve (AUC) was calculated for each time course using GraphPad Prism 9. Statistical comparisons of AUC values between conditions were performed using unpaired two-tailed t-tests. Data were collected from 7 condensates per condition across three independent experiments.

#### **4.7 Biochemical Fractionation**

Cells were washed twice with ice-cold PBS and lysed in RIPA buffer (50 mM Tris-HCl pH 8, 150 mM NaCl, 1% NP-40, 0.5% sodium deoxycholate, 0.1% SDS) supplemented with ReadyShield Protease Inhibitor Cocktail (Sigma-Aldrich, PIC0004), PhosSTOP phosphatase inhibitors (Roche, 04906837001) and 25 U/mL Benzonase nuclease (IMB). Lysates were incubated on ice for 10 minutes with intermittent vortexing, sonicated for 30 seconds (Bioruptor Pico, Diagenode), and centrifuged at 16,000  $\times$  g for 10 minutes at 4°C. The supernatant (RIPA-soluble fraction) was collected, and the pellet was washed once with RIPA buffer, resonicated, and recentrifuged. The final pellet (RIPA-insoluble fraction) was solubilized in urea buffer (7 M urea, 2 M thiourea, 4% CHAPS, 30 mM Tris-HCl pH 8.6). After addition of 4x Lämmli buffer and boiling for 5 min, equal amounts of both fractions were loaded onto a 10% SDS-PAGE gel and subsequently were analyzed by Western blotting with rabbit anti-TDP-43 (Proteintech, 12892-1-AP).

#### **4.8 Quantification of soluble fraction**

Western blot quantitative analysis was performed by extracting the optical densities of each band using the software Image Studio Lite (LI-COR), using the top and bottom average background option, to obtain the signal value, in which local background is automatically subtracted.

Analysis of RIPA-Benzonase fractionation experiments was performed by dividing the signal values of (I) by the total (S+I) signal values, to obtain a I/(S+I) ratio, respectively. Statistical analysis was performed using GraphPad Prism with using unpaired t-tests.

#### **4.9 Live-Cell Imaging**

For live cell imaging, cells were plated on a 96 well plate (Sarstedt, 83.3924) and time-lapse imaging was performed on an IncuCyte SX5 system (Sartorius, IMB Mainz Microscopy core facility) with a 20× objective, acquiring images every 30 minutes for 24 hours.

#### **4.10 siRNA Knockdown**

Cells were reverse-transfected on day 0 while plating cells with 10 nM ON-TARGETplus siRNA (Dharmacon) targeting NBR1 (L-010522-00-0005), p62/SQSTM1 (J-010230-05-0002) or WIPI2 (J-020521-09-0002) or with 10 nM custom siRNA targeting TDP-43 (sequence: 5'- ggcucaagcauggauucuaagucuu-3') using Lipofectamine RNAiMAX (Invitrogen) in Opti-MEM, following the manufacturer's instructions. For partial knockdown of NBR1 and WIPI2, only 2 nM siRNA was used. After 48 hours, cells were lysed and knockdown efficiency was analyzed by Western blotting using rabbit anti-NBR1 (Proteintech, 16004-1-AP), rabbit anti-p62/SQSTM1 (Proteintech, 80294-1-RR) and rabbit anti-WIPI2 (Proteintech, 28820-1-AP) and rabbit anti-TDP43 (Proteintech, 80001-1-RR) primary antibodies, or cells were fixed and processed for confocal imaging as described above.

#### **4.11 Cell lysates and Western blot**

Cells were washed twice with ice-cold PBS and lysed in RIPA buffer (50 mM Tris-HCl pH 8, 150 mM NaCl, 1% NP-40, 0.5% sodium deoxycholate, 0.1% SDS) supplemented

with ReadyShield Protease Inhibitor Cocktail (Sigma-Aldrich, PIC0004) and PhosSTOP phosphatase inhibitors (Roche, 04906837001). Lysates were incubated on ice for 10 minutes with intermittent vortexing, sonicated for 30 seconds (Bioruptor Pico, Diagenode), and centrifuged at  $16,000 \times g$  for 10 minutes at  $4^{\circ}\text{C}$ . The supernatant (RIPA-soluble fraction) was collected and after addition of 4x Lämmli buffer, boiled for 5 min. Samples were loaded onto a 10% SDS-PAGE gel and subsequently analyzed by Western blotting with rabbit anti-TDP-43 (Proteintech, 12892-1-AP), rabbit anti-NBR1 (Proteintech, 16004-1-AP), rabbit anti-p62/SQSTM1 (Proteintech, 80294-1-RR), anti-WIP1 (Proteintech, 28820-1-AP) and rabbit anti-GAPDH (Proteintech, 60004-1-Ig) antibodies.

#### **4.12 Sample preparation for BioID samples**

For BioID experiments, stable HeLa cells expressing doxycycline-inducible TurboID-3xHA-TDP-43 CTF or TurboID-3xHA-TDP-43 WT, cultured as described above, were subjected to proximity labeling by addition of  $50 \mu\text{M}$  biotin (Sigma-Aldrich, B4501) to the culture medium for 60 min.

Following biotinylation, cells were washed twice with ice-cold PBS and lysed in RIPA buffer (50 mM Tris-HCl pH 8, 150 mM NaCl, 1% NP-40, 0.5% sodium deoxycholate, 0.1% SDS) containing ReadyShield Protease Inhibitor Cocktail (Sigma-Aldrich, PIC0004) and PhosSTOP phosphatase inhibitors (Roche, 04906837001). Lysates were incubated for 45 minutes at  $4^{\circ}\text{C}$  with gentle agitation and clarified by centrifugation at  $1,000 \times g$  for 5 minutes at  $4^{\circ}\text{C}$ . The supernatant was incubated with pre-equilibrated streptavidin magnetic beads (Thermo Fisher Scientific, 88816) for 1 hour at  $4^{\circ}\text{C}$  with end-over-end rotation. Beads were washed stringently to reduce nonspecific interactions: once with RIPA buffer, three times with 4 M urea and 1% SDS in PBS (Wash Buffer 1), once with 1% SDS in PBS (Wash Buffer 2), and twice with RIPA buffer. Biotinylated proteins were eluted by boiling the beads in 25 mM Tris-HCl pH 8, 1% SDS, 10 mM DTT, 10 mM biotin at  $95^{\circ}\text{C}$  for 15 minutes, followed by magnetic separation of the eluate. Samples were processed using the SP3 approach<sup>293</sup>. Proteins were reduced in 5 mM DTT, alkylated in 15 mM iodoacetamide in the dark and quenched in 5 mM DTT. Trypsin was used to digest proteins overnight at  $37^{\circ}\text{C}$ . Following acidification by formic acid, the peptide solution was purified through solid phase extraction in C<sub>18</sub> StageTip<sup>294</sup>.

#### **4.13 MS data acquisition for BiID of TDP-43 WT and TDP-43 CTF**

LC-MS/MS analysis was performed on an Orbitrap Exploris480 mass spectrometer (Thermo Fisher, IMB Mainz Proteomics Core Facility) coupled to an Easy-nLC UHPLC system (Thermo Fisher). Peptides were separated using a 55-cm reverse phase column (inner diameter: 75  $\mu\text{m}$ ; ReproSil-Pur 120 C<sub>18</sub>-AQ 1.9- $\mu\text{m}$  silica particles, Dr. Maisch GmbH) across a gradient from 5 to 22% in 40 minutes, 22 to 32% in 23 minutes and from 32 to 40% in 10 minutes (buffer A: 0.1% (v/v) formic acid; buffer B: 0.1% (v/v) formic acid, 80% (v/v) acetonitrile) at a flow rate of 250 nl/min. The DDA data acquisition mode was set to perform one MS1 scan followed by a maximum of 15 dependent scans for the top 15 most intense peptides with MS1 scans (R=60,000 at 400 m/z, normalized AGC (%)=300 and max. IT set to 28ms), HCD fragmentation (NCE=30%), isolation windows (1.4 m/z) and MS2 scans (R=15,000 at 400 m/z, normalized AGC (%)=100 and max. IT set to 40ms). A dynamic exclusion of 25s was applied and charge states lower than two and higher than seven were rejected for the isolation, the MIPS mode was set to "Peptide".

#### **4.14 MS data acquisition for BiID of TDP-43 CTF treated with BZT and BafA1**

LC-MS/MS analysis was performed on an Orbitrap Astral mass spectrometer (Thermo Fisher) coupled to a Vanquish Neo liquid chromatography system (Thermo Fisher). Peptides were separated using a 45-cm reverse phase column (inner diameter: 75  $\mu\text{m}$ ; ReproSil-Pur 120 C<sub>18</sub>-AQ 1.9- $\mu\text{m}$  silica particles, Dr. Maisch GmbH) across a linear gradient from 5 to 40% in 31 minutes (buffer A: 0.1% (v/v) formic acid; buffer B: 0.1% (v/v) formic acid, 80% (v/v) acetonitrile). The mass spectrometer was operated in data-independent acquisition (DIA) with the following parameters: one full FTMS scan in Orbitrap (350–1,050 m/z) at 120,000 resolution, 20 ms injection time, and AGC target (%)= 300, followed by 174 fixed windows of 4Da from 350.4092 to 1050.7274 m/z at 30,000 resolution, 5 ms injection time, and AGC target (%)= 500 (Astral detector). Precursor ions were fragmented with HCD, Normalized Collision Energy 26%, isolation window 4m/z.

#### **4.15 Data analysis for BiID of TDP-43 WT and TDP-43 CTF**

Acquired spectra were searched using the MaxQuant software package version 2.4.13 embedded with the Andromeda search engine<sup>295</sup> against the Human Proteome

reference dataset (<http://www.uniprot.org/>, downloaded on 01.18.2024, 20'414 proteins) extended with contaminant list, TURBO id and reverse decoy sequences. The search parameters were set to include only full tryptic peptides, maximum two missed cleavage, carbamidomethyl as static peptide modification, oxidation (M) and deamidation (N-ter) as variable modification and “match between runs” option. The MS and MS/MS mass tolerance was set to 20 ppm, and a False discovery rate of < 1% was used at PSM and Protein level. Protein identified with at least 2 peptides were considered and the abundance was determined from the intensity of top two peptides. Intensity values of 4'806 proteins identified in triplicate in at least one condition were log<sub>2</sub> transformed, normalized by the median intensity per run and imputed using random sampling from a normal distribution generated 1% less intense values. ANOVA statistical analysis was employed to compare multiple conditions (control minus Biotin, TDP-43 WT and CTF). The entire dataset, including raw data, generated Tables and scripts used for the data analysis are available in the PRIDE repository (PXD063884).

#### **4.16 Data analysis for BioID of TDP-43 CTF treated with BTZ and BafA1**

Acquired DIA spectra were search using MSFragger computational platform version 22.0<sup>296,297</sup>), Philosopher version 5.1.1<sup>298</sup>. Peptide identification from MS/MS spectra was performed with MSFragger search engine against the Human Proteome reference dataset (<http://www.uniprot.org/>, downloaded on 01.18.2024, 20'414 proteins) extended with contaminant list, TURBO id and reverse decoy sequences. Mass tolerance was set to 20 ppm for precursor and for fragment ions. The search parameters were set to include fully tryptic peptides, allowing for up to one missed cleavage-sites, carbamidomethylation on cysteine residues as static modification and up to three variable modification including methionine oxidation and N-terminal acetylation. Peptide and protein inference was FDR controlled at 1% by PeptideProphet and ProteinProphet respectively. The generated library included entries for 169'750 peptide precursors and 8465 protein groups. For the DIA analysis, extraction of quantitative data was performed with DIA-NN version 1.8.2 beta 8 with a maximum FDR of 1% and quantification strategy was set to “Robust LC”.

Protein group identified in triplicate in at least one condition plus Biotin were considered (8'219). Protein intensities > 0 were log<sub>2</sub> transformed and median normalized and the missing values (3.9%) were imputed from a normal distribution around a value that is 3 (log<sub>2</sub>) lower than the mean intensity of the non-missing condition for each protein.

Next, ANOVA statistical analysis was conducted to identify proteins enriched in the presence of biotin compared to the no-treatment condition for each treatment group (untreated, Bortezomib 6 hrs and 24 hrs, Bafilomycin A1 6 hrs, 12 hrs, and 24 hrs). Proteins significantly enriched ( $\log_2FC > 1$  and  $p\text{-value} < 0.05$ ) in at least one condition were considered as candidate interactors (1'192).

In the next step, hierarchical clustering was performed to identify candidate interactors exhibiting similar profiles in response to proteasome and lysosome inhibition. To ensure specificity, only positive and significant fold changes related to the no-biotin treatment were considered, while null values were imputed for all other conditions. Pearson correlation coefficients were computed for all candidate interactors across the dataset, and hierarchical clustering using Ward's method ( $k = 7$ ) was performed based on the Jaccard distance of all interactors. GO analysis was performed with Enrichr using the list Cellular Component 2018<sup>299</sup>

For each identified cluster, we calculated the recovery of Protein–Protein Interactions (PPIs) annotated in BioGRID (version 4.4.216.;<sup>300</sup>) and compared them with those calculated for random cluster generated from the list of candidate interactions. Only physical interactions identified in at least two experiments were considered. Two generated distributions were assayed for normality with Shapiro test and tested with Mann-Whitney U test ( $N=7$ ).

For the characterization of Cluster 2, the top 30 GO terms<sup>299</sup> were selected, considering only those with at least five associated genes. To ensure a single protein assignment per GO term, proteins linked to multiple terms were assigned to the one with the lowest p-value. This data was then integrated with interaction annotations from BioGRID (version 4.4.216), where the link width represents the number of experiments in which the interaction was documented. The entire dataset, including raw data, generated Tables and scripts used for the data analysis are available in the PRIDE repository (PXD063899).

All gene ontology analysis were performed using the R package EnrichR<sup>299</sup> considering as background the list of candidate interactors.

#### **4.17 Immunohistochemistry (IHC) Staining**

Formalin-fixed, paraffin-embedded (FFPE) sections were prepared from the frontal cortex and hippocampus. Sections were deparaffinized in xylene and rehydrated through a graded ethanol series. To quench endogenous peroxidase activity, sections

were treated with 0.3% hydrogen peroxide in methanol for 10 minutes. Antigen retrieval was performed by pressure cooking in citrate buffer (pH 6.0) for 10 minutes. Non-specific binding sites were blocked using 10% dried milk in Tris-buffered saline with Tween-20 (TBS-T). Sections were then incubated with the following primary antibodies: p62 (80294-1, Proteintech; 1:1000) or NBR1 (16004-1; Proteintech: 1:200) overnight at 4 °C. Following primary antibody incubation, sections were treated with a biotinylated anti-rabbit or anti-mouse IgG secondary antibody (1:200, 30 min, DAKO) at room temperature, followed by incubation with an avidin–biotin complex (30 min, Vector Laboratories). Immunoreactivity was visualized using 3,3'-diaminobenzidine (DAB) activated with hydrogen peroxide, as previously described<sup>301</sup>.

#### **4.18 Correlative Cryo-ET**

Stable HeLa EGFP-TDP-43 CTF cells were cultured as mentioned above. For cryo-ET experiments, cells were switched to DMEM high glucose HEPES medium without phenolred (Thermo Scientific, 21063029) for robust fluorescence detection in cryo-conditions. The cells were seeded in 8-well  $\mu$ -Slide dishes (Ibidi, 80826) onto EM grids (Au SiO<sub>2</sub> R1/4, mesh 200, Quantifoil) that were glow-discharged twice for 90s using Pelco easiGlow device and pre-treated with 1  $\mu$ g/mL human fibronectin in PBS (Sigma-Aldrich, F0895) for 1h under UV-light. One day after cell seeding, EGFP-TDP-43 CTF expression was induced with doxycycline. The next day, condensate formation was triggered with 100 nM BTZ) and after 24 hours, the grids with cells were taken out of the 8-well dish and directly vitrified with 3.5  $\mu$ L of diluted autofluorescent 1  $\mu$ m diameter Dynabeads (Thermo Scientific, acid65011) after 6.5s blotting time at 37°C and 70% relative humidity in liquid ethane (at -184°C) using an EM GP2 plunger (Leica Microsystems). The EM grids were clipped into specialized autogrids rings with a cut-out window suitable for cryo-FIB-milling. GFP-CTF-TDP43 fluorescence was observed using the integrated fluorescence light microscope (iFLM) of the Aquilos cryo-focused ion beam-scanning electron microscope (cryo-FIB-SEM) (Thermo Scientific) using the 488 nm channel (2% laser intensity, 30ms exposure per slice, z-stack height of 6  $\mu$ m, 15 slices). After correlation of the fiducial beads from the fluorescence 2D projection image with the grid's respective SEM overview image in the MAPS Software (Thermo Scientific), the optimal areas for lamella milling were selected. A protective layer of organometallic platinum was deposited on the grid for 45s. Semi-automatic FIB-milling was carried out at 8° milling angle using the AutoTEM software (Thermo Scientific).

The ion beam current and distance was decreased between milling patterns to obtain a final lamella thickness of 150–200 nm, similar to<sup>302</sup>.

Tilt series were acquired in a Titan Krios G2 (Thermo Scientific) cryo-transmission electron microscope operated at 300 kV and equipped with a Gatan Bioquantum-K3 imaging filter, an energy slit set to 20 eV, and Gatan K3 direct electron detector at a nominal magnification of X42,000, corresponding to 2.176Å/px using SerialEM v.4.1.13<sup>303</sup>. Tilt series acquisition was started at the lamella pre-tilt of +8° and went through the tilt range from -52° to +68° in a dose-symmetric scheme with 2° increments<sup>304</sup>, resulting in 61 projections with a total dose of 140-150 e/Å<sup>2</sup>. The defocus was cycled through from -3.5 μm to -5 μm.

#### **4.19 Tomogram reconstruction, segmentation and template matching**

The motion-corrected tilt series were corrected for dose exposure and and projections of low quality were removed after visual inspection. The tilt series was then aligned and reconstructed using weighted back-projection using AreTomo2 v1.0.0 (PMID: 35601683). Tomogram denoising at bin4 (8.704Å/px) was done using cryoCARE (PMID: 31326025). Automatic membrane segmentation of the tomograms was carried out using MemBrain-Seg<sup>305,306</sup>. For segmentation of the amorphous condensate structures, the U-net deep-learning based segmentation in Dragonfly v.2022.1 was used<sup>307</sup>. The tomograms were also reconstructed in Warp<sup>308</sup> using the alignments generated by AreTomo2 for easier compatibility with the sub-tomogram averaging workflow using Relion v.3.1<sup>309</sup>. Ribosomes were template matched at bin4 using Gapstop TM<sup>310,311</sup> with a previously generated 80S ribosome template. The top hits were extracted and sub-tomograms were exported using Warp. The sub-tomograms were then averaged using Relion v.3.1 and the coordinates/angles from the 3D refinement were used to place the particles back into the tomogram using ArtiaX<sup>312</sup>. All visualization of the membrane/condensate segmentation and ribosome particles was done using ChimeraX v.1.9<sup>313</sup>. The reconstructed tomogram was displayed using IMOD v.4.10.51<sup>314</sup>.

## 4.20 Electrophoretic mobility shift assays

The Stem loop RNA from the SON transcript gene (GGAUCUUUAACUACUCAAGAUACUGAACAUUGACAUGGUA) and the TDP-3'UTR FRG.2-SITE RNA (GAGAGAGCGCGUGCAGAGACUUGGUGGUGCAUAA) was chemically synthesized with the addition of a Cy5-label (Metabion). 2 nM of Cy5-labeled RNA was mixed with fixed amounts of TDP-43 wt (0.2  $\mu$ M) or FUS wt (0.3  $\mu$ M) and varying amounts of UBQLN2 (0-0.6  $\mu$ M). Binding reactions (20  $\mu$ L) were incubated in binding buffer (20 mM NaPO<sub>4</sub> [pH8], 150mM NaCl, 5% glycerol, 1 mM DTT, 5 mM MgCl<sub>2</sub> 0.5 mg/mL BSA, 0.1 mg/mL yeast tRNA, 1U/ $\mu$ L RNase inhibitor (Thermo Fisher) for 20 min at RT before loading onto a 1 mm thick non-denaturing polyacrylamide gel (6%) in 0.5 x TBE. Gels were run at 100 V for 40 min at RT. Gels were imaged with a Bio-Rad ChemiDoc MP Imaging system.

## 4.21 Protein expression and purification

### 4.21.1 UBQLN2

UBQLN2 was expressed in *E. coli* Rosetta 2 cells grown in LB medium with 50  $\mu$ g/ml kanamycin and 33  $\mu$ g/ml chloramphenicol at 37 °C until OD600 reached 0.8, followed by induction with 1 mM IPTG and overnight incubation at 16 °C. Cells were lysed in buffer (50 mM Tris-HCl pH 8.0, 150 mM NaCl, 20 mM imidazole, 10% glycerol, 4 mM  $\beta$ -mercaptoethanol, 0.1 mg/ml RNase A, 1 mM MgCl<sub>2</sub>) using high-pressure homogenization. Protease inhibitors were added post-lysis. Proteins were purified by Ni-NTA agarose (Qiagen) and bound proteins were treated with benzonase (250 U/ml) overnight at 4 °C to remove nucleic acids. UBQLN2 was eluted with buffer containing 600 mM imidazole and further purified by size exclusion chromatography (SEC; NGC Quest 10 Plus, BioRad) in storage buffer (20 mM Tris-HCl pH 8.0, 150 mM NaCl, 10% glycerol, 2 mM DTT, or alternatively 20 mM Na-phosphate pH 6.8, 0.5 mM EDTA). Peak fractions were pooled, concentrated with Amicon Ultra-15 (30 kDa cutoff), flash frozen in liquid nitrogen, and stored at -80 °C.

### 4.21.2 TDP-43-MBP-His6

TDP-43-MBP-His6 was expressed in *E. coli* Rosetta 2 cells grown in LB medium with 50  $\mu$ g/ml kanamycin and 33  $\mu$ g/ml chloramphenicol at 37 °C until OD600 reached 0.6–0.8, followed by induction with 0.5 mM IPTG and overnight incubation at 16 °C. Cells

were lysed in buffer (20 mM Tris-HCl pH 8.0, 1 M NaCl, 10 mM imidazole, 10% glycerol, 4 mM  $\beta$ -mercaptoethanol, 0.1 mg/ml RNase A, and 1  $\mu$ g/ml aprotinin, leupeptin, and pepstatin A) using lysozyme and sonication. The clarified lysate was purified by Ni-NTA agarose (Qiagen) and eluted with buffer containing 300 mM imidazole. Eluted proteins were subjected to SEC (Hiload 16/600 Superdex 200 pg, GE Healthcare) in storage buffer (20 mM Tris-HCl pH 8.0, 300 mM NaCl, 10% glycerol, 2 mM TCEP). Fractions corresponding to monomeric TDP-43-MBP-His6 were pooled, concentrated, flash frozen in liquid nitrogen, and stored at  $-80^{\circ}\text{C}$ .

#### **4.21.3 MBP-FUS-His6/MBP-FUS-EGFP-His6**

MBP-FUS-His6 wild-type or MBP-FUS-EGFP-His6 were expressed in *E. coli* BL21-DE3 Rosetta LysS cells grown in LB medium at  $37^{\circ}\text{C}$  until OD600 reached  $\sim 0.8$ , followed by induction with 0.1 mM IPTG and incubation for 22 h at  $12^{\circ}\text{C}$ . Cells were lysed in buffer (50 mM NaPO<sub>4</sub> pH 8.0, 300 mM NaCl, 10  $\mu$ M ZnCl<sub>2</sub>, 40 mM imidazole, 10% glycerol, 4 mM  $\beta$ -mercaptoethanol) using sonication. Proteins were purified by tandem-affinity chromatography on Ni-NTA agarose (Qiagen) and amylose resin (NEB), and eluted with buffer containing 250 mM imidazole and 20 mM maltose, respectively. Eluted proteins were dialyzed into storage buffer (20 mM NaPO<sub>4</sub> pH 8.0, 150 mM NaCl, 5% glycerol, 1 mM DTT), concentrated, flash frozen in liquid nitrogen, and stored at  $-80^{\circ}\text{C}$ . Protein concentrations were determined by absorbance at 280 nm using ProtParam-predicted extinction coefficients, with A<sub>260/280</sub> ratios of 0.6–0.7.

#### **4.22 Microscopic condensate assay**

Purified full-length wild-type (WT) UBQLN2 was diluted to the indicated concentrations in 20 mM sodium phosphate buffer (pH 6.8) containing 0.5 mM EDTA and either 50 mM or 150 mM NaCl. Samples were prepared in PCR tubes and transferred into ibiTreat  $\mu$ -Slides (ibidi) for droplet imaging by widefield microscopy. Prior to imaging, samples were incubated at  $37^{\circ}\text{C}$  for 20 min.

Phase separation of MBP-tagged FUS WT was performed in 50 mM Tris-HCl (pH 8.0), 1 mM DTT, 0.5 mM EDTA, and 150 mM NaCl. Where indicated, 40 U/ $\mu$ l RNase inhibitor was included for assays containing RNA. Samples were pre-mixed in PCR tubes in the presence or absence of 1  $\mu$ M SON-GGU RNA. To induce phase separation, tobacco etch virus (TEV) protease was added directly to the  $\mu$ -Slide chambers to cleave the

MBP solubility tag. Following cleavage, samples were incubated at room temperature for 20 min before imaging.

Droplet formation of FUS WT was analyzed by phase-contrast microscopy, while widefield fluorescence microscopy was used for FUS WT constructs C-terminally tagged with enhanced green fluorescent protein (EGFP).

## **5. Results – Part A**

This chapter is part of a submitted manuscript:

Yongwon Suk, Federico Uliana, DeLong Li, Simone Mosna, Christian Behrends, Florian Wilfling, Tammaryn Lashley, Dorothee Dormann. “Cytosolic TDP-43 condensates are cleared by the autophagy machinery in a WIPI2-dependent manner”

### **5.1 Cytosolically mislocalized TDP-43 and TDP-43 C-terminal fragments form cytosolic condensates upon proteasome inhibition**

To investigate turnover of TDP-43, we created stable HeLa cells inducibly expressing EGFP-tagged TDP-43 wild-type (WT), TDP-43 with a mutated nuclear localization signal (NLSm) or a C-terminal fragment (CTF) of 25 kDa that is known to arise in the

brains of ALS/FTD patients<sup>219,222</sup> (Fig. 5A, Fig. S1A). After induction of EGFP-TDP-43

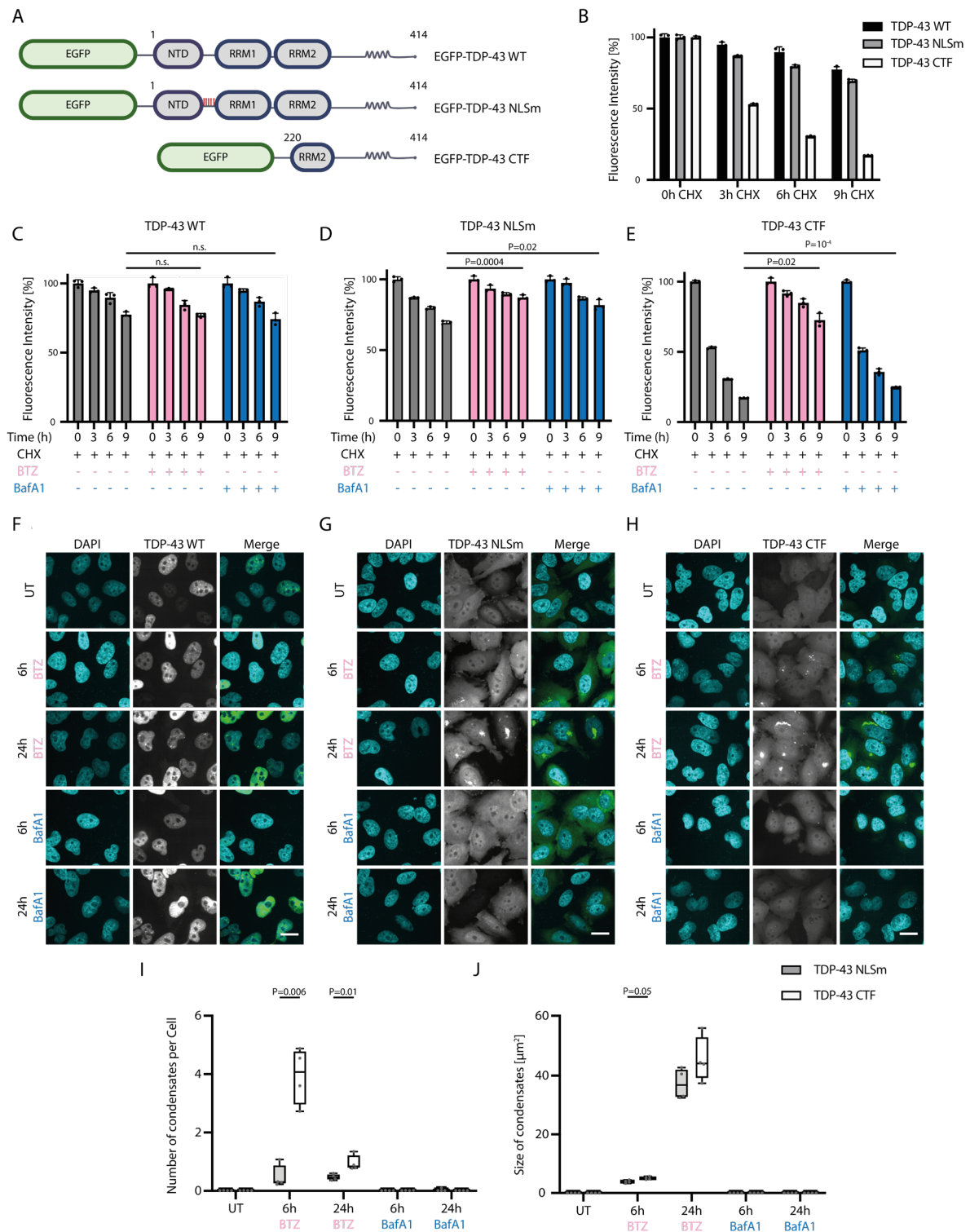


**Figure 5: Cytosolically mislocalized TDP-43 and TDP-43 C-terminal fragments (CTF) form cytosolic condensates upon proteasome inhibition.**

**A** Schema of N-terminally EGFP-tagged TDP-43 variants: wild-type (WT), nuclear localization signal mutant (NLSm, indicated by red lines), and C-terminal fragment (CTF; residues 220–414). TDP-43 comprises a folded N-terminal domain (NTD), two RNA recognition motifs (RRM1/2) and a C-terminal low complexity region that is largely intrinsically disordered, with a short helical region.

**B** Turnover kinetics of EGFP-TDP-43 variants measured by flow cytometry after treatment of cell lines with cycloheximide (CHX) for 3, 6 or 9 h. Bars indicate EGFP fluorescence intensities (mean  $\pm$  SD; n = 3 replicates).

**C–E** Turnover kinetics of EGFP-TDP-43 variants measured as in B, with proteasome inhibitor (Bortezomib, BTZ) or lysosomal acidification inhibitor (Bafilomycin A1, BafA1) present during the CHX treatment period. Quantification of EGFP fluorescence intensity (mean  $\pm$  SD; n = 3) by flow cytometry. Statistical significance was determined by unpaired t-test comparing the 9h CHX + inhibitor condition to 9h CHX alone.

**F–H** Confocal microscopy of HeLa cells expressing the indicated EGFP-tagged TDP-43 variants either untreated (UT) or after 6 or 12h BTZ or BafA1 treatment (DAPI: nuclei in cyan; EGFP-TDP-43 variants in green in the merge). Scale bars: 15  $\mu$ m.

**I–J** Quantification of condensate number and size [ $\mu$ m<sup>2</sup>, log scale] in TDP-43 NLSm and CTF cell lines under different treatment conditions. Box plots show the median and interquartile range (IQR) with whiskers extending from minimum to maximum values across 100 cells per replicate (4 independent replicates). Statistical significance was determined by unpaired t-test.

expression with doxycycline, we treated cells with cycloheximide (CHX) to block protein synthesis and measured EGFP levels by flow cytometry to assess stability of the different TDP-43 variants over a period of 9 hours. TDP-43 WT levels declined only slowly, whereas cytosolically mislocalized TDP-43 NLSm was turned over slightly more rapidly, and TDP-43 CTF levels strongly declined over the 9-hour period (Fig. 5B). To investigate whether the turnover was mediated by the proteasome or the autolysosomal system, we treated cells with a proteasome-specific inhibitor (Bortezomib, BTZ) or an inhibitor of the lysosomal V-type ATPase (Bafilomycin A1, BafA1) during the CHX treatment. Turnover of TDP-43 WT was not affected by proteasome or lysosome inhibition (Fig. 5C), whereas TDP-43 NLSm was slightly stabilized by BTZ as well as by BafA1 treatment (Fig. 5D). The rapid turnover of the TDP-43 CTF was efficiently blocked by the proteasome inhibitor, but was only slightly attenuated by BafA1 (Fig. 5E). Confocal microscopy demonstrated that localization of TDP-43 WT was unaffected by both treatments (Fig. 5F), whereas small cytosolic TDP-43 NLSm or CTF puncta/condensates formed after proteasome inhibition, but not upon lysosomal inhibition (Fig. 5G, H). These condensates were small ( $\sim$ 5  $\mu$ m<sup>2</sup> in a confocal slice) and mainly observed in the TDP-43 CTF line after 6h of BTZ treatment, whereas much larger ( $\sim$ 40  $\mu$ m<sup>2</sup>) condensates were seen for the TDP-43 CTF and less frequently for the NLSm after 24h of proteasome inhibition (Fig. 5I, J). To determine whether cytosolic condensate formation upon proteasome inhibition is also seen for other disease-linked RNA-binding proteins, we generated HeLa cell lines stably expressing EGFP-tagged FUS wild-type (WT) or the cytosolic FUS P525L mutant. Following BTZ treatment, neither FUS WT nor FUS P525L formed cytosolic condensates, as assessed by confocal microscopy (Fig. S1B). These findings indicate that the ability to form cytosolic condensates upon proteasome inhibition is a specific property of cytosolically mislocalized TDP-43. Taken together, our results demonstrate that cytosolically mislocalized TDP-43, and in particular CTFs of TDP-43, are selectively

degraded by the proteasome, and upon proteasome inhibition form cytosolic condensates, a phenomenon that was not observed for a cytosolic FUS mutant. As TDP-43 CTFs showed the strongest proteasome-dependent turnover and formed large cytosolic condensates upon proteasome inhibition in almost all cells, we used the TDP-43 CTF cell line for all subsequent experiments.

## **5.2 Proteasome inhibition induces amorphous non-fibrillar TDP-43 CTF condensates that acquire markers of TDP-43 pathology**

To investigate whether the cytosolic TDP-43 condensates formed after proteasome inhibition resemble inclusions seen in brains of ALS/FTD patients, we co-stained for pathognomonic markers of TDP-43 inclusions<sup>19,315,316</sup>. Immunostaining with antibodies against total ubiquitin and TDP-43 S409/S410 phosphorylation revealed strong colocalization of both pathology markers with TDP-43 CTF condensates formed after 6h and 24h of BTZ treatment (Fig. 6A, S2A). As proteasome inhibition is known to induce proteotoxic stress and stress granules, we examined whether TDP-43 CTF condensates colocalize with the stress granule marker G3BP1. However, no G3BP1 co-localization with TDP-43 CTF condensates was observed, demonstrating that the BTZ-induced TDP-43 CTF condensates are distinct from stress granules (Fig. 6A). Furthermore, proteasome inhibition is known to cause formation of aggresomes, which are large, juxtannuclear vimentin-encaged inclusions formed through transport of ubiquitylated misfolded proteins along microtubules to the centrosome<sup>317</sup>. Since monomeric TDP-43 has been reported to accumulate in aggresomes upon proteasome inhibition<sup>318</sup>, we co-stained BTZ-treated TDP-43 CTF cells for the aggresome marker vimentin. However, no vimentin cage, which would be typical for an aggresome, was seen around TDP-43 CTF condensates, neither after 6h nor 24h BTZ treatment (Fig. 6A, S2A). We thus conclude that the BTZ-induced TDP-43 CTF condensates are neither stress granules nor aggresomes, but most likely form due to the inherent condensation/aggregation propensity of the TDP-43 CTF.

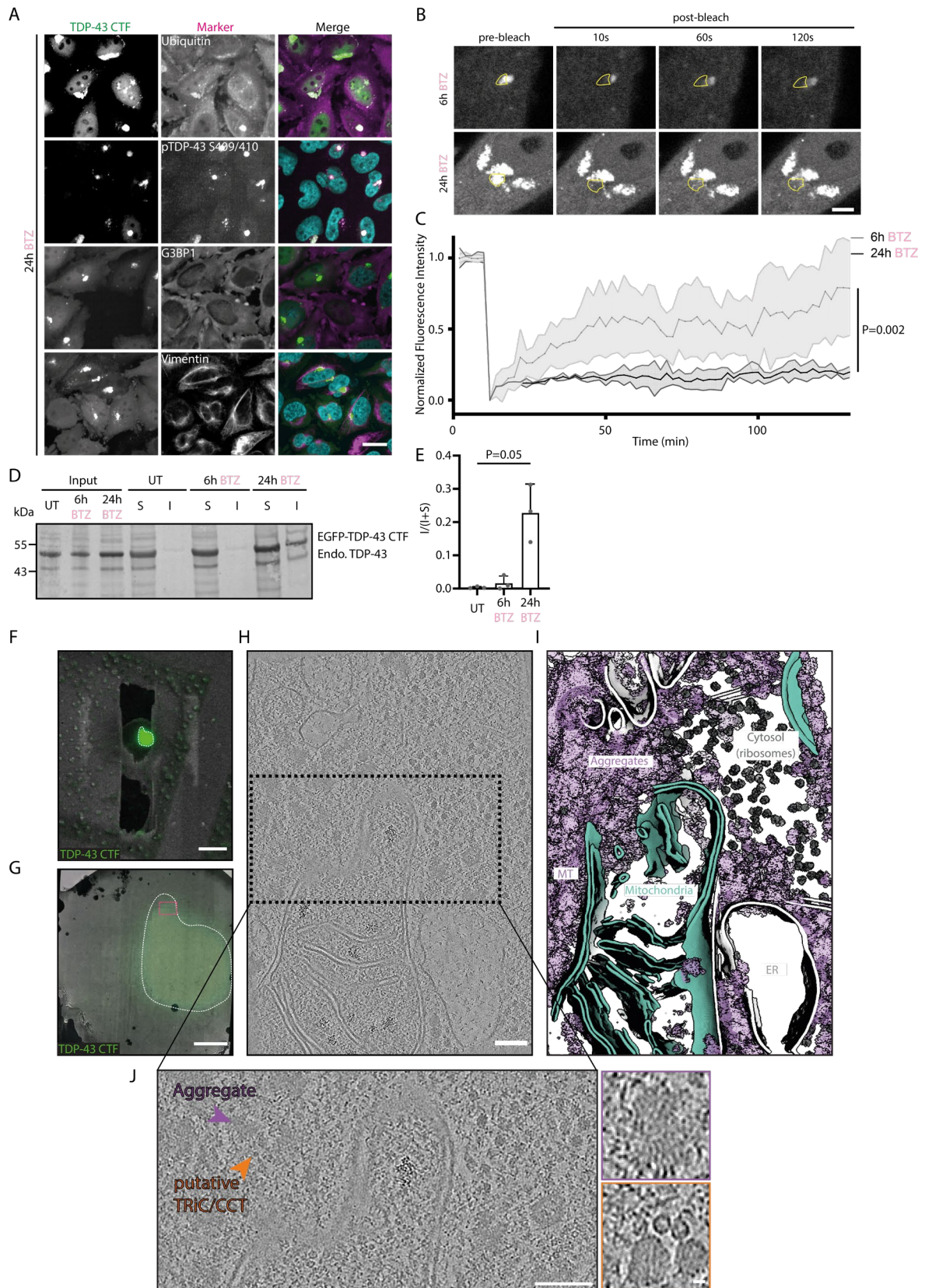


**Figure 6: Proteasome inhibition induces amorphous, non-fibrillar TDP-43 CTF condensates with reduced dynamics and partial insolubility.**

**A** Immunostaining of EGFP-TDP-43 CTF condensates (green in the merge) with antibodies specific to Ubiquitin (FK2), phospho-S409/410-TDP-43, G3BP1 or Vimentin (magenta in the merge) after 24h BTZ treatment. Nuclei (DAPI) are shown in cyan in the merge. Scale bar: 15  $\mu$ m

**B** FRAP (fluorescence recovery after photobleaching) of EGFP-TDP-43 CTF condensates after 6h or 24h BTZ treatment. Bleached region indicated by yellow circle and recovery monitored over 120 s. Scale bar: 5  $\mu$ m.

**C** FRAP curves after bleaching of EGFP-TDP-43 CTF condensates in 6 h or 24 h BTZ-treated cells. Values represent mean  $\pm$  SD from analysis of 7 condensates per condition. Statistical comparison was performed using an unpaired t-test on the area under the curve (AUC) calculated for each independent condensate \*P < 0.002.

**D** Biochemical fractionation into RIPA-Benzonase-soluble (S) and RIPA-Benzonase-insoluble (I) fractions to analyze solubility of EGFP-tagged TDP-43 CTF and endogenous TDP-43 after BTZ treatment. Detection was performed by Western blotting with a TDP-43-specific antibody.

**E** Quantification of EGFP-TDP-43 CTF solubility, plotted as I/(I + S) ratio. Values represent mean  $\pm$  SD from four independent replicates. Statistical significance determined by one-way ANOVA with Dunnett's multiple comparison test.

**F** Cryo-ET of HeLa cells expressing GFP-TDP-43 CTF after 24h of BTZ treatment. Scanning electron microscope (SEM) image of polished lamella with the GFP-TDP-43 CTF fluorescence overlaid. The condensate/aggregate structure is indicated with dashed lines. Scale bar: 15  $\mu$ m.

**G** Overview map of an exemplary lamella (from F) imaged in cryo-TEM overlaid with the GFP fluorescence. Tilt series acquisition site is marked with a pink box. Scale bar: 3  $\mu$ m.

**H-I** Representative denoised tomographic slice of TDP-43 CTF condensate/aggregate *in situ* showing amorphous protein densities next to cellular structures (left). Tomogram segmentation with the amorphous protein densities marked in light purple ribosomes in dark grey. Cellular organelles are indicated (mitochondria, MT=microtubules, ER=endoplasmic reticulum). Scale bar: 100 nm.

**J** Zoom-in of condensate/aggregate structures in tomogram (purple arrow/box) and putative TRiC/CCT chaperonin complexes (orange arrow/box). Scale: 10 nm.

Next, we investigated the biophysical properties of TDP-43 CTF condensates formed after proteasome inhibition. To assess the dynamics of TDP-43 CTF molecules in condensates formed after 6h or 24h of BTZ treatment, we performed fluorescence recovery after photobleaching (FRAP) experiments, in which a portion of a condensate was bleached with a high intensity laser and fluorescence recovery in the bleached region was monitored over time (Fig. 6B). We observed partial fluorescence recovery in 6h old condensates within 2 minutes, whereas 24h old condensates barely showed any recovery during this time frame, indicating reduced molecular exchange in older and larger structures (Fig. 6C). Next, we examined the solubility of TDP-43 CTF condensates by lysis of cells in RIPA-Benzonase buffer, followed by a high-speed spin and separation of the cell lysates into a soluble (S) and insoluble (I) fraction. Western blot analysis showed that the TDP-43 CTF as well as endogenous TDP-43 were soluble in RIPA-Benzonase buffer in untreated and 6h BTZ-treated cells, but became partially insoluble after 24h of BTZ-treatment (Fig. 6D,E), further demonstrating that TDP-43 CTF condensates have aggregate-like features.

To characterize the structural organization of TDP-43 CTF condensates /aggregates after 24h BZT, we performed *in situ* 2D correlative cryo-electron tomography (cryo-ET). Cells were grown on EM grids, and vitrified after induction of TDP-43 CTF and treatment with BZT for 24h (Fig S2B). After vitrification, condensates were localized

using the integrated fluorescence microscope (iFLM) of the cryo-FIB/SEM to target them for cryo-FIB-milling (Fig. 6F, G). Thin (100–200 nm) lamellae were prepared at these sites and tilt series were acquired in a cryo-transmission electron microscope. After tomogram reconstruction TDP-43 CTF condensates exhibited an amorphous architecture without fibrillar organization (Fig 6H, Fig S2B), consistent with prior reports<sup>319</sup>. Template matching and subsequent sub-tomogram averaging showed that ribosomes were excluded from the condensate areas (Fig 6I), mirroring observations in other aggregate pathologies<sup>320,321</sup>. In contrast to ribosomes, microtubules and ER could span across the condensate. Furthermore, based on visual inspection, we observed putative TRiC/CCT chaperonin complexes, in proximity to the condensate (Fig 6J), suggesting a potential engagement of this chaperone system with TDP-43 CTF condensates.

In summary, we demonstrate that prolonged periods of proteasome inhibition induce formation of undynamic and partially insoluble TDP-43 CTF condensates, which show an amorphous architecture without fibrillar organization but nevertheless exhibit hallmarks of ALS/FTD-linked TDP-43 aggregates, including ubiquitination and C-terminal phosphorylation.

### **5.3 TDP-43 CTF condensates are cleared by the autophagy-lysosome pathway requiring Hsp70 activity**

Next, we sought to investigate whether the large, amorphous TDP-43 CTF condensates are irreversible aggregates, or whether they can still disassemble or be cleared by the cellular degradation machinery. To this end, we first induced the formation of TDP-43 CTF condensates by treating cells with BTZ for 24 hours, then washed out the inhibitor-containing medium and replaced it with fresh medium and monitored the cells for another 24h using live cell fluorescence microscopy (Fig. 7A). During this 24h time window, TDP-43 CTF condensates disappeared completely, indicating that they either disassemble or get degraded, or their disappearance reflects a combination of both disassembly and degradation.

To determine whether the disappearance of TDP-43 CTF condensates involves degradation by the autophagy-lysosome pathway, we performed BTZ washout experiments, including treatment with BafA1, to block lysosomal degradation. BTZ washout led to complete disappearance of the large TDP-43 CTF condensates.

However, washout in the presence of BafA1 resulted in the formation of numerous small cytosolic TDP-43 puncta (Fig. 7B). Immunostaining for LC3, a marker protein for autophagic membranes, showed strong co-localization with these newly formed small TDP-43 structures (Fig. 3B left), suggesting that they are autophagosomes or autolysosomes and that TDP-43 CTF condensates can get cleared by autophagy. To determine whether the small TDP-43/LC3-positive puncta also carry markers of lysosomes, we co-stained them for LAMP1, a marker of lysosomal membranes. As expected, LAMP1 was strongly recruited to the small TDP-43 CTF structures formed after BafA1 treatment (Fig. 7B right), further supporting that they are autolysosomal structures containing TDP-43 CTF and that TDP-43 CTF condensates can eventually be cleared by autophagic-lysosomal degradation. Line-scan analysis indicated both co-localization and adjacent positioning of LAMP1 relative to TDP-43 CTF condensates (Fig. 7C), likely reflecting BafA1-induced blockade of autophagosome-lysosome fusion. We hypothesized that condensate fragmentation involving chaperones might be a prerequisite for autophagic targeting, as smaller condensates could be more efficiently degraded.

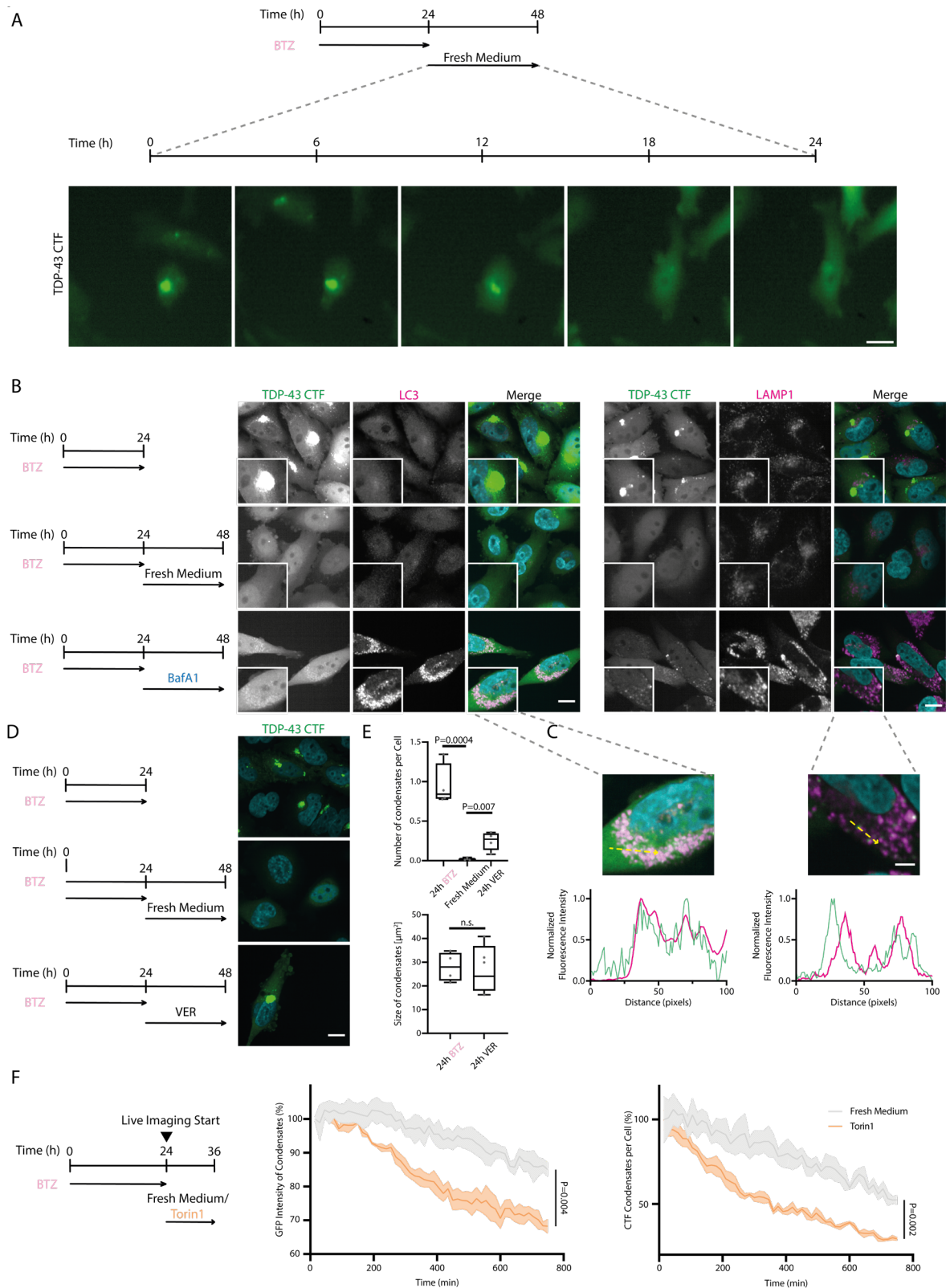


**Figure 7: TDP-43 CTF condensates are cleared by the autophagy-lysosome pathway requiring Hsp70 activity.**

**A** Live-cell imaging of EGFP-TDP-43 CTF condensates induced by 24h BTZ treatment during washout for 24h in fresh medium. Representative still images were captured at 0, 6, 12, 18, and 24 hours during the washout period. Scale bar: 20  $\mu\text{m}$ .

**B** Confocal images of EGFP-TDP-43 CTF (green in the merge) co-stained either with anti-LC3 antibody (left, magenta in the merge) or anti-LAMP1 antibody (right, magenta in the merge) after the treatments indicated in the scheme to the left. Nuclei (DAPI) are shown in cyan in the merge. Scale bar: 15  $\mu\text{m}$ .

**C** Confocal images of zoomed merged channels from B with line scan analysis of EGFP-TDP-43 CTF and LC3/LAMP1 signals, respectively. Line graph shows normalized fluorescence intensity against distance of line in pixels.

**D** Confocal images of EGFP-TDP-43 CTF (green in the merge) after the treatments indicated in the scheme to the left (VER = Hsp70 inhibitor). Nuclei (DAPI) are shown in cyan in the merge. Scale bar: 15  $\mu$ m.

**E** Quantification of number and size of condensates under the different treatment conditions from D. Box plots show the median and interquartile range (IQR) with whiskers extending from minimum to maximum values across 100 cells per replicate (4 independent replicates). Statistical significance was determined by unpaired t-test.

**F** Live cell imaging of EGFP-CTF condensates induced by 24h BTZ treatment during washout in fresh medium or medium supplemented with Torin1 (autophagy stimulator). EGFP fluorescence intensity was monitored over 12h. Data were normalized to the 0h time point to quantify relative EGFP intensity in condensates or relative condensate number per cell. Statistical analysis compared the area under the curve (intensity) or total counts (condensate number) using an unpaired t-test.

To test this, we performed washout experiments in presence of the Hsp70 inhibitor VER. Indeed, Hsp70 inhibition significantly impaired condensate clearance, with persistent condensates retaining their original size (Fig. 7D, E). This suggests that Hsp70-mediated fragmentation may facilitate autophagic degradation of TDP-43 CTF condensates. Next, we investigated whether pharmacological induction of autophagy can enhance clearance of TDP-43 CTF condensates. Thus, we performed BTZ washout experiments in the presence of Torin-1, an mTOR inhibitor that promotes autophagy, and monitored TDP-43 CTF condensates by live cell confocal microscopy over a period of 12 hours (Fig. 7F). Autophagy stimulation by Torin-1 led to a stronger decrease in EGFP fluorescence intensity within condensates or condensate number compared to washout with normal medium, indicating accelerated clearance of TDP-43 CTF condensates upon autophagy induction. Taken together, our data suggest that TDP-43 CTF condensates can get cleared by an autophagolysosomal route, involving Hsp70-mediated fragmentation, and that this pathway can be promoted by autophagy-stimulating drugs.

#### **5.4 Proximity proteomics reveals dynamic changes in the proteasome and autophagy network during TDP-43 CTF condensation and clearance**

Next, we sought to identify proteins linked to TDP-43 CTF condensation upon proteasome inhibition and clearance of TDP-43 CTF condensates via the autophagolysosomal route. To achieve this, we first performed siRNA-mediated knockdown of endogenous TDP-43 to prevent interference, and identified transient TDP-43 CTF interactors by a proximity labeling-based proteomics approach (BioID)<sup>322,323</sup> in stable HeLa cell lines inducibly expressing TurboID-HA-tagged TDP-43 CTF. We employed a BioID approach to investigate proteins in close proximity to TDP-43 (with a BirA labeling radius of approximately 20 Å), enabling the identification

of transient and low-abundant components that are near the bait (contextual information), even though they may not necessarily be direct physical interactors. Immunostaining demonstrated that the TurboID-HA-tagged protein also forms cytosolic condensates upon BTZ treatment (Fig. 8A), and Western blot analysis confirmed an efficient biotinylation reaction upon addition of biotin, as indicated by the characteristic biotinylation smear, confirming the suitability of this approach (Fig. 8B).

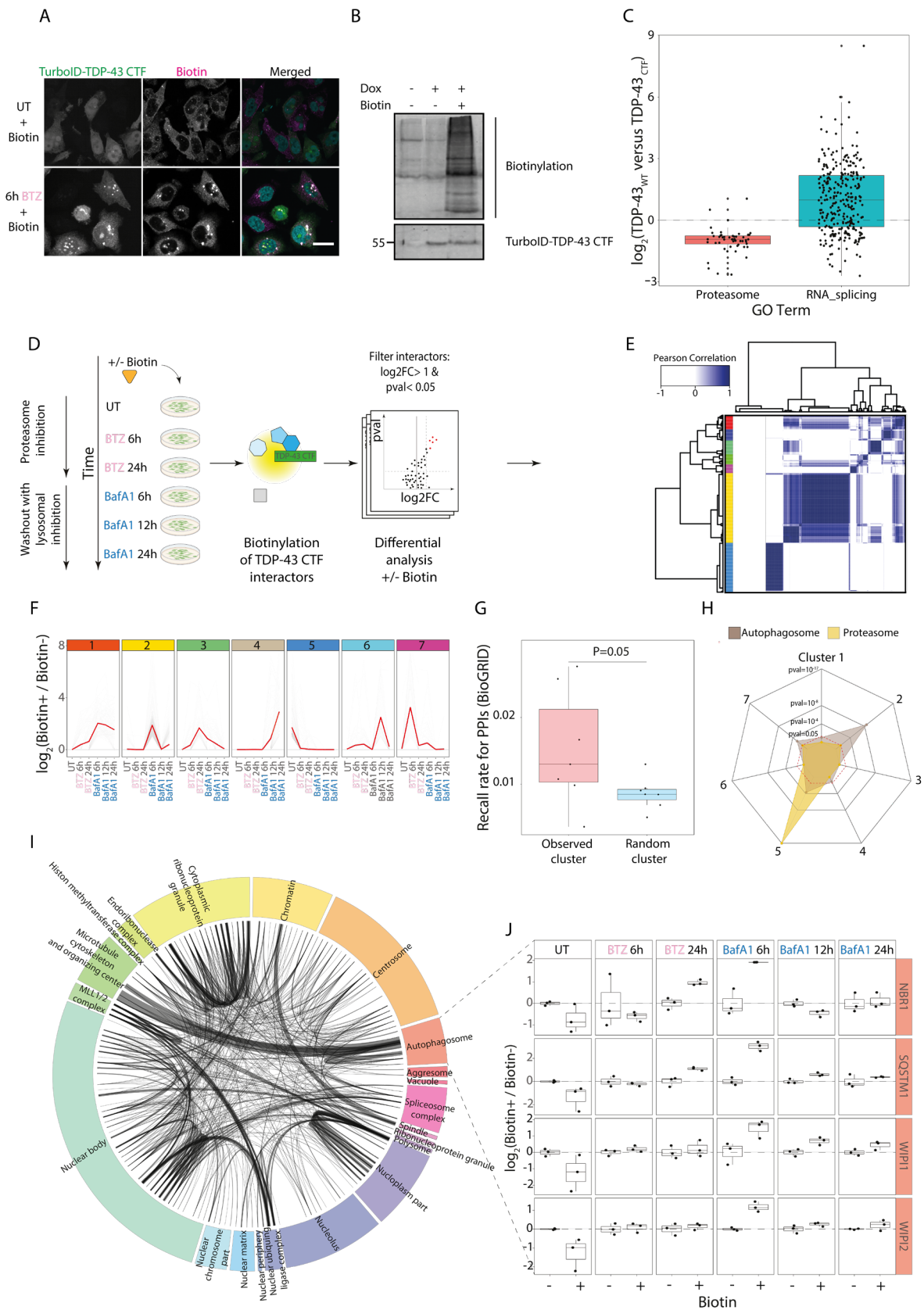


**Figure 8: Proximity proteomics of TurboID-tagged TDP-43 CTF reveals dynamic changes in the proteasome and autophagy network during TDP-43 CTF condensation and clearance**

**A** Immunostaining of TurboID-3xHA-TDP-43 CTF (green in the merge) and biotinylation signal (magenta in the merge) upon biotin treatment with and without BTZ treatment for 6h. Nuclei (DAPI) are shown in cyan in the merge, scale bar: 15  $\mu$ m.

**B** Western blot of TurboID-3xHA-TDP-43 CTF expression and biotinylation smear after biotin treatment. TurboID-3xHA-TDP-43 CTF was detected using an anti-HA-specific antibody and biotinylation was detected using an anti-Streptavidin Antibody.

**C** Comparison between TDP-43 WT and CTF interactome. Boxplot showing the differential abundance of proteasome proteins (GO:0000502) and RNA splicing proteins (GO:0008380) in the TDP-43 WT vs. CTF pulldowns. N=3 independent replicates. The boundaries of the box plot correspond to the quantiles Q1 (25%) and Q3 (75%). Lower and upper whiskers are defined by  $Q1 - 1.5IQR$  and  $Q3 + 1.5IQR$ .

**D** Workflow for characterizing the TDP-43 CTF interactome and its time-resolved reorganization upon proteasome (BTZ) or lysosome acidification (BafA1) inhibition. Cells were treated with BTZ or BafA1 for the indicated time periods, with and without biotin (control). Proteins in proximity to TDP-43 CTF were biotinylated and enriched using streptavidin beads. Candidate interactors significantly enriched in at least one biotin-treated condition ( $\log_2FC > 1$  and  $p\text{-value} < 0.05$ ) were clustered using an unsupervised approach to identify proteins with similar responses to proteasome and lysosome acidification inhibition.

**E** Unsupervised hierarchical clustering of TDP-43 CTF candidate interactors. Dendrogram of hierarchical clustering based on the Jaccard similarity of candidate interactors levels following treatment with BTZ and BafA1.

**F** Profile of the clusters identified by unsupervised hierarchical cluster (E). Individual protein profiles are shown in light grey, while the average profile is displayed in red.

**G** Recall rate for protein-protein interaction (PPIs) pairs (based on BioGRID v. 4.4.216) in observed clusters and in random clusters (controls). The significance was calculated based on Mann-Whitney U test (N=7). The boundaries of the box plot correspond to the quantiles Q1 (25%) and Q3 (75%). Lower and upper whiskers are defined by  $Q1 - 1.5IQR$  and  $Q3 + 1.5IQR$ .

**H** Radar plot, showing the enrichment of Autophagy terms in cluster 2 and Proteasome Terms in cluster 5, respectively (GO: 0005776 and GO: 0000502). Statistical significance was tested using a hypergeometric test and is indicated by the red line ( $P = 0.05$ ).

**I** Characterization of physical relationships (PPIs) between proteins identified in cluster 2. In the circus plot, proteins are clustered based on the GO term with higher significance. Links between proteins represents previously annotated interactions (BioGRID v. 4.4.216), with connection width proportional to the number of reported identifications (only physical interactions were considered).

**J** Profile abundance for proteins identified in cluster 2 linked to autophagy. Protein abundance for SQSTM1, NBR1, WIPI1 and WIPI2 are normalized to the average of the minus biotin untreated condition (N =3). The abundance of other proteins linked to autophagy identified in cluster 2 are shown in Fig. S4I. The boundaries of the box plot correspond to the quantiles Q1 (25%) and Q3 (75%), the average value is represented by a line across the center of the box. Lower and upper whiskers are defined by  $Q1 - 1.5IQR$  and  $Q3 + 1.5IQR$ .

First, we characterized proteins in proximity to TDP-43 WT and compared them to the CTF fragment. For all BioID experiments, to identify candidate interactors specific for each condition, we performed pair-wise differential abundance analysis comparing samples treated and not treated with Biotin. Proteins in proximity to TurboID-tagged TDP-43 were labeled by a biotin ligase and affinity-purified based on biotin tagging. For TDP-43 WT, differential analysis comparing conditions with and without biotin is presented in the Volcano plot (Fig. S3A). As expected, TDP-43 was highly enriched ( $\log_2FC \sim 6$ ) compared to the control (Fig S3A,B), furthermore about 60% of the enriched proteins ( $\log_2FC > 1$  and  $p\text{-value} < 0.05$ ) are involved in RNA splicing (Fig. 4C/Supp Table 1), and the vast majority is linked to DNA and RNA binding (Fig. 8C, S3C,D), in line with published TDP-43 interactomes<sup>244,319,324–328</sup>. Comparison of proximity partners between WT and CTF revealed an interactome re-arrangement for the CTF proteoform, with an enrichment of proteins associated with the proteasome, and a loss of RNA splicing proteins (Fig. 8C), in line with a prior report<sup>319</sup>.

Next, we tracked dynamic rearrangement of TDP-43 CTF proximity interactors during condensation (0h, 6h, 24h of BTZ treatment) and during BTZ washout with lysosomal V-type ATPase inhibition (6h, 12h, 24h post-BTZ with BafA1). Pulldowns were examined by mass spectrometry (MS) using the Data Independent Acquisition (DIA) method, identifying 8219 proteins generating a matrix with high completeness (quality controls are reported in Fig. S3E-G). Proteins enriched significantly compared to the “no biotin” control (ANOVA,  $\log_2FC > 1$  and  $p\text{-value} < 0.05$ ) in at least one condition were filtered (1192 proteins) and unsupervised hierarchical clustering based on protein correlation profiles was employed to identify proteins exhibiting similar behavior in response to proteasome and lysosomal inhibition (Fig. 8D). This approach led to the identification of seven clusters of proteins (Fig. 8E) showing distinct profiles after treatment (Fig. 8F). To provide evidence of the biological relevance of the identified clusters, we verified that protein pairs within each cluster have been reported in PPIs database (Biogrid v. 4.4.216<sup>300</sup>) significantly more frequently than those observed in randomly generated clusters (Fig. 8G).

Cluster analysis demonstrates that proteins associated with the proteasome (cluster 5) (Fig. 8H) progressively decrease during the condensation and clearance process (Fig. 8F, see Fig. S4A for profile of all proteasome complex members). This finding is in agreement with our result that the TDP-43 CTF is preferentially degraded by the proteasome in its diffuse state (Fig. 5). In contrast, autophagy-related proteins were enriched in cluster 2 (Fig. 8H), characterized by a peak at the early washout phase (6h BafA1 treatment), followed by a subsequent decrease (Fig. 8F). This suggests that the autophagy machinery is recruited during the early phases of TDP-43 CTF condensate clearance. Next, we explored physical association among proteins identified in Cluster 2 (Fig. 8I). The majority of proteins in cluster 2 are linked to nuclear components likely caused by translocation and being sequestered/trapped within TDP-43 CTF condensates. These are followed by proteins linked to cytoplasmic ribonucleoprotein granule, autophagosome and aggresomal components, including the autophagy receptors p62/SQSTM1 and NBR1, components involved in autophagosome formation (WIPI1, WIPI2) (Fig. 8J) as well as other autophagy-linked proteins (Fig. S4B), pinpointing a key role of these factors in the selective autophagic degradation of condensed TDP-43 CTFs. Proteins identified in this cluster are highly interconnected, revealing a striking association between the autophagosome and the microtubule cytoskeleton and organizing center (MTOC), including KEAP1, a substrate receptor for

the KEAP1-CUL3-RBX1 ligase complex, which mediates SQSTM1 ubiquitination and degradation activity<sup>329</sup>. Within this cluster, we also identified proteins with chaperone functions capable of binding unfolded protein fragments, including CCT8, a component of the TRiC (TCP-1 Ring Complex)<sup>330</sup> and small heat shock proteins (Fig. S4C). In summary, proximity proteomics using TurboID-tagged TDP-43 CTF pinpoint a re-arrangement of potential TDP-43 CTF interactors, with dynamic and sequential recruitment of proteasomal and autophagic factors during the condensation and degradation process, respectively. Our findings suggest that proteasomal degradation is favored in the diffuse state, whereas the autophagy machinery is recruited to TDP-43 CTF condensates for clearance in the condensed, insoluble state. Key autophagy receptors, including p62/SQSTM1 and NBR1, as well as autophagosome formation factors (WIPI1 and WIPI2), are preferentially associated with the late-stage condensates and the initial phase of clearance, supporting a model in which autophagy takes over TDP-43 CTF degradation under conditions of proteasome inhibition and TDP-43 condensate formation.

### **5.5 Autophagy receptor p62/SQSTM1 promotes TDP-43 CTF condensate formation, while WIPI2 is necessary for condensate clearance**

Our proximity analysis identified autophagy-related factors dynamically enriched during TDP-43 CTF condensate formation and clearance (Fig. 8, cluster 2). To corroborate the time-resolved recruitment of autophagy components, we propagated the interaction network using annotated physical interactions (BioGRID v. 4.4.412<sup>331,332</sup>) for the identified components (Fig. 9A in yellow). Interactors of autophagy components were ranked based on their influence within the network (eigenvalue centrality) (Figure S5A); among the top 10% of hits, we identified VCP (top-ranking hit), OPTN, UBQLN2 and TAX1BP1 which form a highly interconnected module with the identified autophagy factors (Fig. 9A, in blue). Proteins identified in this module were subsequently characterized by immunostaining in cells with TDP-43 CTF condensates (24h BTZ). Confocal microscopy confirmed strong co-localization of all identified autophagy components with TDP-43 CTF condensates (Fig. 9B). WIPI2, which is essential for LC3 lipidation, and various autophagy receptors (p62/SQSTM1, NBR1, OPTN, TAX1BP1) were strongly recruited to TDP-43 CTF condensates, consistent with their roles in cargo recruitment. VCP, a disaggregase and autophagosome maturation factor<sup>333,334</sup>, also strongly co-localized with TDP-43 CTF condensates, indicating a

possible role for VCP in the clearance of TDP-43 CTFs by the autophagic route. In contrast, the proteasome subunit PSMA1 exhibited only moderate enrichment (Fig. S5B), corroborating the observation that proteasomal engagement declines as condensates form (Fig. 8F–H).

Next, we investigated the functional roles of NBR1, p62/SQSTM1 and WIPI2 in TDP-43 CTF condensate formation and clearance using siRNA-mediated knockdown (KD). KD of NBR1 or WIPI2 did not affect the formation of TDP-43 CTF condensates following 24h proteasome inhibition, with condensate number and size being comparable to non-targeting control (NTC) cells (Fig. 9C,D). In contrast, p62/SQSTM1 KD significantly reduced TDP-43 CTF condensate numbers, although the size of the remaining condensates was unaffected (Fig. 9C,D). During washout experiments to assess condensate clearance, we observed substantial cell death under NBR1 and WIPI2 KD conditions, prompting us to develop a partial KD of NBR1 and WIPI2 (Fig. S5C), which abolished their colocalization with TDP-43 CTF condensates (Fig. S5D).

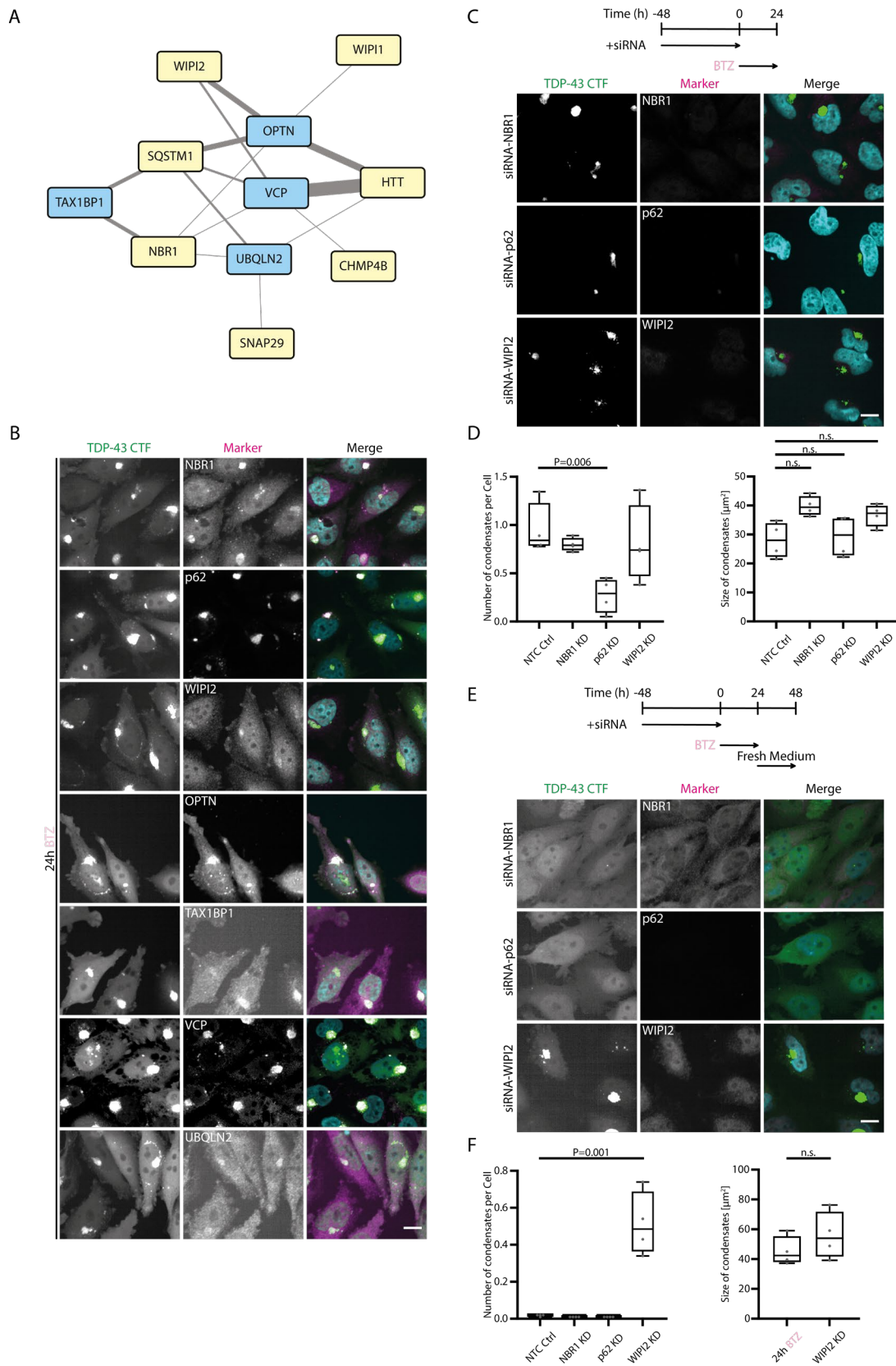


Figure 9: p62/SQSTM1 is required for TDP-43 CTF condensation, whereas WIPI2 is required for clearance of TDP-43 CTF condensates.

**A** Protein-protein interaction network based on physical interactions of autophagy factors dynamically recruited in TDP-43 CTF condensates based on BioID analysis (cluster 2; yellow nodes: WIPI1/2, SQSTM1, NBR1, HTT, CHMP4B, SNAP29). Proteins interacting with autophagy components (selected based on the highest eigenvector centrality in the network, Fig. S5A) and experimentally validated by immunostaining (**B**) are shown as blue nodes.

**B** Confocal images of EGFP-TDP-43 CTF condensates (green in the merge) stained with antibodies specific to NBR1, p62/SQSTM1, WIPI2, Optineurin (OPTN), TAX1BP1, VCP and UBQLN2 (magenta in the merge) after 24h BTZ treatment. Nuclei (DAPI) shown in cyan in the merge. Scale bar: 15  $\mu\text{m}$ .

**C** Experimental setup of siRNA-mediated knockdown (KD) of NBR1, SQSTM1/p62 and WIPI2 and TDP-43 CTF condensate formation. Confocal images show EGFP-TDP-43 CTF (green in the merge) and signals for the indicated proteins (magenta in the merge). Nuclei (DAPI) shown in cyan in the merge. Scale bar: 15  $\mu\text{m}$ .

**D** Quantification of TDP-43 CTF condensate number per cell and condensate size [in  $\mu\text{m}^2$ ] for the indicated treatments (NTC Ctrl = non-targeting control siRNA). Box plots show the median and interquartile range (IQR) with whiskers extending from minimum to maximum values across 100 cells per replicate (4 independent replicates). Statistical significance was determined by unpaired t-test comparing each KD to the NTC control.

**E** Experimental setup of siRNA-mediated KD of NBR1, SQSTM1/p62 and WIPI2, followed by 24h BTZ treatment and washout with fresh medium. Confocal images of EGFP-TDP-43 CTF (in green in the merge) co-stained for the indicated protein (magenta in the merge). Nuclei (DAPI) shown in cyan in the merge. Scale bar: 15  $\mu\text{m}$ .

**F** Quantification of remaining TDP-43 CTF condensates per cell and their size [in  $\mu\text{m}^2$ ] after 24h washout in fresh medium under the indicated siRNA KD conditions (NTC Ctrl = non-targeting control siRNA). Box plots show the median and interquartile range (IQR) with whiskers extending from minimum to maximum values across 100 cells per replicate (4 independent replicates). Statistical significance was determined by unpaired t-test comparing each KD treatment to the NTC control.

Washout experiments demonstrated that partial NBR1 KD and complete p62/SQSTM1 KD did not impair TDP-43 CTF condensate clearance, with most condensates disappearing within 24h (Fig. 9E,F).

Strikingly, partial WIPI2 KD resulted in persistent TDP-43 CTF condensates ( $0.51 \pm 0.17$  condensates/cell) that maintained their original size (Fig. 9E,F). Together, our results identify WIPI2 as a critical factor in the autophagic degradation of TDP-43 CTF condensates and reveal a role for p62/SQSTM1 in promoting TDP-43 CTF condensation.

## **5.6 p62/SQSTM1 and NBR1 show inclusion pathology in post mortem brains of FTD-TDP patients**

TDP-43 aggregates in ALS/FTD patient brains are known to highly co-localize with p62/SQSTM1<sup>335</sup>. To address whether the other autophagy receptor that strongly associates with TDP-43 CTFs during condensate clearance (Fig. 8J), NBR1, also co-localizes with pathological TDP-43 inclusions in patient brains, we performed immunohistochemistry on post-mortem frontal- and hippocampal-tissue blocks from different FTLD-TDP brains: type A (including a case carrying a *C9orf72* repeat expansion) and type C<sup>246,336</sup>. Across all cases and regions examined, p62/SQSTM1 showed almost complete co-localization with TDP-43 neuronal cytoplasmic inclusions (NCIs) (Fig. 10A,C), consistent with its established role in FTLD-TDP pathology<sup>335,337</sup>. NBR1, by contrast, labelled inclusions in a region-dependent pattern. Most prominent

staining was seen in the dentate-gyrus granule-cell layer (Fig. 10B) and less frequent in superficial frontal cortex (Fig. 10D). Taken together, our data show that the autophagy cargo-receptors p62/SQSTM1 and, to a lesser extent, NBR1 associate with pathological TDP-43 assemblies in both FTLD-TDP type A and type C human brain, supporting a role of these receptors in attempts to clear TDP-43 aggregates in the human brain via aggrephagy.

### **5.7 p62/SQSTM1 and NBR1 show inclusion pathology in post mortem brains of FTD-TDP patients**

TDP-43 aggregates in ALS/FTD patient brains are known to highly co-localize with p62/SQSTM1<sup>335</sup>. To address whether the other autophagy receptor that strongly associates with TDP-43 CTFs during condensate clearance (Fig. 8J), NBR1, also co-localizes with pathological TDP-43 inclusions in patient brains, we performed immunohistochemistry on post-mortem frontal- and hippocampal-tissue blocks from different FTLD-TDP brains: type A (including a case carrying a *C9orf72* repeat expansion) and type C<sup>246,336</sup>. Across all cases and regions examined, p62/SQSTM1 showed almost complete co-localization with TDP-43 neuronal cytoplasmic inclusions (NCIs) (Fig. 10A,C), consistent with its established role in FTLD-TDP pathology<sup>335,337</sup>. NBR1, by contrast, labelled inclusions in a region-dependent pattern. Most prominent staining was seen in the dentate-gyrus granule-cell layer (Fig. 10B) and less frequent in superficial frontal cortex (Fig. 10D). Taken together, our data show that the autophagy cargo-receptors p62/SQSTM1 and, to a lesser extent, NBR1 associate with pathological TDP-43 assemblies in both FTLD-TDP type A and type C human brain, supporting a role of these receptors in attempts to clear TDP-43 aggregates in the human brain via aggrephagy.

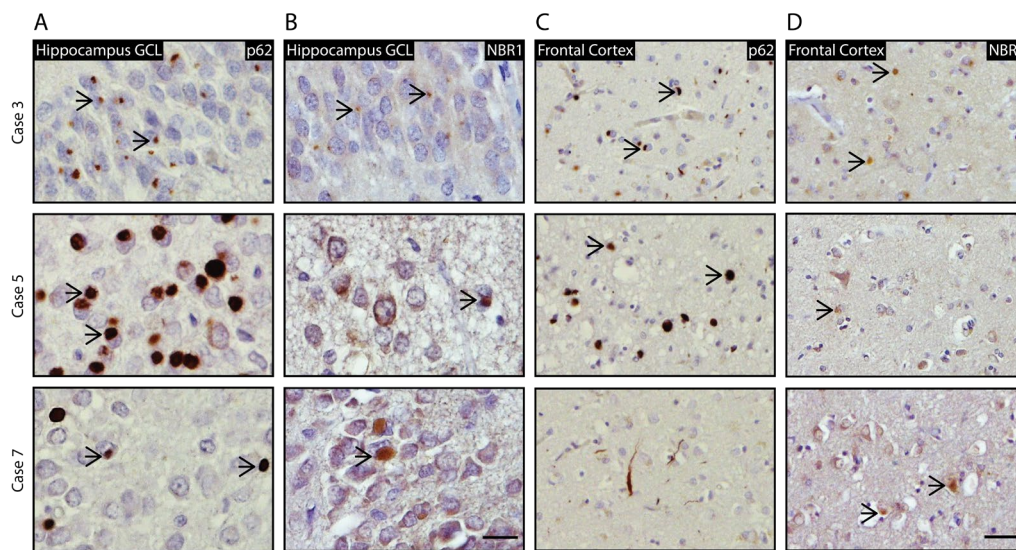


**Figure 5: Autophagy receptors p62/SQSTM1 and NBR1 form inclusions in FTLD-TDP brain tissue**

**A** Hippocampal dentate-gyrus granule-cell layer (GCL) from three different FTLD-TDP cases (case 3: FTLD-TDP type A with C9orf72 repeat expansion; case 5: sporadic FTLD-TDP type A; case 7: sporadic FTLD-TDP type C) stained for p62/SQSTM1 (arrowhead). Scale bar: 20  $\mu$ m.

**B** Serial hippocampal GCL sections of the same fields stained for NBR1 (arrowhead). Scale bar: 20  $\mu$ m.

**C** Superficial frontal cortex (layers II/III) from the same cases stained for p62/SQSTM1 (arrowhead). Scale bar: 40  $\mu$ m.

**D** Serial frontal-cortex sections of the same fields stained for NBR1 (arrowhead). Scale bar: 40  $\mu$ m.

## 5.8 Supplementary Figures

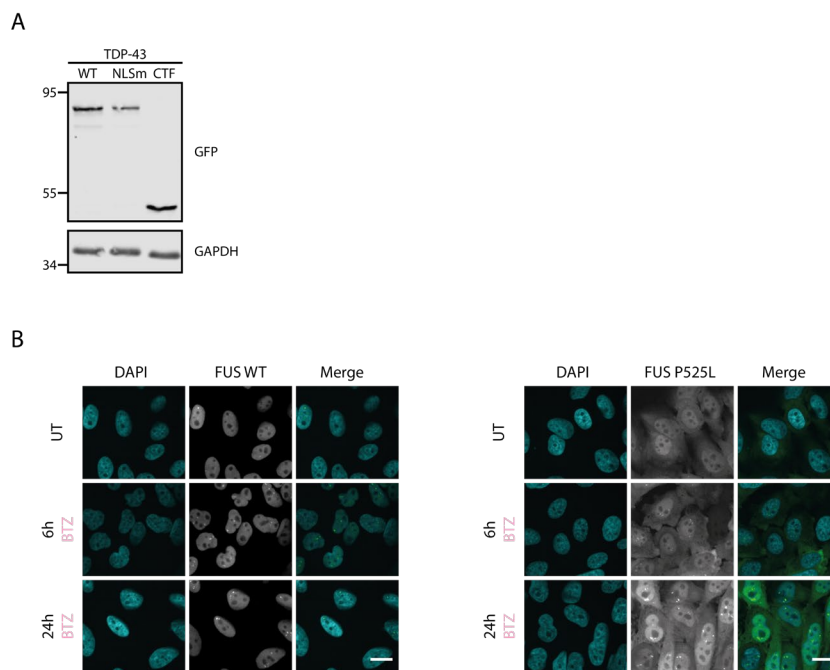


**Figure S1: Expression of EGFP-TDP-43 variants in stable inducible cell lines and confocal analysis of EGFP-FUS localization (WT or P525L) after BTZ treatment.**

**A** Western blot of EGFP-TDP-43 WT, NLSm and CTF expression and GAPDH as loading control. TDP-43 variants were detected using an anti-GFP antibody and GAPDH was detected using anti-GAPDH Antibody.

**B** Confocal microscopy of HeLa cells expressing the indicated EGFP-FUS variants (WT vs. P525L) either untreated (UT) or after 6 or 24h BTZ treatment (DAPI: nuclei in cyan; EGFP-FUS variants in green in the merge). Scale bars: 15  $\mu$ m.

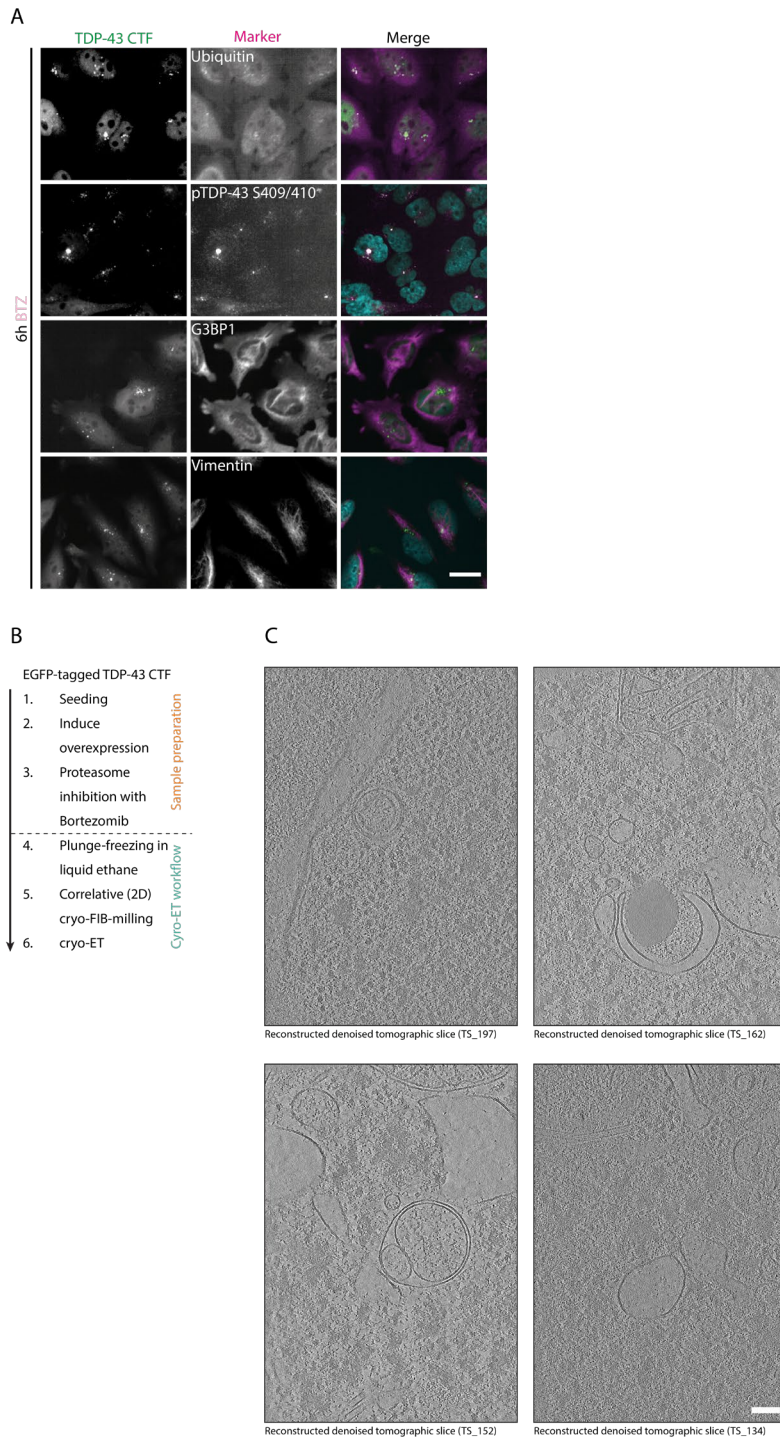


**Figure S2: pS409/S410-TDP-43 signal is already detected on TDP-43 CTF condensates after 6h BTZ treatment.**

**A** Immunostaining of EGFP-TDP-43 CTF condensates (green in the merge) with antibodies specific to Ubiquitin (FK2), phospho-S409/410-TDP-43, G3BP1 or Vimentin (magenta in the merge) after 6h BTZ treatment. Nuclei (DAPI) are shown in cyan in the merge. Scale bar: 15  $\mu$ m.

**B** Workflow of cryo-ET experiment. Numbers on the left indicate day of action.

**C** More representative cryo-ET tomographic slices from different examples of EGFP-TDP-43 CTF correlated regions. Scale bar: 100 nm.

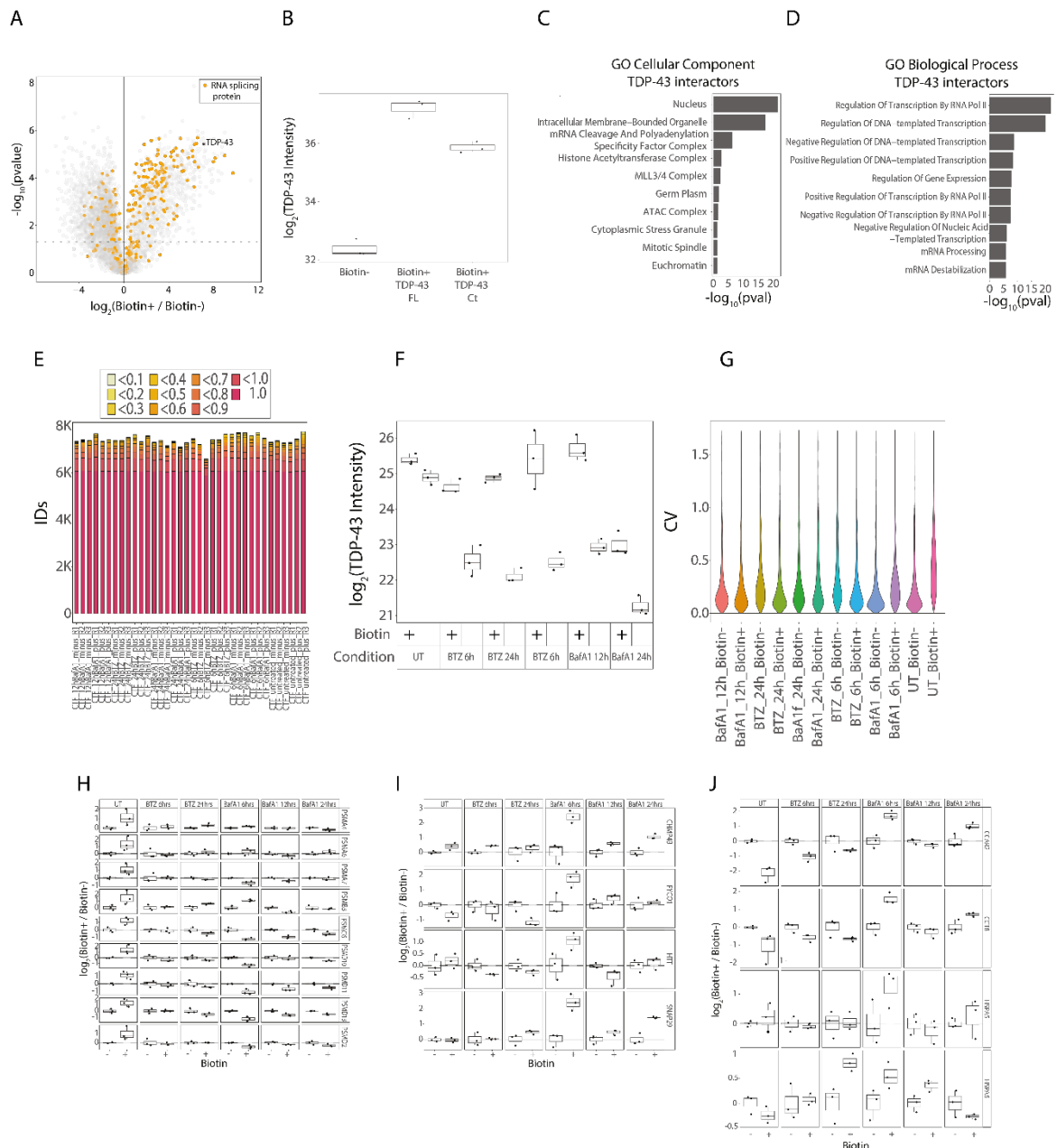


**Figure S3: BioID Quality Control and Proteostasis-Related Proximity Interactors of TDP-43 CTF**

**A** Volcano plot showing proteins differentially enriched with and without Biotin. The bait (TDP-43 WT) is labeled in grey, while RNA binding proteins (GO:0003723) are highlighted in orange.

**B** TDP-43 intensity (bait abundance recovery) from the BioID experiment (control without Biotin and Biotin TDP-43 full-length (FL) and CTF). The boundaries of the boxplot correspond to the quantiles Q1 (25%) and Q3 (75%), the average value is represented by a line across the center of the box. Lower and upper whiskers are defined by Q1-1.5IQR and Q3+1.5IQR (N=3).

**C,D** GO Cellular Component and Biological Process characterization for proteins identified with a  $\log_2FC > 2$  and  $p\text{-value} < 0.05$  in the BioID experiment for TDP-43 (referring to Fig. 4B). The significance of the Terms was calculated considering the identified proteins as background.

**E** Protein identification per single run in the BioID TDP-43 CTF dataset treated with BTZ and BafA1. The bar plot represents the completeness of the acquired matrix, with color indicating the frequency of protein identification, ranging from pale yellow (proteins identified in less than 10% of the runs) to dark red (proteins identified in all acquired runs).

**F** Intensity of the bait protein (TurboID-3xHA-TDP-43 CTF) without biotin and with biotin stimulation for all conditions (untreated (UT) and treated with BTZ and BafA1 for the indicated times), the average value is represented by a line across the center of the box. The boundaries of the box plot correspond to the quantiles Q1 (25%) and Q3 (75%). Lower and upper whiskers are defined by Q1-1.5IQR and Q3+1.5IQR (N=3).

**G** Distribution of coefficient of variations (CV) values for protein levels in the BioID TDP-43 CTF dataset.

**H, I** Profile abundance for proteins identified in cluster 5 and linked to proteasome (A) and for proteins in cluster 2 and linked to autophagosome (B). Protein abundance was normalized for the average of the minus biotin condition

(N =3). The boundaries of the box plot correspond to the quantiles Q1 (25%) and Q3 (75%) the average value is represented by a line across the center of the box. Lower and upper whiskers are defined by  $Q1 - 1.5IQR$  and  $Q3 + 1.5IQR$ .

**J** Profile abundance for proteins identified in cluster 5 and linked heat shock protein. Protein abundance was normalized for the average of the minus biotin condition (N =3). The boundaries of the box plot correspond to the quantiles Q1 (25%) and Q3 (75%) the average value is represented by a line across the center of the box. Lower and upper whiskers are defined by  $Q1 - 1.5IQR$  and  $Q3 + 1.5IQR$ .

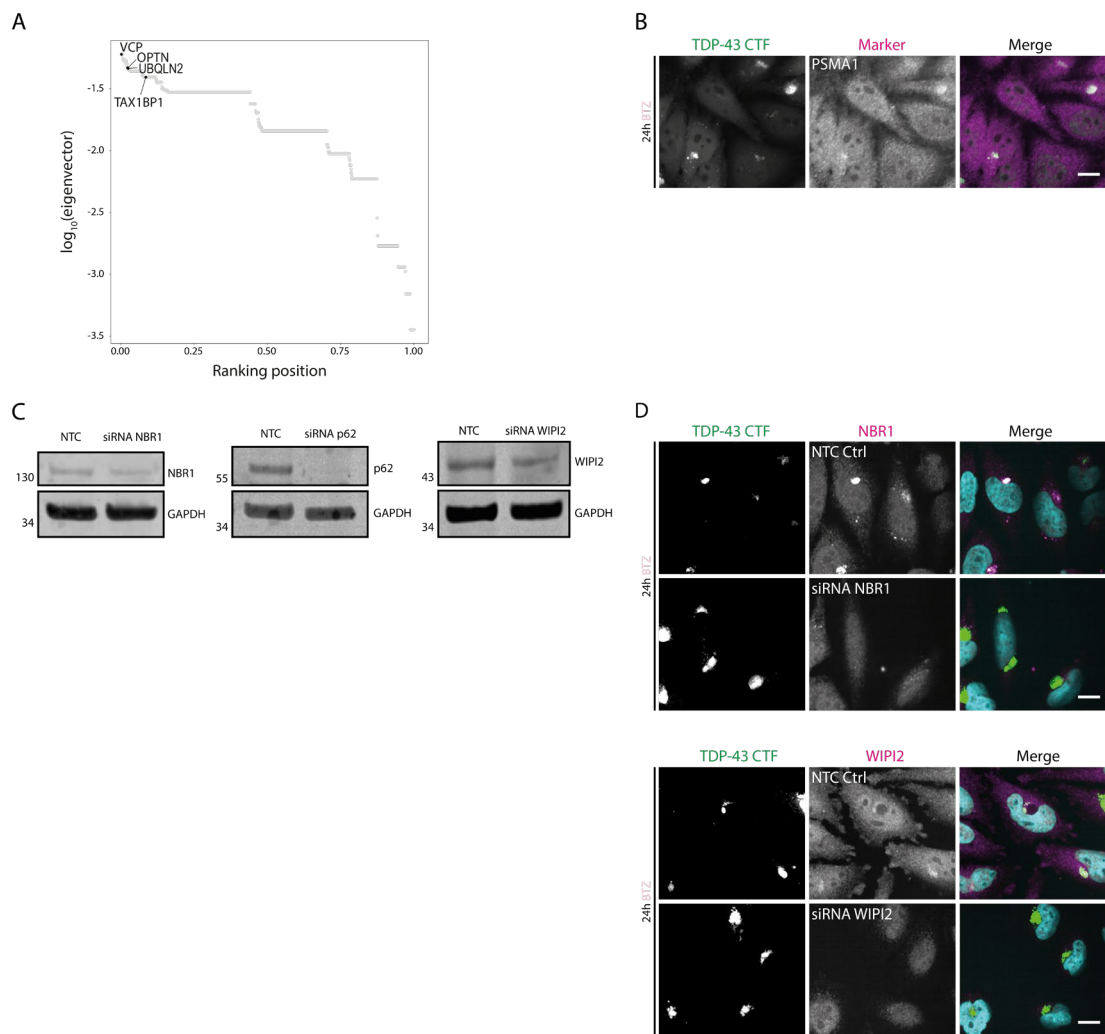


**Figure S4: Enrichment of PSMA1 with TDP-43 CTF condensates and knockdown (KD) efficiencies analyzed by Western blot and immunostaining**

**A** Rank-ordered plot of log<sub>10</sub>-transformed eigenvector-centrality scores for all genes detected in the network screen. The x-axis denotes the normalized ranking position (0 = top hit; 1 = lowest), while the y-axis shows the corresponding centrality value. Grey step line and dots represent individual genes; the four most connected modifiers are highlighted and labelled.

**B** Confocal images of 24h BZT-induced EGFP-TDP-43 CTF condensates (green in the merge) co-stained with a PSMA1-specific antibody (magenta in the merge), demonstrating enrichment of PSMA1 with aged TDP-43 CTF condensates. Scale bars: 15 µm.

**C** Levels of NBR1, p62/SQSTM1, and WIPI2 following siRNA-mediated knockdown (KD). NBR1 and WIPI2 show a partial KD, while SQSTM1 shows a very efficient KD. Protein levels were detected by Western blotting using antibodies specific to the indicated protein. GAPDH was used as loading control.

**D** Confocal images of 24h BZT-induced EGFP-TDP-43 CTF condensates (green in the merge) co-stained with antibodies specific to NBR1 or WIPI2 (magenta in the merge) after partial KD of NBR1 or WIPI2, respectively. Scale bars: 15 µm.

## 6. Results – Part B

### 6.1 Optimized Purification of UBQLN2 Variants with Minimal RNA Contamination

Phase separation and RNA-binding behavior of proteins are highly dependent on RNA content<sup>159,338,339</sup>. Therefore, minimizing RNA impurities is crucial for conducting reliable *in vitro* experiments. Using the common protocol for purifying MBP- and His-tagged proteins, e.g. TDP-43 and FUS, resulted in substantial RNA contamination, as indicated by a high 260/280 nm absorbance ratio (>0.8). To reduce RNA carryover, I introduced an additional step into the purification workflow for UBQLN2. After the initial Immobilized Metal Ion Affinity Chromatography (IMAC) purification with a HisTrap column, we incubated the bound protein with benzonase at 4 °C overnight. Benzonase is a nuclease capable of degrading single-stranded, double-stranded, linear, and circular nucleic acids. Since benzonase exhibits maximal activity at room temperature, we supplemented this with an additional 1 h incubation at room temperature the following day. The purification was then completed by size-exclusion chromatography (SEC) to separate the protein by size, and the purity of the resulting fractions was validated by SDS-PAGE analysis. Including this nuclease treatment decreased the 260/280 nm ratio to 0.68. As a ratio below 0.7 is generally indicative of a protein preparation with minimal RNA contamination<sup>340,341</sup>, this confirms that our preparation yielded highly pure protein. Using this optimized protocol, we proceeded to purify various UBQLN2 mutants (Fig. 11A). In total, I purified seven proteins with single-point mutations found in familial ALS/FTD patients, which have been described to alter phase separation properties<sup>113</sup>. In addition, we generated several domain-deletion mutants to identify domains critical for phase separation and RNA-binding behavior. Specifically, we deleted the UBL domain, which has been reported as necessary for oligomerization<sup>112,114</sup>, and the Pxx domain, which is strongly linked to disease pathogenesis<sup>17,342</sup> (Fig 11B). Beyond these domain-specific deletions, we also purified larger truncation constructs: UBQLN2 1–178 (lacking residues 179–624), UBQLN2 1–379 (lacking residues 380–624), UBQLN2 178–624 (lacking residues 1–177), and UBQLN2 379–624 (lacking residues 1–378). These variants provide a toolkit to dissect how different regions contribute to phase separation, RNA binding, and potential interactions with TDP-43 or FUS, although these aspects remain to be systematically tested.

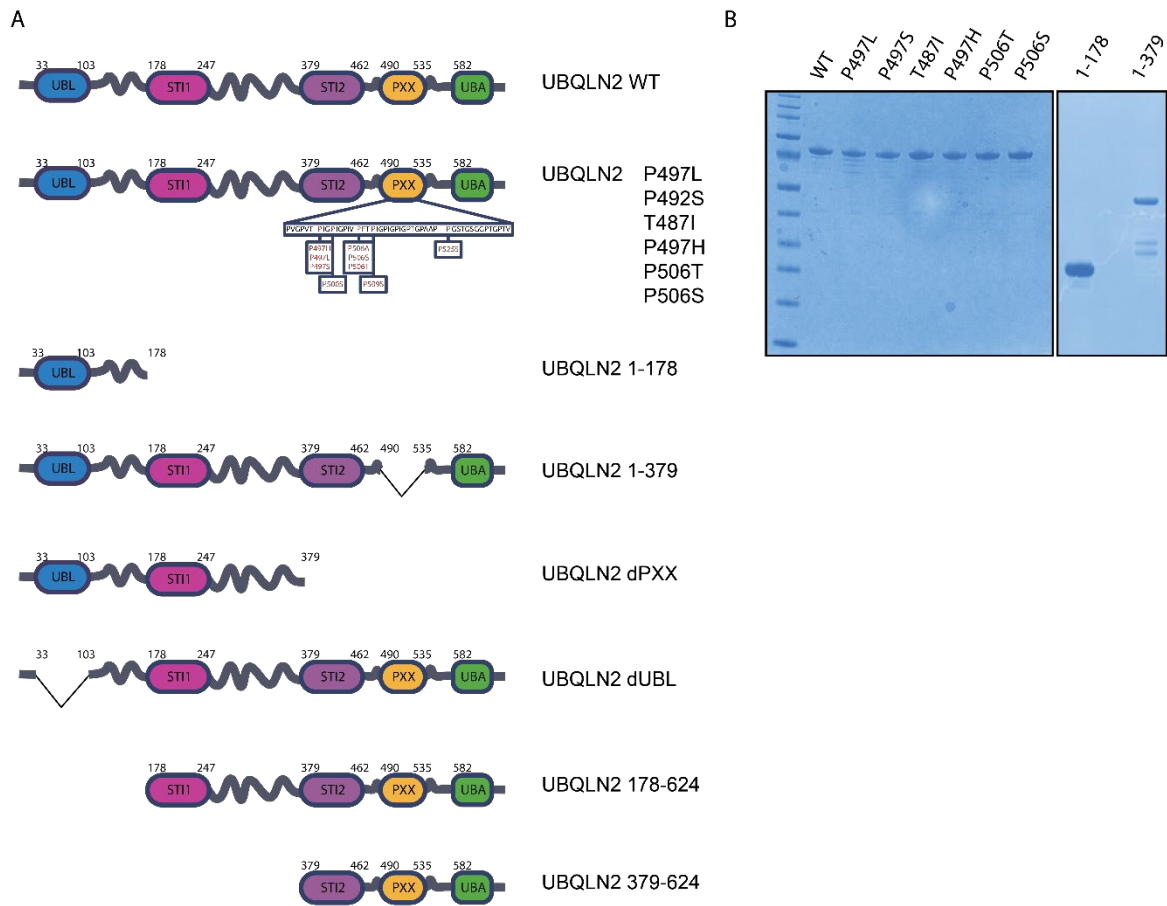


**Figure 6 Purification of nucleic acid free UBQLN2 constructs**

**A** Scheme of UBQLN2 constructs containing ALS/FTD-linked point mutations and domain-deletion mutants. Domain abbreviations: UBL (ubiquitin-like domain), ST11/ST12 (ST11-like motifs), Pxx (proline-rich repeat region linked to disease), and UBA (ubiquitin-associated domain).

**B** Purified UBQLN2 mutants on a SDS-PAGE gel stained with Coomassie Blue

## 6.2 UBQLN2 Modulates RNA Binding and Phase Separation of FUS and TDP-43

UBQLN2 may not only act as a shuttle protein for UPS and autophagy, but may also regulate RNA-binding proteins (RBPs) through different mechanisms. Previous studies demonstrated that UBQLN2 can modulate the phase separation behavior of FUS–RNA condensates<sup>23</sup>. Specifically, UBQLN2 was shown to alter the dynamics and morphology of mutant FUS–RNA condensates, as assessed by single-molecule FRET, where UBQLN2 increased the internal dynamics of FUS–RNA complexes. However, it remained unclear whether these effects were the result of a direct UBQLN2–FUS interaction or were mediated indirectly through RNA.

In addition, UBQLN2 has been reported to interact with the C-terminal region of TDP-43<sup>343</sup>, although no effect on TDP-43 phase separation or RNA binding has been described. Given that ALS/FTD patients carrying UBQLN2 mutations exhibit TDP-43

pathology, I investigated whether UBQLN2 could influence the RNA-binding and phase separation behavior of both FUS and TDP-43.

To address investigate the impact on RNA-binding, I performed electrophoretic mobility shift assays (EMSAs) using physiological RNA targets of FUS and TDP-43, respectively. As shown in (Fig. 12A), FUS formed distinct complexes with SON-GGU RNA, a well-characterized FUS target<sup>232,344</sup>. Upon titrating increasing amounts of UBQLN2 into the reaction, the FUS–RNA complex signal increased while the free RNA signal decreased, indicating that UBQLN2 enhances FUS–RNA binding. A similar effect was observed for TDP-43 (Fig. 12B), where the specific TDP-43 target RNA TDP-43 autoregulatory RNA site<sup>345</sup>, showed stronger binding in the presence of UBQLN2.

Beyond RNA-binding, UBQLN2 in the low  $\mu\text{M}$  range itself exhibited temperature- and salt-dependent phase separation behavior (Fig. 12C). Under physiological conditions (37 °C, 150 mM NaCl), UBQLN2 formed large condensates, whereas higher salt concentrations reduced droplet formation. Finally, I tested whether UBQLN2 could directly affect the phase separation of FUS. Wide-field fluorescence microscopy revealed that the presence of UBQLN2 altered FUS-EGFP condensates in an RNA-independent manner (Fig. 12D). At low UBQLN2 concentrations, FUS-EGFP phase separation appeared enhanced, whereas at higher UBQLN2 concentrations, FUS-EGFP condensate formation decreased.

Together, these results indicate that UBQLN2 not only modulates the RNA-binding capacity of FUS and TDP-43, but also alters the phase separation behavior of FUS itself. This suggests that UBQLN2 may regulate RBP dynamics at multiple levels, potentially contributing to pathological changes observed in ALS/FTD.

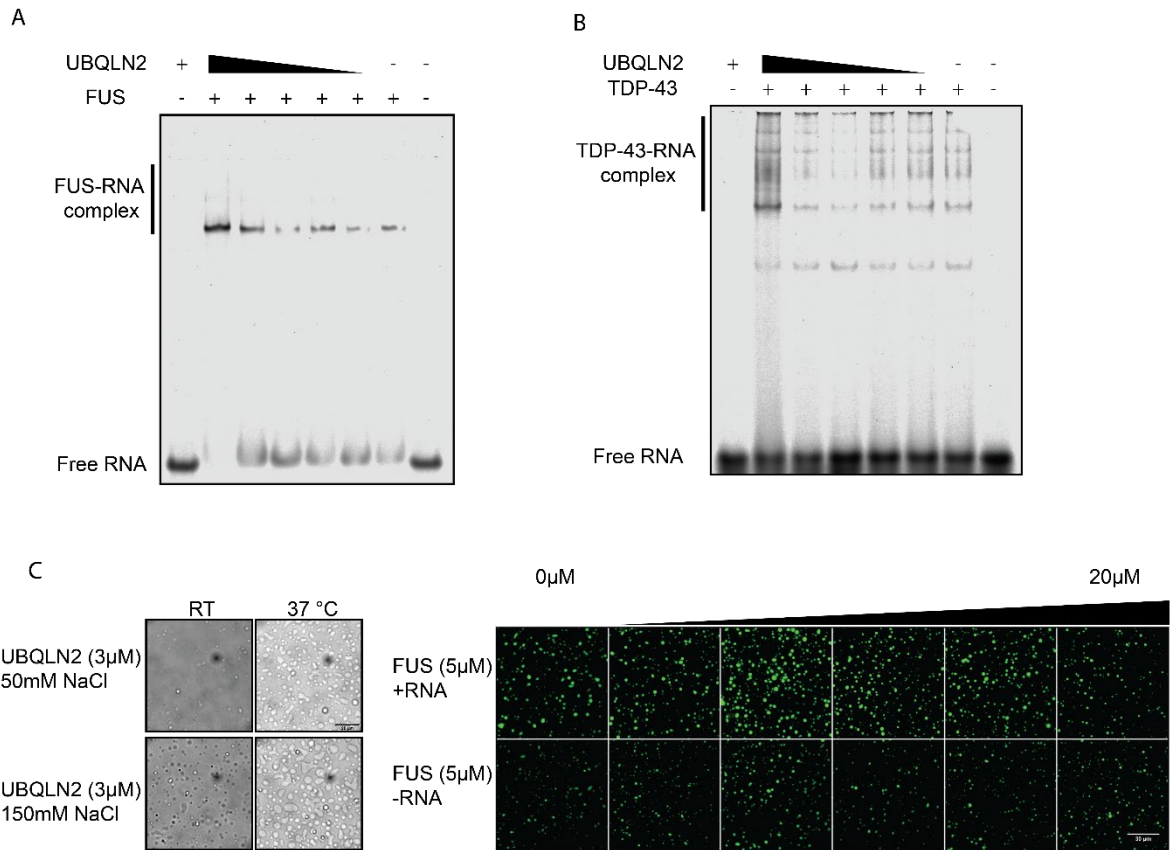


**Figure 7 UBQLN2 affects RNA binding of FUS and TDP-43 as well as phase separation behavior of FUS.**

**A** Electrophoretic mobility shift assay (EMSA) of FUS (0.3 μM) and SON-GGU RNA (2 nM) in absence or presence of UBQLN2 show enhanced FUS-RNA binding with increasing amount of UBQLN2 (0-0.6 μM)

**B** Similar effect as in (A) is seen for TDP-43 (0.2 μM) using TDP autoregulatory RNA site (8 nM) with increasing amount of UBQLN2 (0-0.4 μM)

**C** Brightfield microscopic images of UBQLN2 droplets at room temperature (RT) and 37°C at two different sodium chloride (NaCl) concentrations (50 and 150 mM) and 3 μM protein concentration. Under physiological condition, large UBQLN2 condensates are formed. Scale bar: 20 μm

**D** Wide-field fluorescence microscopy images of FUS-EGFP (5 μM) droplets with increasing amount of UBQLN2 (0-20 μM) independent on the presence (upper row) or absence (lower row) of SON-GGU RNA (1 μM) show changed phase separation behavior of FUS. In the low molar range of UBQLN2 phase separation seems increased which then decreases with high molar range. Scale bar: 30 μm

## 7. Discussion

### 7.1 Summary of findings described in Part A

In Part A, I set out to define how proteasome dysfunction reshapes the intracellular handling of TDP-43 and whether the resulting assemblies are actively triaged for clearance. Using cytosolic TDP-43 constructs, including C-terminal fragments (CTFs) I show that acute proteasome inhibition elicits a rapid and selective condensation of TDP-43 in the cytoplasm, whereas FUS, a related, disease-linked RBP, remains largely refractory under the same conditions. These TDP-43 assemblies are distinct from stress granules and aggresomes: they do not recruit G3BP1 and do not organize within a vimentin cage, indicating that the response reflects an intrinsic condensation process rather than a generic stress response or aggresome formation.

Time-resolved imaging and biochemical fractionation reveal that the TDP-43 CTF condensates are not static. In the early phase after proteasome inhibition they exhibit liquid-like behavior with high molecular exchange, but over time they “age,” becoming less mobile and partially detergent-insoluble. Simultaneously, they acquire molecular hallmarks associated with TDP-43 proteinopathy, including polyubiquitin and phosphorylation at S409/410. Correlative ultrastructural analysis (performed in collaboration with the lab of Florian Wilfling, MPI Biophysics) supports the idea that these structures are pre-amyloid, amorphous assemblies rather than mature fibrils. Together, these observations imply proteasome stress as a trigger for a liquid-to-amorphous trajectory of TDP-43 CTF assemblies, which potentially could mirror early disease-like states preceding fibrillar aggregates.

Clearance experiments following recovery from proteasome inhibition demonstrate that TDP-43 CTF condensates are removed by the autophagy–lysosome system. Pharmacological blockage of lysosomal degradation stabilizes small TDP-43-positive puncta that co-localize with LC3 and LAMP1, whereas mTOR inhibition accelerates removal, consistent with an autophagic clearance route. Importantly, chaperone activity is required for clearance: inhibition of Hsp70 function impairs clearance and biases the system toward larger, persistent assemblies. These findings support a model of “chaperone-licensed autophagy,” in which chaperones condition TDP-43 condensates for piecemeal engulfment and degradation.

Proximity proteomics experiments and functional perturbations helped to identify involved aggregation factors. Reducing p62/SQSTM1 levels decreases the number of TDP-43 CTF condensates, pointing to a role of p62 in cargo clustering, whereas depletion of WIPI2 compromises their removal, consistent with a role of WIPI2 in phagophore initiation/expansion<sup>346</sup>. In contrast, NBR1 is largely dispensable in the clearance process. Complementing these perturbations, proximity labeling across the condensation–clearance timeline reveals a proteostasis hand-off: proteasome components predominate in the diffuse state, while autophagy machinery (including p62 and WIPI-family factors) peaks during clearance. This dataset also nominates additional factors, such as VCP, OPTN and UBQLN2, which localize to TDP-43 CTF condensates and might additionally be involved in recognition, remodeling, and routing functions.

Finally, immunohistochemical analyses in FTLD-TDP brain tissue align the cell-based observations with human pathology. As previously reported, p62 robustly co-localizes with TDP-43 inclusions across different brain regions<sup>337</sup>, but we found that also NBR1 shows a region-specific aggregation, supporting its engagement in the clearance of TDP-43 in disease. Altogether, my findings reported in Part A of this thesis establish that proteasome impairment is sufficient to precipitate disease-relevant condensation of TDP-43 CTFs and that successful resolution of these assemblies depends on chaperone activity and an autophagy program with distinct receptor and co-factor contributions. These findings set the stage for future mechanistic investigations how specific modulators shape both the formation and the clearance of TDP-43 assemblies. Part B reports how one of these factors, UBQLN2, was further investigated *in vitro*.

## **7.2 Proteasome dysfunction selectively drives TDP-43 condensation distinct from stress granules or aggresomes**

My data show that acute proteasome inhibition (by BTZ) triggers a robust, time-dependent condensation of cytosolically mislocalized TDP-43, particularly its C-terminal fragment (CTF), while leaving FUS largely unaffected under the same conditions. In live-cell imaging and endpoint analyses, I found that BTZ rapidly converts diffuse TDP-43 CTF into cytosolic puncta that enlarge and lose dynamics over 24 h, whereas neither FUS WT nor FUS P525L form comparable condensates, underscoring a selective vulnerability of TDP-43 to UPS failure in this paradigm. I observed that aged TDP-43 CTF condensates become partially RIPA-insoluble and exhibit reduced FRAP

recovery, yet lack fibrillar ultrastructure by in situ cryo-ET, arguing for an amorphous, non-amyloid organization at the stage captured here. Together, these observations position UPS stress as a preferential driver of early TDP-43 condensation, rather than a generic inducer of RBP granulation.

Several lines of evidence argue that BTZ-induced TDP-43 CTF assemblies are not stress granules (SGs). First, they fail to recruit G3BP1, a core SG scaffold and hallmark marker of SGs (ref), despite efficient SG induction under these conditions. SGs are RNA–protein condensates that nucleate when translation initiation is inhibited and G3BP1-centered networks phase-separate, typically dissolving upon stress relief<sup>126,127</sup>. Under chronic or proteostasis-impaired states some SGs can “mature” into less dynamic, ubiquitin/p62-positive solids and become substrates for autophagy<sup>65,137,347</sup>. By contrast, our TDP-43 CTF assemblies appear under proteasome blockade. They do not carry SG identity by marker recruitment, and my proximity proteomic analysis shows a proteasome-to-autophagy hand-off that is depends on their biophysical properties and partial insolubility. Instead, it is likely that BTZ inhibition strongly raises the levels of TDP-43 CTF, causing its concentration-dependent condensation independent of SGs.

Aggresomes represent a distinct stress response in which HDAC6-driven transport corrals ubiquitylated misfolded proteins into a juxtannuclear, centrosome-proximal inclusion encased by a vimentin cage<sup>96</sup>. Although proteasome inhibition is a classic trigger for aggresome formation, BTZ-induced TDP-43 CTF condensates in our system did not exhibit a vimentin cage at either early (6 h) or late (24 h) time points, as revealed by co-immunostaining for vimentin. Morphologically, I observed multiple cytosolic puncta rather than a single perinuclear body, further distinguishing these assemblies from aggresomes. Hence, while UPS stress is sufficient to induce aggresomes in many contexts<sup>96</sup>, the TDP-43 CTF assemblies characterized here follow a different formation route, independent of aggresomes.

The selectivity for TDP-43 over FUS might reflect differences in (i) exposure of low-complexity domains, (ii) degradation routing, and (iii) condensation propensity. Disease-relevant TDP-43 C-terminal fragments accumulate in ALS/FTD and are strongly aggregation-prone. Their generation and persistence correlate with toxicity and impaired clearance<sup>220,348–350</sup>. In our system, UPS inhibition blocks the rapid proteasomal turnover of TDP-43 CTF and likely unmask its intrinsic condensation

propensity that proceeds from liquid-like droplets to more gel-like, amorphous aggregates. FUS, by contrast, tends to condense in response to nucleocytoplasmic transport defects or altered RNA/ATP buffering, and its phase separation is actively suppressed by Transportin-1 interactions. Import disruption or changes in RNA/ATP milieu are well-established drivers for FUS condensation<sup>5,230,237,238,351</sup>. Under the acute trigger used here (UPS failure), those FUS-specific drivers are not engaged, explaining the lack of FUS condensates despite comparable proteotoxic pressure. In short, UPS stress is a potent “TDP-43-centric” perturbation, whereas FUS generally responds to different axes of cellular dysregulation.

Our findings fit a model in which soluble TDP-43 CTF is normally rapidly degraded by the proteasome. When UPS flux is diminished, cytosolic concentration rises above its critical condensation threshold, yielding TDP-43 CTF droplets that subsequently age and then are routed towards autophagy. This is seen as a decline in proteasomal engagement and the progressive recruitment of the autophagy-lysosome machinery (e.g. WIPI2, cargo receptors, LC3 and LAMP1)), culminating in degradation by lysosomes when the proteasome constraint is relieved. The assemblies’ amorphous ultrastructure seen by cryo-ET is consistent with an early aggregate phase that remains accessible to chaperone/autophagy surveillance. Notably, these mechanistic steps unfold without SG or aggresome intermediates, emphasizing that TDP-43 can enter a distinct condensation–clearance loop under proteasome stress.

Together, our data suggest that proteasome compromise in neurons, which have special requirements for proteostasis, might preferentially seed TDP-43 pathology without affecting FUS<sup>5</sup>. They also highlight two possible therapeutic levers: preventing the initial UPS-driven TDP-43 condensation (e.g., by enhancing UPS flux) and expediting the downstream hand-off to autophagy (e.g., by enhancing WIPI2-dependent phagophore formation), all while avoiding SG or aggresome-centric interventions that do not target the assemblies observed here<sup>96,126,127,137</sup>.

### **7.3 From liquid to amorphous: early pathological intermediates in cells and human tissue**

Time-resolved analyses indicate that the assemblies formed by cytosolic TDP-43 C-terminal species after proteasome inhibition are not static endpoints but evolve along a biophysical trajectory from liquid-like droplets to more gel-like, amorphous states. Early condensates display substantial molecular exchange and rapid internal

rearrangements, whereas later structures show reduced mobility and increased detergent insolubility which are features consistent with condensate “aging” and material hardening under sustained proteotoxic load. This maturation occurs without distinct fibrillization at the stage captured here, implying that proteasome stress drives TDP-43 CTFs across a condensation threshold into pre-amyloid intermediates rather than immediately into amyloid fibers. Such intermediates are particularly important conceptually, because they are likely to be accessible to cellular surveillance and clearance mechanisms before becoming irreversible lesions. Importantly, evidence from patient material indicates that such amorphous aggregates are not restricted to early intermediates. It is reported that TDP-43 inclusions in FTD brains contained a mixture of amorphous and fibrillar material, suggesting that non-fibrillar assemblies can persist into disease stages and may contribute directly to pathology alongside amyloid-like species<sup>352</sup>.

As the condensates age, they acquire molecular signatures that track with human TDP-43 proteinopathy: polyubiquitin and phosphorylation of TDP-43 at serines 409/410. Ubiquitination is a near-constant feature of pathological TDP-43 inclusions in ALS/FTD, and phosphorylation at S409/410 is widely recognized as a disease hallmark in patient tissue<sup>5</sup>. The appearance of these modifications on maturing condensates situates them on the same pathological axis towards mature inclusions found in disease, but at an earlier, potentially reversible point in the cascade. This aligns with the idea that selective autophagy can recognize and triage aberrant condensates, particularly when they have begun to accumulate ubiquitin and LC3-interacting cargo receptors<sup>137</sup>.

Ultrastructural inspection supports an amorphous, non-fibrillar organization for the late condensates observed under proteasome stress. Rather than the ordered  $\beta$ -sheet architecture typical of amyloid, these structures present as dense, irregular assemblies. An amorphous organization is more susceptible to the continued action of chaperones and the autophagy machinery, which can fragment and package cargo for lysosomal degradation before fibrillar order sets in<sup>137</sup>. Consistent with this, recent work showed that autophagy preferentially targets non-fibrillar polyQ aggregates, reinforcing the idea that early, amorphous assemblies remain within reach of the clearance machinery<sup>353</sup>. According to this view, TDP-43 C-terminal species enter a surveillance-competent condensate state that can still be cleared if the appropriate quality-control pathways engage in time, before TDP-43 CTFs have been converted into fibrils.

The molecular convergence between aging condensates and patient inclusions is further underscored by immunohistochemical patterns in FTLD-TDP, where p62/SQSTM1 is a robust component of TDP-43-positive inclusions across brain regions and disease subtypes<sup>5</sup>. The presence of p62 in human lesions aligns with the condensates' enrichment in ubiquitin and with their eventual routing to autophagy, reinforcing a model in which cargo receptors scaffold and hand off aberrant TDP-43 assemblies to the degradative pathway<sup>5,137</sup>. The type of ubiquitin modification is likely to be critical: K48-linked chains are enriched in TDP-43 inclusions and typically signal proteasomal degradation, while K63-linked chains are also frequently observed and align with autophagic processing<sup>207,354,355</sup>. At the same time, ubiquitin costaining in patient tissue does not by itself prove that TDP-43 is directly ubiquitylated. It could instead reflect ubiquitination of associated proteins within the inclusions<sup>207,355</sup>. Definitive evidence would require biochemical analyses such as co-immunoprecipitation under denaturing conditions to determine whether ubiquitin is covalently attached to TDP-43 itself. Together, these observations support a staging framework: proteasome dysfunction elevates cytosolic TDP-43 C-terminal species, which rapidly condense into liquid-like droplets. Sustained stress promotes material aging, modification by ubiquitin and phospho-S409/410, and transition to amorphous intermediates that are primed for aggrephagy. Failure or delay in this hand-off risks progression toward more intractable, neuron-damaging pathology. This staging helps reconcile how proteasome compromise can seed disease-relevant TDP-43 biology while still leaving a therapeutic window for chaperone/autophagy-based interventions<sup>5,137,220,348–350</sup>.

#### **7.4 Chaperone and autophagy cooperation in TDP-43 clearance (p62, WIPI2, KEAP1)**

Following recovery from proteasome inhibition, the TDP-43 condensates described above are not left to passive dissolution but are actively removed by the autophagy–lysosome system. Pharmacological and marker-based evidence converge on this route: lysosomal blockade stabilizes small TDP-43–positive puncta decorated by LC3/LAMP1, whereas mTOR inhibition accelerates disappearance, consistent with enhanced autophagic flux<sup>137</sup>. While these data highlight autophagy as a major clearance mechanism, we cannot exclude that proteasomal degradation or spontaneous dissolution also contribute, and the overall process is likely a combination of these pathways. A key requirement for molecular chaperone activity emerges in

parallel. Inhibiting Hsp70 function shifts the system toward larger, persistent assemblies and delays clearance, aligning with the view that Hsp70-based machineries fragment, remodel, and “license” condensates for engagement by the autophagy apparatus<sup>99,137,356</sup>. Recent studies have shown that HSP70, together with HSP110, DNAJB6, and even the 19S proteasomal subunit, can act as a key complex regulating the fragmentation of large condensates<sup>357</sup>. Testing this concept in this TDP-43 condensation model, for example by systematically silencing or inhibiting these factors could provide valuable insight into their role in disassembly and clearance. Together, these observations support a “chaperone-licensed aggrephagy” model in which chaperones prepare aberrant TDP-43 condensates for piecemeal engulfment and lysosomal turnover.

Within this program, aggrephagy factors show a division of labor that helps explain both the formation and removal phases. p62/SQSTM1 can undergo ubiquitin-induced phase separation with ubiquitylated clients, a property that efficiently concentrates cargo above the capture threshold for autophagy<sup>358</sup>. These properties might promote TDP-43 CTF condensate formation through its PB1-mediated oligomerization and UBA-driven ubiquitin recognition, subsequently p62 might mediate LIR-mediated docking to LC3. Complementarily, WIPI2 functions at the initiation/expansion step by sensing PI3P on nascent phagophores and recruiting the ATG12–ATG5–ATG16L1 conjugation machinery, thereby activating LC3 lipidation and enabling membrane growth around cargo<sup>359,360</sup>. I observed that reducing p62 represses the number of TDP-43 CTF condensates that form (less clustering), whereas depleting WIPI2 stalls their removal (phagophore progression defect), a pattern that fits the mechanistic partitioning of receptor-driven cargo condensation and WIPI2-driven autophagosome biogenesis<sup>358–360</sup>. Together with the chaperone requirement noted above, these roles outline a sequential logic: Hsp70-dependent remodeling, p62-mediated clustering and tagging, WIPI2-enabled phagophore capture and lysosomal degradation<sup>99,137,356,358–360</sup>.

A further layer of regulation is provided by the p62–KEAP1 axis, which links proteostasis to redox signaling and helps rationalize why p62 loss perturbs condensate dynamics beyond mere cargo clustering. Interestingly, in the proximity proteomics dataset, KEAP1 emerged as part of the cluster associated with autophagosome and cytoskeletal components. p62 directly binds KEAP1 via its STGE motif. When p62 accumulates or becomes phosphorylated (e.g., at Ser349/351), it sequesters KEAP1

and thereby stabilizes the transcription factor Nrf2, boosting antioxidant capacity<sup>94,361</sup>. Conversely, KEAP1–Cul3 can ubiquitinate p62 within its UBA domain (K420), modulating p62's sequestration and autophagic activity<sup>362</sup>. In the context of proteasome stress, this bidirectional control suggests two non-exclusive routes to failure when p62 is depleted: loss of a scaffolding/phase-separation hub for ubiquitylated TDP-43 species, and loss of KEAP1 sequestration that would otherwise tune p62 stability and bolster Nrf2-dependent stress resilience<sup>94,358,361,362</sup>. Persistent KEAP1 availability under p62 deficiency could thus both destabilize p62 (via ubiquitination) and blunt antioxidant responses, creating a feed-forward environment that favors TDP-43 toxicity. Framed this way, p62 is not just a cargo adaptor. It is a node that integrates ubiquitin signaling, stress transcription, and autophagic capture to keep TDP-43 condensates on a surveillance-competent path.

Viewed across these layers, clearance of TDP-43 condensates depends on a cooperative network: chaperones condition and fragment the material, p62 concentrates and labels it in a ubiquitin/LIR-dependent manner (and coordinates with KEAP1/Nrf2 to stabilize cellular defenses) and WIPI2 recruits the core conjugation machinery to build the autophagosome around the cargo. Failures at any step, such as reduced Hsp70 capacity, p62 dysfunction, or impaired WIPI2 recruitment, are predicted to slow clearance and extend the lifetime of pre-amyloid TDP-43 intermediates, increasing the probability that they progress toward more intractable pathology. This mechanistic segmentation also suggests therapeutic levers: enhancing Hsp70-based remodeling to lower the size/rigidity of condensates, boosting p62's cargo-condensing and KEAP1-sequestering functions (while avoiding chronic Nrf2 hyperactivation) and promoting WIPI2-ATG16L1 activity to expedite phagophore formation and LC3 lipidation<sup>94,99,137,356,358–362</sup>.

## **7.5 A proteostasis pathway switch: autophagy receptors and co-factor modules**

The temporal proximity-mapping, together with functional perturbations, supports a model in which TDP-43 C-terminal species are first surveilled by the proteasome while diffuse, then (once condensed and partially aged) are handed off to the autophagy–lysosome system. In the pre-condensation or early condensation window, proteasome subunits and associated quality-control factors are prominently captured, consistent with basal UPS surveillance of soluble or weakly self-associating species. As

proteasome inhibition persists and condensates mature, the interactome shifts toward autophagy machinery, and upon relief of the proteasome block the recruitment of autophagy factors peaks, coinciding with clearance. Thus, the degradation route taken by TDP-43 is not a single pathway but involves a state-dependent switch: proteasome engagement predominates for diffuse protein, whereas autophagy assumes control for aged condensates, likely involving disaggregation by chaperones and finally membrane encapsulation and lysosomal turnover.

Within this switch, autophagy receptors and membrane organizers display a division of labor that explains the phenotypes observed. p62/SQSTM1 acts as a ubiquitin-sensing scaffold capable of oligomerization and ubiquitin-induced phase separation, thereby concentrating ubiquitylated TDP-43 species above the threshold for capture and linking them to LC3 via its LIR motif<sup>358</sup>. This clustering function rationalizes why reducing p62 levels by siRNA-mediated knockdown lowers the number of TDP-43 CTF condensates that form under proteasome stress: without p62's multivalent hub function, ubiquitylated TDP-43 CTF appears to remain below the critical concentration needed for coalescence and subsequent hand-off to the LC3-positive phagophore membrane.

In addition to p62, other aggrephagy receptors contribute to cargo clustering and capture. NBR1, for example, shares many functional features with p62, including a ubiquitin-binding domain and LC3-interacting region, and is often recruited to the same inclusions<sup>50</sup>. Genetic studies suggest that p62 and NBR1 can act cooperatively, forming mixed oligomers that increase avidity for ubiquitin-tagged substrates<sup>87</sup>. At the same time, there is evidence for partial redundancy: loss of p62 alone does not completely abolish aggregate clearance, whereas combined loss of p62 and NBR1 produces stronger phenotypes<sup>363</sup>. Other receptors such as OPTN, TAX1BP1, and NDP52 also contribute in more selective contexts, particularly when aggregates are associated with damaged organelles or stress granules<sup>87</sup>. Thus, while p62 provides a dominant hub function in clustering ubiquitylated TDP-43, additional receptors likely ensure robustness of aggrephagy by sharing or reinforcing this role.

By contrast, WIPI2 operates at the level of phagophore initiation and expansion. Through binding PI3P and recruiting the ATG12–ATG5–ATG16L1 conjugation machinery, WIPI2 promotes LC3 lipidation and membrane growth around selected cargo, so its depletion primarily stalls autophagosome formation, not initial cargo

clustering<sup>359</sup>. Together, these molecular roles map cleanly onto the observed sequence, p62-driven condensation and tagging, followed by WIPI2-dependent enclosure.

Beyond autophagy receptors and PI3P readers, other factor likely tunes both the pre-clearance remodeling of condensates and their post-capture processing. VCP/p97, with its disaggregase activity and links to both UPS and autophagy, is well placed to extract and unfold proteins at the condensate–membrane interface. Small heat-shock proteins (sHSPs) may also contribute at this stage. These ATP-independent chaperones act as holdases that prevent irreversible solidification and keep client proteins in a refoldable or degradable state<sup>364</sup>. Recent work has shown that sHSPs such as HSPB8 cooperate with BAG3 to promote aggrephagy<sup>365,366</sup>, and HSPB1/HSPB5 can influence the dynamics of RNA-binding protein condensates<sup>223</sup>. It is therefore plausible that sHSPs act upstream of Hsp70 systems, stabilizing fluid-like states and priming condensates for subsequent remodeling and clearance. Small heat-shock proteins and Hsp70 systems together can help to fluidize or fragment condensate material to make it compatible with autophagic engulfment. The proximity proteomics signatures and co-localization patterns that I identified are consistent with such a remodel-then-route logic: chaperones and AAA+ ATPases may condition the material, receptors and WIPI proteins provide the capture geometry, and lysosomes complete the turnover. Finally, cargo adaptors beyond p62 can participate in cell-type- or context-specific fashion. In our system, NBR1 contributes little to formation or clearance of TDP-43 CTF condensates, and the role of other receptors, e.g. OPTN or TAX1BP1, remain to be functionally addressed, e.g. by knockdown studies. It is possible that they are functionally redundant with p62, or they may become more relevant under certain stress conditions, or in neurons, or when ubiquitin-linkage patterns differ<sup>356</sup>. Notably, a factor that emerged in our dataset, UBQLN2, is at the interface of the UPS and autophagy pathways<sup>117,342,367</sup>. Given its UBL/UBA architecture and genetic links to ALS/FTD, it is another strong candidate to modulate TDP-43 CTF condensation and/or clearance and has been further studied *in vitro*, as described in Part B of the results section.

In sum, my data support a state-dependent proteostasis switch governed by modular components: p62 concentrates and tags TDP-43 CTF condensates, WIPI2 is involved in building the capture machinery, and a set of chaperones and ATPases (including VCP) may remodel the cargo for efficient lysosomal delivery. This coordinated hand-

off explains how cells can pivot from proteasome surveillance to autophagy when aberrant assemblies emerge. It offers mechanistic levers for therapeutic strategies, like enhancing p62's cargo scaffolding, strengthening WIPI2-ATG16L1 recruitment, or boosting VCP/chaperone remodeling, as possible means to accelerate the disposal of early TDP-43 aggregation intermediates without globally overactivating proteolysis<sup>137,356,358,359</sup>.

## **7.7 Broader implications and translational relevance**

The state-dependent hand-off (from proteasomal surveillance of diffuse TDP-43 C-terminal species to autophagic capture of aged TDP-43 condensates) that I describe here should be discussed in the context of neuron-selective vulnerability in ALS/FTD. Neurons operate with long processes, high metabolic demand, and limited capacity to dilute damaged proteins by division. Under these constraints, even transient dips in UPS flux may raise cytosolic TDP-43 CTF levels above a condensation threshold, initiating the liquid-to-amorphous trajectory that I have observed in my research. Once formed, such intermediates accumulate ubiquitin and phospho-S409/410, recruit cargo receptors, and must be cleared efficiently to avoid progression towards more intractable pathology. This suggests proteasome compromise not as a late accompaniment of degeneration but as a plausible entry point to TDP-43 proteinopathy, with autophagy and chaperones determining whether cells recover or cross a point-of-no-return<sup>137,356</sup>. Indeed, several independent studies support this interpretation: reduced proteasome activity and accumulation of ubiquitin conjugates have been observed in ALS/FTD patient tissue<sup>368</sup>. Proteasome inhibition in cellular models triggers cytoplasmic mislocalization and aggregation of TDP-43<sup>286</sup>, and proteasome impairment in vivo accelerates TDP-43 pathology and neurodegeneration<sup>369</sup>

Therapeutically, these findings suggest two separable levers. First, prevent formation of TDP-43 condensates/aggregates by preserving proteasome throughput and stabilizing the RNA-bound, soluble pool of TDP-43. This encompasses classic UPS-supportive strategies, such as enhancing proteasome activity through small-molecule proteasome activators or preventing excessive proteasome inhibition by reducing oxidative or ER stress and extends to factors that regulate TDP-43's phase behavior<sup>370</sup>. Second, accelerate clearance once aberrant TDP-43 condensates arise, by strengthening the chaperone–aggrephagy axis. Here, small-molecule or genetic

augmentation of Hsp70/Hsp110-based disaggregation and remodeling could keep condensates in a fragmentable, engulfment-competent state, reducing their residence time and limiting secondary seeding<sup>99,356</sup>. On the other hand, several reports indicate that certain chaperones can support and even accelerate Tau fibril seeding<sup>371,372</sup>. This suggests that chaperones do not act unilaterally but rather in a condition-dependent manner, highlighting the fine balance that governs their function. On the autophagy side, selectively enhancing WIPI2-ATG16L1 recruitment and LC3 lipidation should expedite phagophore growth around tagged cargo, whereas broadly activating autophagy without improving capture risks diverting capacity away from relevant substrates<sup>359</sup>. These approaches are conceptually orthogonal: chaperones tune material properties, WIPI2 and the conjugation machinery tune membrane geometry and flux. Combining them may yield additive benefits by targeting both the biophysical properties of condensates and the efficiency of their delivery to lysosomes.

The p62/SQSTM1–KEAP1 axis could potentially also be harnessed in therapeutic strategies. Because p62 both clusters ubiquitylated cargo and sequesters KEAP1 to stabilize NRF2-dependent antioxidant programs, interventions that boost p62 function can, in principle, reinforce two protective layers: cargo condensation for capture and stress resilience via NRF2<sup>94,102</sup>. But chronic, unrestrained NRF2 activation carries liabilities, including metabolic rewiring and potential interference with normal redox signaling<sup>373</sup>. Any p62-targeting strategy therefore should aim for timed, context-dependent engagement rather than tonic activation, and should be paralleled with enhanced autophagy capture to prevent building condensates that outstrip clearance. In parallel, AAA+ remodeling factors such as VCP/p97 represent attractive targeting nodes because they bridge UPS and autophagy and can assist at the condensate–membrane interface. Yet given VCP’s broad cellular roles, dosing and selectivity will be critical to avoid off-target proteostasis disruption<sup>356</sup>.

My mechanistic insights also could be relevant for biomarker considerations. If TDP-43 pathology initiates through pre-amyloid, amorphous intermediates decorated with ubiquitin and p62, then assays that read out mixed K48/K63 ubiquitin codes, p62 engagement, and phospho-S409/410 levels could serve as early indicators and as pharmacodynamic markers for agents that improve chaperone conditioning or autophagic capture<sup>5</sup>. In cell culture model systems, quantitative live-cell readouts like condensate number/size distributions, FRAP-derived material properties, and

clearance kinetics upon washout can function as mechanism-proximal endpoints to rank candidate interventions before advancing to neuron/iPSC models where transport geometry and long-lived proteostasis constraints are more faithfully represented<sup>356</sup>.

### **7.8 Summary of findings described in Part B**

As described in in Part B, I explored whether UBQLN2, an ALS/FTD–linked proteostasis factor modulates RNA-binding and phase separation of disease-relevant RBPs. I first established a purification workflow that removes unwanted RNA from recombinant UBQLN2, ensuring that subsequent in-vitro measurements are free from contaminating RNAs. Using electrophoretic mobility shift assays with defined RNA substrates, I found that UBQLN2 enhances the RNA-binding of both FUS and TDP-43, shifting the equilibrium toward higher-affinity RBP–RNA complexes. Functionally, this places UBQLN2 at the interface of proteostasis routing and RNA-binding homeostasis: by favoring the RNA-bound state of FUS and TDP-43, UBQLN2 is predicted to raise the concentration threshold for aberrant phase separation of these RBPs, thereby reducing the likelihood that proteotoxic stress pushes them into maladaptive condensates.

These findings align with the modular architecture of UBQLN2: an N-terminal ubiquitin-like (UBL) domain that can engage the proteasome, a C-terminal ubiquitin-associated (UBA) domain that recognizes ubiquitin chains, and internal regions that support multivalent client interactions<sup>374</sup>. In cells, such a topology is well suited to couple client selection with downstream routing, and the in-vitro data here add an orthogonal dimension, tuning of RNA occupancy that could influence whether RBPs remain in a soluble, chaperone-surveyed pool or cross a condensation barrier under stress. Together with my results described in Part A, where UBQLN2 emerges within the autophagy/clearance module for TDP-43 CTF condensates, these results suggest a dual role of UBQLN2: UBQLN2 may both prevent inappropriate condensate formation (by stabilizing the RNA-bound form of RBPs) and may facilitate their disposal once condensates arise (via ubiquitin-dependent routing). Given that UBQLN2 mutations cause dominantly inherited ALS/FTD<sup>17</sup>, perturbations of either function offer plausible mechanisms by which UBQLN2 dysfunction could bias cells toward RBP pathology.

## 7.9 Mechanistic interpretation and disease context

The observations reported in Part B suggest that UBQLN2 acts on two mechanistic axes that together determine whether disease-relevant RBPs tip into maladaptive condensation or remain in a surveillance-competent pool. On the formation axis, UBQLN2 increases the RNA-bound fraction of both TDP-43 and FUS *in vitro*, which is predicted to raise the concentration threshold required for phase separation<sup>159</sup>. Because RNA binding generally competes with protein–protein self-association in these RBPs, stabilizing RBP–RNA complexes should shift the phase boundary toward solubility, delay liquid-like droplet nucleation during proteasome stress, and bias any droplets that do form toward more fluid, chaperone-amenable material states.

On the clearance axis, On the clearance side, UBQLN2 is thought to help route ubiquitylated proteins toward degradation, either by the proteasome or through autophagy<sup>374</sup>. While this role has been described in other contexts, I did not investigate it here, so its relevance to TDP-43 condensates remains speculative. In this integrated view, UBQLN2 can both prevent the initial crossing of the condensation threshold (by stabilizing RNA occupancy) and facilitate disposal when crossing nonetheless occurs (by engaging ubiquitin-dependent quality control).

This dual influence offers a coherent explanation for how UBQLN2 mutations cause ALS/FTD. Pathogenic substitutions in the UBQLN2 proline-rich (PXX) region and elsewhere may possibly weaken either side of the control loop, i.e. they may reduce UBQLN2's capacity to stabilize RBP–RNA complexes (lowering the formation threshold) and/or may compromise ubiquitin-guided routing (slowing clearance). This, however, remains to be investigated. In neurons, which operate with limited proteostasis margins, even modest defects along either axis could be amplified by long lifetimes and extended transport geometries, converting otherwise reversible condensates into persistent, ubiquitin- and p62-decorated intermediates that accumulate hallmark modifications (such as phospho-S409/410 on TDP-43) and progress toward pathology<sup>5</sup>. This model also rationalizes why UBQLN2 pathology frequently coexists with TDP-43 lesions in patient tissue: the same routing failure that produces ubiquitin-positive inclusions would be expected to promote TDP-43 retention and modification in the same compartments<sup>5,17</sup>. Although UBQLN2 can influence both FUS and TDP-43 condensation and RNA-binding *in vitro*, one possible reason UBQLN2 mutations are more often linked to TDP-43 pathology is that TDP-43

inclusions are typically heavily ubiquitin- and p62-decorated, making them especially dependent on UBQLN2's role as a ubiquitin shuttle<sup>19,316</sup>. By contrast, FUS inclusions can be ubiquitin/p62-positive but show more heterogeneous features (e.g., some intranuclear lesions with weaker p62 labeling)<sup>375</sup>, making their dependence on ubiquitin-centric routing less uniform. In that light, partial loss or misregulation of UBQLN2 could disproportionately impair clearance of ubiquitin-rich TDP-43 assemblies and thereby bias toward TDP-43 retention and modification. Consistent with this idea (but not proving causality), UBQLN2 binds ubiquitin and proteasome components<sup>114</sup> and has been shown to exacerbate TDP-43 pathology in models<sup>23</sup>. These points collectively suggest a tighter disease-relevant coupling of UBQLN2 to TDP-43 than to FUS, but this should be treated as hypothesis-level until tested directly.

Several testable predictions follow. If UBQLN2 stabilizes the RNA-bound state, then overexpressing wild-type UBQLN2 should decrease TDP-43/FUS condensate number and increase FRAP recovery under proteasome stress, whereas disease-linked UBQLN2 mutants should blunt these effects and prolong TDP-43/FUS condensate lifetimes. If UBQLN2 enhances routing, its depletion should increase ubiquitinated cargo and slow autophagic capture after proteasome recovery. Indeed, studies have shown that loss of UBQLN2 leads to an accumulation of ubiquitin-positive aggregates, impaired proteasomal degradation, and increased p62-positive inclusions, consistent with a failure to efficiently hand off ubiquitylated cargo<sup>113,114,376</sup>. Conversely, restoring UBQLN2 should normalize the proteasome to autophagy hand-off described in Part A. Finally, because these axes are mechanistically separable, one would expect epistasis with chaperone and aggrephagy components: UBQLN2's protective effects should be strongest when Hsp70 capacity is intact, since only under these conditions can ubiquitylated cargo be efficiently recognized and cleared<sup>377</sup>. However, because UBQLN2 can also modulate condensate formation directly, targeting UBQLN2 may still alter the dynamics or solubility of TDP-43/FUS condensates even when chaperone function or autophagosome biogenesis is partially compromised<sup>113</sup>. Together, these considerations place UBQLN2 at a pivotal crossroads in RBP proteostasis, by tuning RBP phase behavior and routing ubiquitylated RBP cargo towards degradation. This provides a concrete framework for how UBQLN2 dysfunction biases cells toward TDP-43/FUS proteinopathy.

## 7.10 UBQLN2 at the RNA/phase-separation interface

Alexander *et al.* (2018) demonstrated that UBQLN2 localizes to stress granules, interacts with FUS, and increases the internal dynamics of FUS–RNA complexes, thereby limiting droplet maturation and stress granule growth<sup>23</sup>. My findings from Part B converge with this theme, although derived from different experimental approaches. In particular, I observed that UBQLN2 modulates the biophysics of RNA-binding proteins at two levels: it alters condensate behavior in a concentration-dependent manner and enhances RNA binding in EMSAs with physiological RNA substrates. Together, these observations strengthen the view that UBQLN2 can tune the state of RBPs, balancing their RNA-bound solubility with their propensity to phase-separate.

There are, however, important differences between our datasets. Alexander *et al.* primarily used polyU RNA and a disease-linked FUS mutant (R244C) to show that UBQLN2 disperses condensates and increases dynamics. In contrast, I employed physiological RNA substrates and wild-type proteins, where UBQLN2 enhanced the formation of stable RBP–RNA complexes. A plausible reconciliation is that UBQLN2 loosens overly static, non-physiological FUS–polyU assemblies (appearing as dispersion) while stabilizing productive interactions with native RNAs. These divergent outcomes may therefore reflect differences in RNA identity and assay readouts, with smFRET capturing increased molecular exchange and EMSA reporting enhanced complex formation.

Another distinction lies in the concentration dependence. In my reconstitution assays, low UBQLN2 concentrations promoted FUS condensate formation, whereas higher concentrations suppressed it. This biphasic behavior provides a mechanistic rationale for why UBQLN2 overexpression in cells, globally reduces stress granule abundance<sup>23</sup>: cellular UBQLN2 levels may push the system into the high-concentration regime, where suppression dominates.

Finally, Alexander *et al.* mapped stress granule targeting to UBQLN2's Sti1-like linker and noted that UBQLN2 itself undergoes phase separation<sup>23</sup>. My results add to this by showing that UBQLN2 directly impacts the solubility and RNA-binding properties of both FUS and TDP-43, suggesting that UBQLN2 is not merely recruited to condensates but actively remodels them. Taken together, these findings support a model in which UBQLN2 acts as a tunable regulator of RBP condensates: at appropriate stoichiometries, it can stabilize RNA-bound states and enhance solubility,

while at higher levels it can dampen condensate growth and prevent pathological maturation.



## **8. Scientific Acknowledgment**

I would like to thank Edward Lemke and the entire Lemke lab? for generously sharing lab infrastructure and reagents. I am grateful to all members of the Dormann Lab for insightful discussions and comments throughout the course of this work. I thank the Proteomics Core Facility (IMB, Mainz) for their support and wish to acknowledge Dr. Federico Uliana, who co-analyzed the proteomics data, and Jiaxuan Chen for his assistance with mass spectrometry experiments. I also thank the IMB Microscopy and Flow Cytometry Core Facilities for access to their instruments. The cryo-ET samples were prepared and acquired by Delong Li, whose contribution was essential for this part of the study.

Funding from the German Research Foundation (P# 524805621) supported the Orbitrap Astral mass spectrometer. Additional support by the Deutsche Forschungsgemeinschaft (DFG) (P#316215830, P#497669232, P#511658729, P#210144599) enabled access to the Opera Phenix, Stellaris 8 Falcon Confocal, Invitrogen Bigfoot, and BD FACS Aria III SORP. This work was further supported by the DFG within SFB1177, project number 259130777 and the DFG's Heisenberg Programme (P# 442698351) (to Dorothee Dormann).

## **9. Contributions**

Yongwon Suk designed, carried out and analyzed most of the experiments shown in this Thesis, created most figures and wrote and edited the manuscript/thesis under the supervision of Prof. Dr. Dorothee Dormann.

Dr. Federico Uliana co-analyzed the proteomics data and co-created the Figure showing the proximity proteomics data (Fig. 8, S3, S4A)

Delong Li and Dr. Florian Wilfling performed, acquired and analyzed the Cryo-ET samples and co-wrote the Results Section for the Cryo-ET part (Fig. 6F-J, S2B-C)

Prof. Dr. Tammaryn Lashley performed, acquired and analyzed the IHC samples. (Fig. 10).

## 10. Acknowledgment

First, I would like to thank Doro for giving me the opportunity to work in your team and on this project. Your style of supervision, providing guidance while giving me the freedom to explore my own ideas. This increased both motivation and excitement, and allowed me to grow into an independent researcher confident in every aspect of my work.

I am also grateful to Helle, Edward, and Petra for your supervision during my TAC meetings over the years. Your outside-the-box thinking and the combination of your diverse expertise enriched my project tremendously and added value not only to the research itself but also to my personal development as a young scientist.

A heartfelt thank you goes to all past and present members of the Dormann lab. Our constant discussions in group meetings, Long Progress Reports, Journal Clubs, and 1:1 exchanges contributed enormously to my scientific growth. Beyond science, I truly appreciated all the fun and personal conversations that made my time here both enjoyable and memorable.

I owe special thanks to Maestro, whose input elevated my project and manuscript in many ways, and who always offered valuable advice as a scientific senior. Together with Simon, you also created many memorable and joyful laughs during our lunch breaks and office conversations.

I would also like to thank Edward and the Lemke lab for so kindly hosting and welcoming us from the very beginning, which made our move from Munich smooth and efficient.

Finally, I would like to thank Delong and Florian from Frankfurt for investing so much of their time and effort to strengthen my project.

Darüber hinaus möchte ich mich bei meinen Eltern und meinem Bruder für ihre jahrelange Unterstützung bedanken. Die Gewissheit, jederzeit auf sie zurückgreifen zu können, war mir stets eine große emotionale Hilfe. Ebenso möchte ich meinem besten Freund Volkan danken, der mich seit jeher in allen Aspekten meines Lebens unterstützt hat.

Zuletzt gilt mein tiefster Dank meiner Partnerin Hannah. Danke für deine Geduld und deine unerschütterliche Unterstützung in all den langen Jahren. Ich weiß, es schien manchmal so, als würde dieses Kapitel nie enden aber nun ist es geschafft, und wir können uns auf neue gemeinsame Wege konzentrieren. Ich freue mich sehr auf unser nächstes Kapitel.

## 11. References

1. Brown, R. H. & Al-Chalabi, A. Amyotrophic Lateral Sclerosis. *N Engl J Med* **377**, 162–172 (2017).
2. Bang, J., Spina, S. & Miller, B. L. Frontotemporal dementia. *The Lancet* **386**, 1672–1682 (2015).
3. Rascovsky, K. *et al.* Sensitivity of revised diagnostic criteria for the behavioural variant of frontotemporal dementia. *Brain* **134**, 2456–2477 (2011).
4. Taylor, J. P., Brown, R. H. & Cleveland, D. W. Decoding ALS: from genes to mechanism. *Nature* **539**, 197–206 (2016).
5. Mackenzie, I. R. A., Rademakers, R. & Neumann, M. TDP-43 and FUS in amyotrophic lateral sclerosis and frontotemporal dementia. *The Lancet Neurology* **9**, 995–1007 (2010).
6. Marin, B. *et al.* Variation in worldwide incidence of amyotrophic lateral sclerosis: a meta-analysis. *Int J Epidemiol* **46**, 57–74 (2017).
7. Levison, L. S., Blicher, J. U. & Andersen, H. Incidence and mortality of ALS: a 42-year population-based nationwide study. *J Neurol* **272**, 44 (2024).
8. Talbott, E. O., Malek, A. M. & Lacomis, D. The epidemiology of amyotrophic lateral sclerosis. *Handb Clin Neurol* **138**, 225–238 (2016).
9. Onyike, C. U. & Diehl-Schmid, J. The epidemiology of frontotemporal dementia. *Int Rev Psychiatry* **25**, 130–137 (2013).
10. Barberio, J., Lally, C., Kupelian, V., Hardiman, O. & Flanders, W. D. Estimated Familial Amyotrophic Lateral Sclerosis Proportion: A Literature Review and Meta-analysis. *Neurol Genet* **9**, e200109 (2023).

11. Ling, S.-C., Polymenidou, M. & Cleveland, D. W. Converging mechanisms in ALS and FTD: Disrupted RNA and protein homeostasis. *Neuron* **79**, 416–38 (2013).
12. Rummens, J. & Da Cruz, S. RNA-binding proteins in ALS and FTD: from pathogenic mechanisms to therapeutic insights. *Mol Neurodegeneration* **20**, 64 (2025).
13. Ringholz, G. M. *et al.* Prevalence and patterns of cognitive impairment in sporadic ALS. *Neurology* **65**, 586–590 (2005).
14. Hardiman, O. Cognitive and behavioural criteria for ALS-FTD. *Journal of the Neurological Sciences* **455**, 120981 (2023).
15. DeJesus-Hernandez, M. *et al.* Expanded GGGGCC hexanucleotide repeat in noncoding region of C9ORF72 causes chromosome 9p-linked FTD and ALS. *Neuron* **72**, 245–256 (2011).
16. Kwiatkowski, T. J. *et al.* Mutations in the FUS/TLS gene on chromosome 16 cause familial amyotrophic lateral sclerosis. *Science* **323**, 1205–1208 (2009).
17. Deng, H.-X. *et al.* Mutations in UBQLN2 cause dominant X-linked juvenile and adult-onset ALS and ALS/dementia. *Nature* **477**, 211–215 (2011).
18. Al-Sarraj, S. *et al.* p62 positive, TDP-43 negative, neuronal cytoplasmic and intranuclear inclusions in the cerebellum and hippocampus define the pathology of C9orf72-linked FTLD and MND/ALS. *Acta Neuropathol* **122**, 691–702 (2011).
19. Neumann, M. *et al.* Ubiquitinated TDP-43 in Frontotemporal Lobar Degeneration and Amyotrophic Lateral Sclerosis. *Science* **314**, 130–133 (2006).
20. Vance, C. *et al.* Mutations in FUS, an RNA Processing Protein, Cause Familial Amyotrophic Lateral Sclerosis Type 6. *Science* **323**, 1208–1211 (2009).
21. Lagier-Tourenne, C. & Cleveland, D. W. Rethinking ALS: the FUS about TDP-43. *Cell* **136**, 1001–1004 (2009).

22. Maruyama, H. *et al.* Mutations of optineurin in amyotrophic lateral sclerosis. *Nature* **465**, 223–226 (2010).
23. Alexander, E. J. *et al.* Ubiquilin 2 modulates ALS/FTD-linked FUS-RNA complex dynamics and stress granule formation. *Proc Natl Acad Sci U S A* **115**, 11485–11494 (2018).
24. Freischmidt, A. *et al.* Haploinsufficiency of TBK1 causes familial ALS and frontotemporal dementia. *Nat Neurosci* **18**, 631–636 (2015).
25. Koppers, M. *et al.* VCP mutations in familial and sporadic amyotrophic lateral sclerosis. *Neurobiology of Aging* **33**, 837.e7-837.e13 (2012).
26. Saxena, S. & Caroni, P. Selective neuronal vulnerability in neurodegenerative diseases: from stressor thresholds to degeneration. *Neuron* **71**, 35–48 (2011).
27. Cavanagh, J. B. The problems of neurons with long axons. *Lancet* **1**, 1284–1287 (1984).
28. Maday, S. & Holzbaur, E. L. F. Autophagosome Biogenesis in Primary Neurons Follows an Ordered and Spatially Regulated Pathway. *Developmental Cell* **30**, 71–85 (2014).
29. Hegde, A. N. The ubiquitin-proteasome pathway and synaptic plasticity. *Learn. Mem.* **17**, 314–327 (2010).
30. Le Masson, G., Przedborski, S. & Abbott, L. F. A computational model of motor neuron degeneration. *Neuron* **83**, 975–988 (2014).
31. Cuervo, A. M. & Dice, J. F. Age-related decline in chaperone-mediated autophagy. *J Biol Chem* **275**, 31505–31513 (2000).
32. Alvarez-Erviti, L. *et al.* Chaperone-mediated autophagy markers in Parkinson disease brains. *Arch Neurol* **67**, 1464–1472 (2010).
33. Ramesh, N. & Pandey, U. B. Autophagy Dysregulation in ALS: When Protein Aggregates Get Out of Hand. *Front Mol Neurosci* **10**, 263 (2017).

34. Saez, I. & Vilchez, D. The Mechanistic Links Between Proteasome Activity, Aging and Age-related Diseases. *Curr Genomics* **15**, 38–51 (2014).
35. Giandomenico, S. L., Alvarez-Castelao, B. & Schuman, E. M. Proteostatic regulation in neuronal compartments. *Trends Neurosci* **45**, 41–52 (2022).
36. Komander, D. & Rape, M. The ubiquitin code. *Annu Rev Biochem* **81**, 203–229 (2012).
37. Swatek, K. N. & Komander, D. Ubiquitin modifications. *Cell Res* **26**, 399–422 (2016).
38. Wang, X. S. *et al.* The unifying catalytic mechanism of the RING-between-RING E3 ubiquitin ligase family. *Nat Commun* **14**, 168 (2023).
39. Haglund, K., Di Fiore, P. P. & Dikic, I. Distinct monoubiquitin signals in receptor endocytosis. *Trends Biochem Sci* **28**, 598–603 (2003).
40. Grice, G. L. & Nathan, J. A. The recognition of ubiquitinated proteins by the proteasome. *Cell Mol Life Sci* **73**, 3497–3506 (2016).
41. Tokunaga, F. Linear ubiquitination-mediated NF- $\kappa$ B regulation and its related disorders. *J Biochem* **154**, 313–323 (2013).
42. Dósa, A. & Csizmadia, T. The role of K63-linked polyubiquitin in several types of autophagy. *Biol Futur* **73**, 137–148 (2022).
43. Tracz, M. & Bialek, W. Beyond K48 and K63: non-canonical protein ubiquitination. *Cell Mol Biol Lett* **26**, 1 (2021).
44. Castañeda, C. A. *et al.* Linkage via K27 Bestows Ubiquitin Chains with Unique Properties among Polyubiquitins. *Structure* **24**, 423–436 (2016).
45. Nakasone, M. A., Livnat-Levanon, N., Glickman, M. H., Cohen, R. E. & Fushman, D. Mixed-linkage ubiquitin chains send mixed messages. *Structure* **21**, 727–740 (2013).

46. Kolla, S., Ye, M., Mark, K. G. & Rapé, M. Assembly and function of branched ubiquitin chains. *Trends Biochem Sci* **47**, 759–771 (2022).
47. Hurley, J. H., Lee, S. & Prag, G. Ubiquitin-binding domains. *Biochemical Journal* **399**, 361–372 (2006).
48. Michel, M. A., Scutts, S. & Komander, D. Secondary interactions in ubiquitin-binding domains achieve linkage or substrate specificity. *Cell Reports* **44**, 114545 (2024).
49. Kirkin, V., Lamark, T., Johansen, T. & Dikic, I. NBR1 cooperates with p62 in selective autophagy of ubiquitinated targets. *Autophagy* **5**, 732–733 (2009).
50. Kirkin, V. *et al.* A role for NBR1 in autophagosomal degradation of ubiquitinated substrates. *Mol Cell* **33**, 505–516 (2009).
51. Nijman, S. M. B. *et al.* A Genomic and Functional Inventory of Deubiquitinating Enzymes. *Cell* **123**, 773–786 (2005).
52. Snyder, N. A. & Silva, G. M. Deubiquitinating enzymes (DUBs): Regulation, homeostasis, and oxidative stress response. *Journal of Biological Chemistry* **297**, 101077 (2021).
53. Wang, F., Ning, S., Yu, B. & Wang, Y. USP14: Structure, Function, and Target Inhibition. *Front Pharmacol* **12**, 801328 (2021).
54. Lee, B.-H. *et al.* Enhancement of proteasome activity by a small-molecule inhibitor of USP14. *Nature* **467**, 179–184 (2010).
55. Finley, D. & Prado, M. A. The Proteasome and Its Network: Engineering for Adaptability. *Cold Spring Harb Perspect Biol* **12**, a033985 (2020).
56. Groll, M. *et al.* Structure of 20S proteasome from yeast at 2.4 Å resolution. *Nature* **386**, 463–471 (1997).

57. Smith, D. M. *et al.* Docking of the proteasomal ATPases' carboxyl termini in the 20S proteasome's alpha ring opens the gate for substrate entry. *Mol Cell* **27**, 731–744 (2007).
58. Lander, G. C. *et al.* Complete subunit architecture of the proteasome regulatory particle. *Nature* **482**, 186–191 (2012).
59. Verma, R. *et al.* Role of Rpn11 metalloprotease in deubiquitination and degradation by the 26S proteasome. *Science* **298**, 611–615 (2002).
60. Lee, B.-H. *et al.* USP14 deubiquitinates proteasome-bound substrates that are ubiquitinated at multiple sites. *Nature* **532**, 398–401 (2016).
61. Thrower, J. S. Recognition of the polyubiquitin proteolytic signal. *The EMBO Journal* **19**, 94–102 (2000).
62. Husnjak, K. & Dikic, I. Ubiquitin-binding proteins: decoders of ubiquitin-mediated cellular functions. *Annu Rev Biochem* **81**, 291–322 (2012).
63. Bard, J. A. M. *et al.* Structure and Function of the 26S Proteasome. *Annu Rev Biochem* **87**, 697–724 (2018).
64. Dong, Y. *et al.* Cryo-EM structures and dynamics of substrate-engaged human 26S proteasome. *Nature* **565**, 49–55 (2019).
65. Wolozin, B. & Ivanov, P. Stress granules and neurodegeneration. *Nat Rev Neurosci* **20**, 649–666 (2019).
66. Lin, B. C., Higgins, N. R., Phung, T. H. & Monteiro, M. J. UBQLN proteins in health and disease with a focus on UBQLN2 in ALS/FTD. *FEBS J* **289**, 6132–6153 (2022).
67. Nagano, S. & Araki, T. Axonal Transport and Local Translation of mRNA in Neurodegenerative Diseases. *Front Mol Neurosci* **14**, 697973 (2021).
68. Choi, W. H. *et al.* Open-gate mutants of the mammalian proteasome show enhanced ubiquitin-conjugate degradation. *Nat Commun* **7**, 10963 (2016).

69. Mizushima, N. & Komatsu, M. Autophagy: renovation of cells and tissues. *Cell* **147**, 728–741 (2011).
70. Hurley, J. H. & Young, L. N. Mechanisms of Autophagy Initiation. *Annu Rev Biochem* **86**, 225–244 (2017).
71. Johansen, T. & Lamark, T. Selective autophagy mediated by autophagic adapter proteins. *Autophagy* **7**, 279–296 (2011).
72. Chua, J. P., De Calbiac, H., Kabashi, E. & Barmada, S. J. Autophagy and ALS: mechanistic insights and therapeutic implications. *Autophagy* **18**, 254–282 (2022).
73. Schuck, S. Microautophagy – distinct molecular mechanisms handle cargoes of many sizes. *Journal of Cell Science* **133**, jcs246322 (2020).
74. Wang, L., Klionsky, D. J. & Shen, H.-M. The emerging mechanisms and functions of microautophagy. *Nat Rev Mol Cell Biol* **24**, 186–203 (2023).
75. Sahu, R. *et al.* Microautophagy of Cytosolic Proteins by Late Endosomes. *Developmental Cell* **20**, 131–139 (2011).
76. Alonso Y Adell, M., Migliano, S. M. & Teis, D. ESCRT-III and Vps4: a dynamic multipurpose tool for membrane budding and scission. *The FEBS Journal* **283**, 3288–3302 (2016).
77. Adell, M. A. Y. *et al.* Recruitment dynamics of ESCRT-III and Vps4 to endosomes and implications for reverse membrane budding. *eLife* **6**, e31652 (2017).
78. Men, Y. *et al.* ESCRT-I and PTPN23 mediate microautophagy of ubiquitylated tau aggregates. *J Cell Biol* **224**, e202406120 (2025).
79. Sundquist, W. I. *et al.* Ubiquitin Recognition by the Human TSG101 Protein. *Molecular Cell* **13**, 783–789 (2004).
80. Kaushik, S. *et al.* Chaperone-mediated autophagy at a glance. *J Cell Sci* **124**, 495–499 (2011).

81. Chiang, H.-L., Terlecky, S. R., Plant, C. P. & Dice, J. F. A Role for a 70-Kilodalton Heat Shock Protein in Lysosomal Degradation of Intracellular Proteins. *Science* **246**, 382–385 (1989).
82. Cuervo, A. M. & Dice, J. F. A Receptor for the Selective Uptake and Degradation of Proteins by Lysosomes. *Science* **273**, 501–503 (1996).
83. Bandyopadhyay, U., Kaushik, S., Varticovski, L. & Cuervo, A. M. The Chaperone-Mediated Autophagy Receptor Organizes in Dynamic Protein Complexes at the Lysosomal Membrane. *Molecular and Cellular Biology* **28**, 5747–5763 (2008).
84. Kiffin, R. *et al.* Altered dynamics of the lysosomal receptor for chaperone-mediated autophagy with age. *Journal of Cell Science* **120**, 782–791 (2007).
85. Kalmar, B. *et al.* Late stage treatment with arimoclomol delays disease progression and prevents protein aggregation in the SOD1<sup>G93A</sup> mouse model of ALS. *Journal of Neurochemistry* **107**, 339–350 (2008).
86. Xilouri, M. *et al.* Boosting chaperone-mediated autophagy in vivo mitigates  $\alpha$ -synuclein-induced neurodegeneration. *Brain* **136**, 2130–2146 (2013).
87. Turco, E. *et al.* Reconstitution defines the roles of p62, NBR1 and TAX1BP1 in ubiquitin condensate formation and autophagy initiation. *Nat Commun* **12**, 5212 (2021).
88. Zhang, M. *et al.* Mechanistic insights into the interactions of TAX1BP1 with RB1CC1 and mammalian ATG8 family proteins. *Proc Natl Acad Sci U S A* **121**, e2315550121 (2024).
89. Turco, E. *et al.* FIP200 Claw Domain Binding to p62 Promotes Autophagosome Formation at Ubiquitin Condensates. *Mol Cell* **74**, 330-346.e11 (2019).
90. Rubino, E. *et al.* SQSTM1 mutations in frontotemporal lobar degeneration and amyotrophic lateral sclerosis. *Neurology* **79**, 1556–1562 (2012).

91. Ge, P., Dawson, V. L. & Dawson, T. M. PINK1 and Parkin mitochondrial quality control: a source of regional vulnerability in Parkinson's disease. *Mol Neurodegeneration* **15**, 20 (2020).
92. Ravenhill, B. J. *et al.* The Cargo Receptor NDP52 Initiates Selective Autophagy by Recruiting the ULK Complex to Cytosol-Invading Bacteria. *Mol Cell* **74**, 320-329.e6 (2019).
93. Vargas, J. N. S., Hamasaki, M., Kawabata, T., Youle, R. J. & Yoshimori, T. The mechanisms and roles of selective autophagy in mammals. *Nat Rev Mol Cell Biol* **24**, 167–185 (2023).
94. Komatsu, M. *et al.* The selective autophagy substrate p62 activates the stress responsive transcription factor Nrf2 through inactivation of Keap1. *Nat Cell Biol* **12**, 213–223 (2010).
95. Li, C. *et al.* Proteasome Inhibition Activates Autophagy-Lysosome Pathway Associated With TFEB Dephosphorylation and Nuclear Translocation. *Front. Cell Dev. Biol.* **7**, 170 (2019).
96. Kawaguchi, Y. *et al.* The Deacetylase HDAC6 Regulates Aggresome Formation and Cell Viability in Response to Misfolded Protein Stress. *Cell* **115**, 727–738 (2003).
97. Erdbrügger, P. & Wilfling, F. p62 condensates are a hub for proteasome-mediated protein turnover in the nucleus. *Proc Natl Acad Sci U S A* **118**, e2113647118 (2021).
98. Meyer, H. & Weihl, C. C. The VCP/p97 system at a glance: connecting cellular function to disease pathogenesis. *Journal of Cell Science* jcs.093831 (2014) doi:10.1242/jcs.093831.
99. Nillegoda, N. B. *et al.* Crucial HSP70 co-chaperone complex unlocks metazoan protein disaggregation. *Nature* **524**, 247–251 (2015).

100. Braxton, J. R. & Southworth, D. R. Structural insights of the p97/VCP AAA+ ATPase: How adapter interactions coordinate diverse cellular functionality. *J Biol Chem* **299**, 105182 (2023).
101. Tittelmeier, J. *et al.* The HSP110/HSP70 disaggregation system generates spreading-competent toxic  $\alpha$ -synuclein species. *EMBO J* **39**, e103954 (2020).
102. Sun, D., Wu, R., Zheng, J., Li, P. & Yu, L. Polyubiquitin chain-induced p62 phase separation drives autophagic cargo segregation. *Cell Res* **28**, 405–415 (2018).
103. Taguchi, Y. V. *et al.* Hsp110 mitigates  $\alpha$ -synuclein pathology in vivo. *Proc Natl Acad Sci U S A* **116**, 24310–24316 (2019).
104. Gu, J. *et al.* Hsp70 chaperones TDP-43 in dynamic, liquid-like phase and prevents it from amyloid aggregation. *Cell Res* **31**, 1024–1027 (2021).
105. Pensato, V. *et al.* Sorting Rare ALS Genetic Variants by Targeted Re-Sequencing Panel in Italian Patients: OPTN, VCP, and SQSTM1 Variants Account for 3% of Rare Genetic Forms. *J Clin Med* **9**, 412 (2020).
106. Cui, R., Tuo, M., Li, P. & Zhou, C. Association between TBK1 mutations and risk of amyotrophic lateral sclerosis/frontotemporal dementia spectrum: a meta-analysis. *Neurol Sci* **39**, 811–820 (2018).
107. Jakobi, A. J. *et al.* Structural basis of p62/SQSTM1 helical filaments and their role in cellular cargo uptake. *Nat Commun* **11**, 440 (2020).
108. Brenner, D. *et al.* A TBK1 variant causes autophagolysosomal and motoneuron pathology without neuroinflammation in mice. *Journal of Experimental Medicine* **221**, e20221190 (2024).
109. Sarraf, S. A. *et al.* Loss of TAX1BP1-Directed Autophagy Results in Protein Aggregate Accumulation in the Brain. *Mol Cell* **80**, 779-795.e10 (2020).
110. Ohnstad, A. E. *et al.* Receptor-mediated clustering of FIP200 bypasses the role of LC3 lipidation in autophagy. *EMBO J* **39**, e104948 (2020).

111. Kaye, F. J. *et al.* A family of ubiquitin-like proteins binds the ATPase domain of Hsp70-like Stch. *FEBS Lett* **467**, 348–355 (2000).
112. Dao, T. P. *et al.* Ubiquitin Modulates Liquid-Liquid Phase Separation of UBQLN2 via Disruption of Multivalent Interactions. *Mol Cell* **69**, 965-978.e6 (2018).
113. Dao, T. P. *et al.* ALS-Linked Mutations Affect UBQLN2 Oligomerization and Phase Separation in a Position- and Amino Acid-Dependent Manner. *Structure* **27**, 937–9515 (2019).
114. Hjerpe, R. *et al.* UBQLN2 Mediates Autophagy-Independent Protein Aggregate Clearance by the Proteasome. *Cell* **166**, 935–949 (2016).
115. Riley, J. F., Fioramonti, P. J., Rusnock, A. K., Hehnly, H. & Castañeda, C. A. ALS-linked mutations impair UBQLN2 stress-induced biomolecular condensate assembly in cells. *J Neurochem* **159**, 145–155 (2021).
116. Joazeiro, C. A. P. Mechanisms and functions of ribosome-associated protein quality control. *Nat Rev Mol Cell Biol* **20**, 368–383 (2019).
117. Lin, B. C. *et al.* ALS/FTD mutations in UBQLN2 are linked to mitochondrial dysfunction through loss-of-function in mitochondrial protein import. *Hum Mol Genet* **30**, 1230–1246 (2021).
118. Ma, Q. *et al.* UBQLN2 and HSP70 participate in Parkin-mediated mitophagy by facilitating outer mitochondrial membrane rupture. *EMBO Rep* **24**, e55859 (2023).
119. Alberti, S. & Dormann, D. Liquid–Liquid Phase Separation in Disease. *Annu. Rev. Genet.* **53**, 171–194 (2019).
120. Molliex, A. *et al.* Phase Separation by Low Complexity Domains Promotes Stress Granule Assembly and Drives Pathological Fibrillization. *Cell* **163**, 123–133 (2015).

121. Banani, S. F., Lee, H. O., Hyman, A. A. & Rosen, M. K. Biomolecular condensates: organizers of cellular biochemistry. *Nat Rev Mol Cell Biol* **18**, 285–298 (2017).
122. Choi, J.-M., Holehouse, A. S. & Pappu, R. V. Physical Principles Underlying the Complex Biology of Intracellular Phase Transitions. *Annu Rev Biophys* **49**, 107–133 (2020).
123. Sun, D., Wu, R., Zheng, J., Li, P. & Yu, L. Polyubiquitin chain-induced p62 phase separation drives autophagic cargo segregation. *Cell Res* **28**, 405–415 (2018).
124. Hofweber, M. & Dormann, D. Friend or foe-Post-translational modifications as regulators of phase separation and RNP granule dynamics. *J Biol Chem* **294**, 7137–7150 (2019).
125. Patel, A. *et al.* ATP as a biological hydrotrope. *Science* **356**, 753–756 (2017).
126. Yang, P. *et al.* G3BP1 Is a Tunable Switch that Triggers Phase Separation to Assemble Stress Granules. *Cell* **181**, 325-345.e28 (2020).
127. Riggs, C. L., Kedersha, N., Ivanov, P. & Anderson, P. Mammalian stress granules and P bodies at a glance. *Journal of Cell Science* **133**, jcs242487 (2020).
128. Zeng, M. *et al.* Phase Transition in Postsynaptic Densities Underlies Formation of Synaptic Complexes and Synaptic Plasticity. *Cell* **166**, 1163-1175.e12 (2016).
129. Kiebler, M. A. & Bauer, K. E. RNA granules in flux: dynamics to balance physiology and pathology. *Nat. Rev. Neurosci.* **25**, 711–725 (2024).
130. Guillén-Boixet, J. *et al.* RNA-Induced Conformational Switching and Clustering of G3BP Drive Stress Granule Assembly by Condensation. *Cell* **181**, 346-361.e17 (2020).
131. Kim, H. J. *et al.* Mutations in prion-like domains in hnRNPA2B1 and hnRNPA1 cause multisystem proteinopathy and ALS. *Nature* **495**, 467–473 (2013).

132. Gasset-Rosa, F. *et al.* Cytoplasmic TDP-43 De-mixing Independent of Stress Granules Drives Inhibition of Nuclear Import, Loss of Nuclear TDP-43, and Cell Death. *Neuron* **102**, 339-357.e7 (2019).
133. Mann, J. R. *et al.* RNA Binding Antagonizes Neurotoxic Phase Transitions of TDP-43. *Neuron* **102**, 321-338.e8 (2019).
134. McGurk, L. *et al.* Poly(ADP-Ribose) Prevents Pathological Phase Separation of TDP-43 by Promoting Liquid Demixing and Stress Granule Localization. *Mol Cell* **71**, 703-717.e9 (2018).
135. Buchan, J. R., Kolaitis, R.-M., Taylor, J. P. & Parker, R. Eukaryotic stress granules are cleared by autophagy and Cdc48/VCP function. *Cell* **153**, 1461–1474 (2013).
136. Uechi, H. *et al.* Small-molecule dissolution of stress granules by redox modulation benefits ALS models. *Nat Chem Biol* (2025) doi:10.1038/s41589-025-01893-5.
137. Ryan, L. & Rubinsztein, D. C. The autophagy of stress granules. *FEBS Lett* **598**, 59–72 (2024).
138. Lin, Y., Protter, D. S. W., Rosen, M. K. & Parker, R. Formation and Maturation of Phase-Separated Liquid Droplets by RNA-Binding Proteins. *Mol Cell* **60**, 208–219 (2015).
139. Jawerth, L. *et al.* Protein condensates as aging Maxwell fluids. *Science* **370**, 1317–1323 (2020).
140. Lee, C. F., Bird, S., Shaw, M., Jean, L. & Vaux, D. J. Combined effects of agitation, macromolecular crowding, and interfaces on amyloidogenesis. *J Biol Chem* **287**, 38006–38019 (2012).
141. Shuster, S. O. & Lee, J. C. Watching liquid droplets of TDP-43CTD age by Raman spectroscopy. *J Biol Chem* **298**, 101528 (2022).

142. Patel, A. *et al.* A Liquid-to-Solid Phase Transition of the ALS Protein FUS Accelerated by Disease Mutation. *Cell* **162**, 1066–1077 (2015).
143. Brangwynne, C. P. *et al.* Germline P Granules Are Liquid Droplets That Localize by Controlled Dissolution/Condensation. *Science* **324**, 1729–1732 (2009).
144. Mondal, M. *et al.* Reversible Disulfide Bond Cross-Links as Tunable Levers of Phase Separation in Designer Biomolecular Condensates. *J. Am. Chem. Soc.* **146**, 25299–25311 (2024).
145. Maharana, S. *et al.* RNA buffers the phase separation behavior of prion-like RNA binding proteins. *Science* **360**, 918–921 (2018).
146. Linsenmeier, M. *et al.* The interface of condensates of the hnRNPA1 low-complexity domain promotes formation of amyloid fibrils. *Nat. Chem.* **15**, 1340–1349 (2023).
147. Alberti, S. & Carra, S. Quality Control of Membraneless Organelles. *Journal of Molecular Biology* **430**, 4711–4729 (2018).
148. Zhang, H. *et al.* Reversible phase separation of HSF1 is required for an acute transcriptional response during heat shock. *Nat Cell Biol* **24**, 340–352 (2022).
149. Lu, S. *et al.* Heat-shock chaperone HSPB1 regulates cytoplasmic TDP-43 phase separation and liquid-to-gel transition. *Nat Cell Biol* **24**, 1378–1393 (2022).
150. Krause, L. J., Herrera, M. G. & Winklhofer, K. F. The Role of Ubiquitin in Regulating Stress Granule Dynamics. *Front Physiol* **13**, 910759 (2022).
151. Sternburg, E. L., Gruijs da Silva, L. A. & Dormann, D. Post-translational modifications on RNA-binding proteins: accelerators, brakes, or passengers in neurodegeneration? *Trends Biochem Sci* **47**, 6–22 (2022).
152. Gruijs Da Silva, L. A. *et al.* Disease-linked TDP-43 hyperphosphorylation suppresses TDP-43 condensation and aggregation. *The EMBO Journal* **41**, e108443 (2022).

153. Hofweber, M. *et al.* Phase Separation of FUS Is Suppressed by Its Nuclear Import Receptor and Arginine Methylation. *Cell* **173**, 706-719.e13 (2018).
154. Keiten-Schmitz, J., Röder, L., Hornstein, E., Müller-McNicoll, M. & Müller, S. SUMO: Glue or Solvent for Phase-Separated Ribonucleoprotein Complexes and Molecular Condensates? *Front. Mol. Biosci.* **8**, 673038 (2021).
155. Liang, P., Zhang, J. & Wang, B. Emerging Roles of Ubiquitination in Biomolecular Condensates. *Cells* **12**, 2329 (2023).
156. Pyle, A. M. RNA helicases and remodeling proteins. *Curr Opin Chem Biol* **15**, 636–642 (2011).
157. Hondele, M. *et al.* DEAD-box ATPases are global regulators of phase-separated organelles. *Nature* **573**, 144–148 (2019).
158. Wang, B. *et al.* ULK1 and ULK2 Regulate Stress Granule Disassembly Through Phosphorylation and Activation of VCP/p97. *Mol Cell* **74**, 742-757.e8 (2019).
159. Maharana, S. *et al.* RNA buffers the phase separation behavior of prion-like RNA binding proteins. *Science* **360**, 918–921 (2018).
160. Tollervey, J. R. *et al.* Characterizing the RNA targets and position-dependent splicing regulation by TDP-43. *Nat Neurosci* **14**, 452–458 (2011).
161. Lukavsky, P. J. *et al.* Molecular basis of UG-rich RNA recognition by the human splicing factor TDP-43. *Nat Struct Mol Biol* **20**, 1443–1449 (2013).
162. Ling, J. P., Pletnikova, O., Troncoso, J. C. & Wong, P. C. TDP-43 repression of nonconserved cryptic exons is compromised in ALS-FTD. *Science* **349**, 650–655 (2015).
163. Ratti, A. & Buratti, E. Physiological functions and pathobiology of TDP-43 and FUS/TLS proteins. *J Neurochem* **138 Suppl 1**, 95–111 (2016).

164. Polymenidou, M. *et al.* Long pre-mRNA depletion and RNA missplicing contribute to neuronal vulnerability from loss of TDP-43. *Nat Neurosci* **14**, 459–468 (2011).
165. Alami, N. H. *et al.* Axonal transport of TDP-43 mRNA granules is impaired by ALS-causing mutations. *Neuron* **81**, 536–543 (2014).
166. Ou, S. H., Wu, F., Harrich, D., García-Martínez, L. F. & Gaynor, R. B. Cloning and characterization of a novel cellular protein, TDP-43, that binds to human immunodeficiency virus type 1 TAR DNA sequence motifs. *J Virol* **69**, 3584–3596 (1995).
167. Wood, M. *et al.* TDP-43 dysfunction results in R-loop accumulation and DNA replication defects. *J Cell Sci* **133**, jcs244129 (2020).
168. Bowden, H. A. & Dormann, D. Altered mRNP granule dynamics in FTLD pathogenesis. *J Neurochem* **138 Suppl 1**, 112–133 (2016).
169. Dewey, C. M. *et al.* TDP-43 is directed to stress granules by sorbitol, a novel physiological osmotic and oxidative stressor. *Mol Cell Biol* **31**, 1098–1108 (2011).
170. Aulas, A., Stabile, S. & Vande Velde, C. Endogenous TDP-43, but not FUS, contributes to stress granule assembly via G3BP. *Mol Neurodegener* **7**, 54 (2012).
171. Doll, S. G. *et al.* Recognition of the TDP-43 nuclear localization signal by importin  $\alpha$ 1/ $\beta$ . *Cell Rep* **39**, 111007 (2022).
172. Pinarbasi, E. S. *et al.* Active nuclear import and passive nuclear export are the primary determinants of TDP-43 localization. *Sci Rep* **8**, 7083 (2018).
173. Ederle, H. *et al.* Nuclear egress of TDP-43 and FUS occurs independently of Exportin-1/CRM1. *Sci Rep* **8**, 7084 (2018).

174. Liscic, R. M., Grinberg, L. T., Zidar, J., Gitcho, M. A. & Cairns, N. J. ALS and FTL: two faces of TDP-43 proteinopathy. *Eur J Neurol* **15**, 772–780 (2008).
175. Sreedharan, J. *et al.* TDP-43 Mutations in Familial and Sporadic Amyotrophic Lateral Sclerosis. *Science* **319**, 1668–1672 (2008).
176. Buratti, E. Functional Significance of TDP-43 Mutations in Disease. *Adv Genet* **91**, 1–53 (2015).
177. Tziortzouda, P., Van Den Bosch, L. & Hirth, F. Triad of TDP43 control in neurodegeneration: autoregulation, localization and aggregation. *Nat Rev Neurosci* **22**, 197–208 (2021).
178. Chiang, C.-H. *et al.* Structural analysis of disease-related TDP-43 D169G mutation: linking enhanced stability and caspase cleavage efficiency to protein accumulation. *Sci Rep* **6**, 21581 (2016).
179. Estes, P. S. *et al.* Wild-type and A315T mutant TDP-43 exert differential neurotoxicity in a *Drosophila* model of ALS. *Hum Mol Genet* **20**, 2308–2321 (2011).
180. Conicella, A. E. *et al.* TDP-43  $\alpha$ -helical structure tunes liquid-liquid phase separation and function. *Proc Natl Acad Sci U S A* **117**, 5883–5894 (2020).
181. Liu-Yesucevitz, L. *et al.* ALS-linked mutations enlarge TDP-43-enriched neuronal RNA granules in the dendritic arbor. *J Neurosci* **34**, 4167–4174 (2014).
182. Barmada, S. J. *et al.* Cytoplasmic mislocalization of TDP-43 is toxic to neurons and enhanced by a mutation associated with familial amyotrophic lateral sclerosis. *J Neurosci* **30**, 639–649 (2010).
183. Conicella, A. E., Zerze, G. H., Mittal, J. & Fawzi, N. L. ALS Mutations Disrupt Phase Separation Mediated by  $\alpha$ -Helical Structure in the TDP-43 Low-Complexity C-Terminal Domain. *Structure* **24**, 1537–1549 (2016).

184. Kabashi, E., Brustein, E., Champagne, N. & Drapeau, P. Zebrafish models for the functional genomics of neurogenetic disorders. *Biochimica et Biophysica Acta (BBA) - Molecular Basis of Disease* **1812**, 335–345 (2011).
185. Ni, J. *et al.* Loss of TDP-43 function underlies hippocampal and cortical synaptic deficits in TDP-43 proteinopathies. *Mol Psychiatry* **28**, 931–945 (2023).
186. Mackenzie, I. R. A. & Neumann, M. Molecular neuropathology of frontotemporal dementia: insights into disease mechanisms from postmortem studies. *J Neurochem* **138 Suppl 1**, 54–70 (2016).
187. Liu, E. Y. *et al.* Loss of Nuclear TDP-43 Is Associated with Decondensation of LINE Retrotransposons. *Cell Reports* **27**, 1409-1421.e6 (2019).
188. Hayes, L. R. & Kalab, P. Emerging Therapies and Novel Targets for TDP-43 Proteinopathy in ALS/FTD. *Neurotherapeutics* **19**, 1061–1084 (2022).
189. Rummens, J. *et al.* TDP-43 seeding induces cytoplasmic aggregation heterogeneity and nuclear loss of function of TDP-43. *Neuron* **113**, 1597-1613.e8 (2025).
190. Scialò, C. *et al.* Seeded aggregation of TDP-43 induces its loss of function and reveals early pathological signatures. *Neuron* **113**, 1614-1628.e11 (2025).
191. Neumann, M. Molecular Neuropathology of TDP-43 Proteinopathies. *IJMS* **10**, 232–246 (2009).
192. Afroz, T. *et al.* Functional and dynamic polymerization of the ALS-linked protein TDP-43 antagonizes its pathologic aggregation. *Nat Commun* **8**, 45 (2017).
193. Mompeán, M. *et al.* The TDP-43 N-terminal domain structure at high resolution. *FEBS J* **283**, 1242–1260 (2016).
194. Wang, A. *et al.* A single N-terminal phosphomimic disrupts TDP-43 polymerization, phase separation, and RNA splicing. *EMBO J* **37**, e97452 (2018).

195. Buratti, E. & Baralle, F. E. Characterization and Functional Implications of the RNA Binding Properties of Nuclear Factor TDP-43, a Novel Splicing Regulator of CFTR Exon 9. *Journal of Biological Chemistry* **276**, 36337–36343 (2001).
196. Buratti, E. & Baralle, F. E. Characterization and Functional Implications of the RNA Binding Properties of Nuclear Factor TDP-43, a Novel Splicing Regulator of CFTR Exon 9. *Journal of Biological Chemistry* **276**, 36337–36343 (2001).
197. Gopal, P. P., Nirschl, J. J., Klinman, E. & Holzbaur, E. L. F. Amyotrophic lateral sclerosis-linked mutations increase the viscosity of liquid-like TDP-43 RNP granules in neurons. *Proc Natl Acad Sci U S A* **114**, E2466–E2475 (2017).
198. Guenther, E. L. *et al.* Atomic structures of TDP-43 LCD segments and insights into reversible or pathogenic aggregation. *Nat Struct Mol Biol* **25**, 463–471 (2018).
199. Arseni, D. *et al.* Structure of pathological TDP-43 filaments from ALS with FTLD. *Nature* **601**, 139–143 (2022).
200. Arseni, D. *et al.* TDP-43 forms amyloid filaments with a distinct fold in type A FTLD-TDP. *Nature* **620**, 898–903 (2023).
201. Arseni, D. *et al.* Heteromeric amyloid filaments of ANXA11 and TDP-43 in FTLD-TDP type C. *Nature* **634**, 662–668 (2024).
202. Hasegawa, M. *et al.* Phosphorylated TDP-43 in frontotemporal lobar degeneration and amyotrophic lateral sclerosis. *Ann Neurol* **64**, 60–70 (2008).
203. Kametani, F. *et al.* Mass spectrometric analysis of accumulated TDP-43 in amyotrophic lateral sclerosis brains. *Sci Rep* **6**, 23281 (2016).
204. Cracco, L. *et al.* Distinguishing post-translational modifications in dominantly inherited frontotemporal dementias: FTLD-TDP Type A (GRN) vs Type B (C9orf72). *Neuropathol Appl Neurobiol* **48**, e12836 (2022).

205. Rabhi, C. *et al.* TDP-43 nuclear retention is antagonized by hypo-phosphorylation of its C-terminus in the cytoplasm. *Commun Biol* **8**, 136 (2025).
206. Kellett, E. A., Bademosi, A. T. & Walker, A. K. Molecular mechanisms and consequences of TDP-43 phosphorylation in neurodegeneration. *Mol Neurodegeneration* **20**, 53 (2025).
207. Nakayama, Y. *et al.* Linear Polyubiquitin Chain Modification of TDP-43-Positive Neuronal Cytoplasmic Inclusions in Amyotrophic Lateral Sclerosis. *J Neuropathol Exp Neurol* **79**, 256–265 (2020).
208. Hans, F., Eckert, M., von Zweydford, F., Gloeckner, C. J. & Kahle, P. J. Identification and characterization of ubiquitinylation sites in TAR DNA-binding protein of 43 kDa (TDP-43). *J Biol Chem* **293**, 16083–16099 (2018).
209. Hebron, M. L. *et al.* Parkin ubiquitinates Tar-DNA binding protein-43 (TDP-43) and promotes its cytosolic accumulation via interaction with histone deacetylase 6 (HDAC6). *J Biol Chem* **288**, 4103–4115 (2013).
210. Ma, P., Li, Y., Wang, H. & Mao, B. Haploinsufficiency of the TDP43 ubiquitin E3 ligase RNF220 leads to ALS-like motor neuron defects in the mouse. *J Mol Cell Biol* **13**, 374–382 (2021).
211. Suk, T. R. *et al.* A stress-dependent TDP-43 SUMOylation program preserves neuronal function. *Mol Neurodegeneration* **20**, 38 (2025).
212. Verde, E. M. *et al.* SUMO2/3 conjugation of TDP-43 protects against aggregation. *Sci Adv* **11**, eadq2475 (2025).
213. Wagner, K. *et al.* Induced proximity to PML protects TDP-43 from aggregation via SUMO–ubiquitin networks. *Nat Chem Biol* **21**, 1408–1419 (2025).
214. Zhang, S. *et al.* Acetylation of lysine 82 initiates TDP-43 nuclear loss of function by disrupting its nuclear import. Preprint at <https://doi.org/10.1101/2024.09.04.611121> (2024).

215. Ko, Y.-H. *et al.* Single Acetylation-mimetic Mutation in TDP-43 Nuclear Localization Signal Disrupts Importin  $\alpha 1/\beta$  Signaling. *J Mol Biol* **436**, 168751 (2024).
216. Garcia Morato, J. *et al.* Sirtuin-1 sensitive lysine-136 acetylation drives phase separation and pathological aggregation of TDP-43. *Nat Commun* **13**, 1223 (2022).
217. Cohen, T. J. *et al.* An acetylation switch controls TDP-43 function and aggregation propensity. *Nat Commun* **6**, 5845 (2015).
218. Zhang, Y.-J. *et al.* Aberrant cleavage of TDP-43 enhances aggregation and cellular toxicity. *Proc Natl Acad Sci U S A* **106**, 7607–7612 (2009).
219. Igaz, L. M. *et al.* Enrichment of C-Terminal Fragments in TAR DNA-Binding Protein-43 Cytoplasmic Inclusions in Brain but not in Spinal Cord of Frontotemporal Lobar Degeneration and Amyotrophic Lateral Sclerosis. *The American Journal of Pathology* **173**, 182–194 (2008).
220. Yamashita, T. *et al.* A role for calpain-dependent cleavage of TDP-43 in amyotrophic lateral sclerosis pathology. *Nat Commun* **3**, 1307 (2012).
221. Gao, J., Wang, L., Huntley, M. L., Perry, G. & Wang, X. Pathomechanisms of TDP-43 in neurodegeneration. *J Neurochem* (2018) doi:10.1111/jnc.14327.
222. Berning, B. A. & Walker, A. K. The Pathobiology of TDP-43 C-Terminal Fragments in ALS and FTL. *Front. Neurosci.* **13**, 335 (2019).
223. Mateju, D. *et al.* An aberrant phase transition of stress granules triggered by misfolded protein and prevented by chaperone function. *EMBO J* **36**, 1669–1687 (2017).
224. Boczek, E. E. *et al.* HspB8 prevents aberrant phase transitions of FUS by chaperoning its folded RNA-binding domain. *Elife* **10**, e69377 (2021).

225. Webster, J. M., Darling, A. L., Uversky, V. N. & Blair, L. J. Small Heat Shock Proteins, Big Impact on Protein Aggregation in Neurodegenerative Disease. *Front Pharmacol* **10**, 1047 (2019).
226. Ganassi, M. *et al.* A Surveillance Function of the HSPB8-BAG3-HSP70 Chaperone Complex Ensures Stress Granule Integrity and Dynamism. *Mol Cell* **63**, 796–810 (2016).
227. Moens, T. G. *et al.* Amyotrophic lateral sclerosis caused by FUS mutations: advances with broad implications. *Lancet Neurol* **24**, 166–178 (2025).
228. Qamar, S. *et al.* FUS Phase Separation Is Modulated by a Molecular Chaperone and Methylation of Arginine Cation- $\pi$  Interactions. *Cell* **173**, 720-734.e15 (2018).
229. Wang, J. *et al.* A Molecular Grammar Governing the Driving Forces for Phase Separation of Prion-like RNA Binding Proteins. *Cell* **174**, 688-699.e16 (2018).
230. Zhang, Z. C. & Chook, Y. M. Structural and energetic basis of ALS-causing mutations in the atypical proline-tyrosine nuclear localization signal of the Fused in Sarcoma protein (FUS). *Proc Natl Acad Sci U S A* **109**, 12017–12021 (2012).
231. Kato, M. *et al.* Cell-free formation of RNA granules: low complexity sequence domains form dynamic fibers within hydrogels. *Cell* **149**, 753–767 (2012).
232. Loughlin, F. E. *et al.* The Solution Structure of FUS Bound to RNA Reveals a Bipartite Mode of RNA Recognition with Both Sequence and Shape Specificity. *Mol Cell* **73**, 490-504.e6 (2019).
233. Ederle, H. & Dormann, D. TDP-43 and FUS en route from the nucleus to the cytoplasm. *FEBS Lett* **591**, 1489–1507 (2017).
234. Fujii, R. *et al.* The RNA binding protein TLS is translocated to dendritic spines by mGluR5 activation and regulates spine morphology. *Curr Biol* **15**, 587–593 (2005).

235. Ishigaki, S. *et al.* Position-dependent FUS-RNA interactions regulate alternative splicing events and transcriptions. *Sci Rep* **2**, 529 (2012).
236. Ma, X. R. *et al.* TDP-43 represses cryptic exon inclusion in the FTD-ALS gene UNC13A. *Nature* **603**, 124–130 (2022).
237. Dormann, D. *et al.* ALS-associated fused in sarcoma (FUS) mutations disrupt Transportin-mediated nuclear import. *EMBO J* **29**, 2841–2857 (2010).
238. Yoshizawa, T. *et al.* Nuclear Import Receptor Inhibits Phase Separation of FUS through Binding to Multiple Sites. *Cell* **173**, 693-705.e22 (2018).
239. Nonaka, T. *et al.* Phosphorylation of TAR DNA-binding Protein of 43 kDa (TDP-43) by Truncated Casein Kinase 1 $\delta$  Triggers Mislocalization and Accumulation of TDP-43. *J Biol Chem* **291**, 5473–5483 (2016).
240. Guo, L. *et al.* Nuclear-Import Receptors Reverse Aberrant Phase Transitions of RNA-Binding Proteins with Prion-like Domains. *Cell* **173**, 677-692.e20 (2018).
241. Korobeynikov, V. A., Lyashchenko, A. K., Blanco-Redondo, B., Jafar-Nejad, P. & Shneider, N. A. Antisense oligonucleotide silencing of FUS expression as a therapeutic approach in amyotrophic lateral sclerosis. *Nat Med* **28**, 104–116 (2022).
242. Devoy, A. *et al.* Humanized mutant FUS drives progressive motor neuron degeneration without aggregation in ‘FUSDelta14’ knockin mice. *Brain* **140**, 2797–2805 (2017).
243. Kapeli, K. *et al.* Distinct and shared functions of ALS-associated proteins TDP-43, FUS and TAF15 revealed by multisystem analyses. *Nat Commun* **7**, 12143 (2016).
244. Chou, C.-C. *et al.* TDP-43 pathology disrupts nuclear pore complexes and nucleocytoplasmic transport in ALS/FTD. *Nat Neurosci* **21**, 228–239 (2018).

245. Urwin, H. *et al.* FUS pathology defines the majority of tau- and TDP-43-negative frontotemporal lobar degeneration. *Acta Neuropathol* **120**, 33–41 (2010).
246. Neumann, M., Lee, E. B. & Mackenzie, I. R. Frontotemporal Lobar Degeneration TDP-43-Immunoreactive Pathological Subtypes: Clinical and Mechanistic Significance. *Adv Exp Med Biol* **1281**, 201–217 (2021).
247. Dormann, D. *et al.* Arginine methylation next to the PY-NLS modulates Transportin binding and nuclear import of FUS: Arginine methylation of FUS impairs TRN binding. *The EMBO Journal* **31**, 4258–4275 (2012).
248. Suárez-Calvet, M. *et al.* Monomethylated and unmethylated FUS exhibit increased binding to Transportin and distinguish FTL-D-FUS from ALS-FUS. *Acta Neuropathol* **131**, 587–604 (2016).
249. Chen, X. *et al.* Structure of hRpn10 Bound to UBQLN2 UBL Illustrates Basis for Complementarity between Shuttle Factors and Substrates at the Proteasome. *J Mol Biol* **431**, 939–955 (2019).
250. Chen, X. *et al.* Structures of Rpn1 T1:Rad23 and hRpn13:hPLIC2 Reveal Distinct Binding Mechanisms between Substrate Receptors and Shuttle Factors of the Proteasome. *Structure* **24**, 1257–1270 (2016).
251. Kaye, F. J. *et al.* A family of ubiquitin-like proteins binds the ATPase domain of Hsp70-like Stch. *FEBS Letters* **467**, 348–355 (2000).
252. Rothenberg, C. *et al.* Ubiquilin functions in autophagy and is degraded by chaperone-mediated autophagy. *Hum Mol Genet* **19**, 3219–3232 (2010).
253. Phung, T. H., Tatman, M. & Monteiro, M. J. UBQLN2 undergoes a reversible temperature-induced conformational switch that regulates binding with HSPA1B: ALS/FTD mutations cripple the switch but do not destroy HSPA1B binding. *Biochim Biophys Acta Gen Subj* **1867**, 130284 (2023).

254. Şentürk, M. *et al.* Ubiquilins regulate autophagic flux through mTOR signalling and lysosomal acidification. *Nat Cell Biol* **21**, 384–396 (2019).
255. Le, N. T. T. *et al.* Motor neuron disease, TDP-43 pathology, and memory deficits in mice expressing ALS-FTD-linked UBQLN2 mutations. *Proc Natl Acad Sci U S A* **113**, E7580–E7589 (2016).
256. Chang, L. & Monteiro, M. J. Defective Proteasome Delivery of Polyubiquitinated Proteins by Ubiquilin-2 Proteins Containing ALS Mutations. *PLoS One* **10**, e0130162 (2015).
257. Halloran, M. *et al.* Amyotrophic lateral sclerosis-linked UBQLN2 mutants inhibit endoplasmic reticulum to Golgi transport, leading to Golgi fragmentation and ER stress. *Cell Mol Life Sci* **77**, 3859–3873 (2020).
258. Silva, M. C. *et al.* Targeted degradation of aberrant tau in frontotemporal dementia patient-derived neuronal cell models. *Elife* **8**, e45457 (2019).
259. Takahashi, D. *et al.* AUTACs: Cargo-Specific Degradation Using Selective Autophagy. *Mol Cell* **76**, 797-810.e10 (2019).
260. Li, Z. *et al.* Allele-selective lowering of mutant HTT protein by HTT-LC3 linker compounds. *Nature* **575**, 203–209 (2019).
261. Benatar, M. *et al.* Safety and efficacy of arimoclomol in patients with early amyotrophic lateral sclerosis (ORARIALS-01): a randomised, double-blind, placebo-controlled, multicentre, phase 3 trial. *Lancet Neurol* **23**, 687–699 (2024).
262. Njomen, E., Osmulski, P. A., Jones, C. L., Gaczynska, M. & Tepe, J. J. Small Molecule Modulation of Proteasome Assembly. *Biochemistry* **57**, 4214–4224 (2018).
263. Trader, D. J., Simanski, S., Dickson, P. & Kodadek, T. Establishment of a suite of assays that support the discovery of proteasome stimulators. *Biochim Biophys Acta Gen Subj* **1861**, 892–899 (2017).

264. D'Arcy, P. *et al.* Inhibition of proteasome deubiquitinating activity as a new cancer therapy. *Nat Med* **17**, 1636–1640 (2011).
265. Wang, X. *et al.* The proteasome deubiquitinase inhibitor VLX1570 shows selectivity for ubiquitin-specific protease-14 and induces apoptosis of multiple myeloma cells. *Sci Rep* **6**, 26979 (2016).
266. Huang, Z.-N., Lee, S.-Y., Chen, J.-M., Huang, Z.-T. & Her, L.-S. Oleuropein enhances proteasomal activity and reduces mutant huntingtin-induced cytotoxicity. *Front Pharmacol* **15**, 1459909 (2024).
267. Anderson, C. *et al.* Loss of Usp14 results in reduced levels of ubiquitin in ataxia mice. *J Neurochem* **95**, 724–731 (2005).
268. Kloetzel, P.-M. The proteasome and MHC class I antigen processing. *Biochim Biophys Acta* **1695**, 225–233 (2004).
269. Mandrioli, J. *et al.* Randomized, double-blind, placebo-controlled trial of rapamycin in amyotrophic lateral sclerosis. *Nat Commun* **14**, 4970 (2023).
270. HEALEY ALS Platform Trial & HEALEY ALS Platform Trial Study Group. Safety and efficacy of trehalose in amyotrophic lateral sclerosis (HEALEY ALS Platform Trial): an adaptive, phase 2/3, double-blind, randomised, placebo-controlled trial. *Lancet Neurol* **24**, 500–511 (2025).
271. Sarkar, S. *et al.* Small molecules enhance autophagy and reduce toxicity in Huntington's disease models. *Nat Chem Biol* **3**, 331–338 (2007).
272. Perera, N. D. *et al.* Rilmenidine promotes MTOR-independent autophagy in the mutant SOD1 mouse model of amyotrophic lateral sclerosis without slowing disease progression. *Autophagy* **14**, 534–551 (2018).
273. Williams, A. *et al.* Novel targets for Huntington's disease in an mTOR-independent autophagy pathway. *Nat Chem Biol* **4**, 295–305 (2008).

274. Sarkar, S. *et al.* Lithium induces autophagy by inhibiting inositol monophosphatase. *J Cell Biol* **170**, 1101–1111 (2005).
275. Shoji-Kawata, S. *et al.* Identification of a candidate therapeutic autophagy-inducing peptide. *Nature* **494**, 201–206 (2013).
276. Kane, L. A. *et al.* PINK1 phosphorylates ubiquitin to activate Parkin E3 ubiquitin ligase activity. *J Cell Biol* **205**, 143–153 (2014).
277. Kazlauskaitė, A. *et al.* Parkin is activated by PINK1-dependent phosphorylation of ubiquitin at Ser65. *Biochem J* **460**, 127–139 (2014).
278. Deane, C. A. S. & Brown, I. R. Induction of heat shock proteins in differentiated human neuronal cells following co-application of celastrol and arimoclomol. *Cell Stress Chaperones* **21**, 837–848 (2016).
279. Neef, D. W., Turski, M. L. & Thiele, D. J. Modulation of heat shock transcription factor 1 as a therapeutic target for small molecule intervention in neurodegenerative disease. *PLoS Biol* **8**, e1000291 (2010).
280. Benatar, M. *et al.* Safety and efficacy of arimoclomol in patients with early amyotrophic lateral sclerosis (ORARIALS-01): a randomised, double-blind, placebo-controlled, multicentre, phase 3 trial. *Lancet Neurol* **23**, 687–699 (2024).
281. Boyault, C. *et al.* HDAC6 controls major cell response pathways to cytotoxic accumulation of protein aggregates. *Genes Dev* **21**, 2172–2181 (2007).
282. Zhong, G., Chang, X., Xie, W. & Zhou, X. Targeted protein degradation: advances in drug discovery and clinical practice. *Signal Transduct Target Ther* **9**, 308 (2024).
283. Wang, W. *et al.* A novel small-molecule PROTAC selectively promotes tau clearance to improve cognitive functions in Alzheimer-like models. *Theranostics* **11**, 5279–5295 (2021).

284. Takahashi, D. *et al.* AUTACs: Cargo-Specific Degradation Using Selective Autophagy. *Mol Cell* **76**, 797-810.e10 (2019).
285. Salama, A. K. A. A., Trkulja, M. V., Casanova, E. & Uras, I. Z. Targeted Protein Degradation: Clinical Advances in the Field of Oncology. *Int J Mol Sci* **23**, 15440 (2022).
286. Scotter, E. L. *et al.* Differential roles of the ubiquitin proteasome system and autophagy in the clearance of soluble and aggregated TDP-43 species. *J Cell Sci* **127**, 1263–1278 (2014).
287. Hergesheimer, R. C. *et al.* The debated toxic role of aggregated TDP-43 in amyotrophic lateral sclerosis: a resolution in sight? *Brain* **142**, 1176–1194 (2019).
288. Lee, E. B., Lee, V. M.-Y. & Trojanowski, J. Q. Gains or losses: molecular mechanisms of TDP43-mediated neurodegeneration. *Nat Rev Neurosci* **13**, 38–50 (2011).
289. Guo, F., Liu, X., Cai, H. & Le, W. Autophagy in neurodegenerative diseases: pathogenesis and therapy. *Brain Pathol* **28**, 3–13 (2018).
290. Dantuma, N. P. & Bott, L. C. The ubiquitin-proteasome system in neurodegenerative diseases: precipitating factor, yet part of the solution. *Front. Mol. Neurosci.* **7**, (2014).
291. Root, J., Merino, P., Nuckols, A., Johnson, M. & Kukar, T. Lysosome dysfunction as a cause of neurodegenerative diseases: Lessons from frontotemporal dementia and amyotrophic lateral sclerosis. *Neurobiology of Disease* **154**, 105360 (2021).
292. Koulouras, G. *et al.* EasyFRAP-web: a web-based tool for the analysis of fluorescence recovery after photobleaching data. *Nucleic Acids Res* **46**, W467–W472 (2018).

293. Hughes, C. S. *et al.* Single-pot, solid-phase-enhanced sample preparation for proteomics experiments. *Nat Protoc* **14**, 68–85 (2019).
294. Rappsilber, J., Ishihama, Y. & Mann, M. Stop and go extraction tips for matrix-assisted laser desorption/ionization, nanoelectrospray, and LC/MS sample pretreatment in proteomics. *Anal Chem* **75**, 663–670 (2003).
295. Cox, J. & Mann, M. MaxQuant enables high peptide identification rates, individualized p.p.b.-range mass accuracies and proteome-wide protein quantification. *Nat Biotechnol* **26**, 1367–1372 (2008).
296. Kong, A. T., Leprevost, F. V., Avtonomov, D. M., Mellacheruvu, D. & Nesvizhskii, A. I. MSFragger: ultrafast and comprehensive peptide identification in mass spectrometry-based proteomics. *Nat Methods* **14**, 513–520 (2017).
297. Demichev, V. *et al.* dia-PASEF data analysis using FragPipe and DIA-NN for deep proteomics of low sample amounts. *Nat Commun* **13**, 3944 (2022).
298. da Veiga Leprevost, F. *et al.* Philosopher: a versatile toolkit for shotgun proteomics data analysis. *Nat Methods* **17**, 869–870 (2020).
299. Kuleshov, M. V. *et al.* Enrichr: a comprehensive gene set enrichment analysis web server 2016 update. *Nucleic Acids Res* **44**, W90-97 (2016).
300. Oughtred, R. *et al.* The BioGRID interaction database: 2019 update. *Nucleic Acids Res* **47**, D529–D541 (2019).
301. Lashley, T. *et al.* A comparative clinical, pathological, biochemical and genetic study of fused in sarcoma proteinopathies. *Brain* **134**, 2548–2564 (2011).
302. Licheva, M. *et al.* Phase separation of initiation hubs on cargo is a trigger switch for selective autophagy. *Nat Cell Biol* **27**, 283–297 (2025).
303. Mastronarde, D. N. Automated electron microscope tomography using robust prediction of specimen movements. *J Struct Biol* **152**, 36–51 (2005).

304. Hagen, W. J. H., Wan, W. & Briggs, J. A. G. Implementation of a cryo-electron tomography tilt-scheme optimized for high resolution subtomogram averaging. *J Struct Biol* **197**, 191–198 (2017).
305. Isensee, F., Jaeger, P. F., Kohl, S. A. A., Petersen, J. & Maier-Hein, K. H. nnU-Net: a self-configuring method for deep learning-based biomedical image segmentation. *Nat Methods* **18**, 203–211 (2021).
306. Lamm, L. *et al.* MemBrain v2: an end-to-end tool for the analysis of membranes in cryo-electron tomography. Preprint at <https://doi.org/10.1101/2024.01.05.574336> (2024).
307. Heebner, J. E. *et al.* Deep Learning-Based Segmentation of Cryo-Electron Tomograms. *J Vis Exp* (2022) doi:10.3791/64435.
308. Tegunov, D. & Cramer, P. Real-time cryo-electron microscopy data preprocessing with Warp. *Nat Methods* **16**, 1146–1152 (2019).
309. Zivanov, J. *et al.* New tools for automated high-resolution cryo-EM structure determination in RELION-3. *Elife* **7**, e42166 (2018).
310. Wan, W., Khavnekar, S. & Wagner, J. STOPGAP, an open-source package for template matching, subtomogram alignment, and classification. *bioRxiv* 2023.12.20.572665 (2023) doi:10.1101/2023.12.20.572665.
311. Cruz-León, S. *et al.* High-confidence 3D template matching for cryo-electron tomography. *Nat Commun* **15**, 3992 (2024).
312. Ermel, U. H., Arghittu, S. M. & Frangakis, A. S. ArtiaX: An electron tomography toolbox for the interactive handling of sub-tomograms in UCSF ChimeraX. *Protein Sci* **31**, e4472 (2022).
313. Meng, E. C. *et al.* UCSF ChimeraX: Tools for structure building and analysis. *Protein Sci* **32**, e4792 (2023).

314. Kremer, J. R., Mastronarde, D. N. & McIntosh, J. R. Computer visualization of three-dimensional image data using IMOD. *J Struct Biol* **116**, 71–76 (1996).
315. Neumann, M. *et al.* Phosphorylation of S409/410 of TDP-43 is a consistent feature in all sporadic and familial forms of TDP-43 proteinopathies. *Acta Neuropathol* **117**, 137–149 (2009).
316. Arai, T. *et al.* TDP-43 is a component of ubiquitin-positive tau-negative inclusions in frontotemporal lobar degeneration and amyotrophic lateral sclerosis. *Biochemical and Biophysical Research Communications* **351**, 602–611 (2006).
317. Johnston, J. A., Ward, C. L. & Kopito, R. R. Aggresomes: a cellular response to misfolded proteins. *J Cell Biol* **143**, 1883–1898 (1998).
318. Pérez-Berlanga, M. *et al.* Loss of TDP-43 oligomerization or RNA binding elicits distinct aggregation patterns. *EMBO J* **42**, e111719 (2023).
319. Riemenschneider, H. *et al.* Gel-like inclusions of C-terminal fragments of TDP-43 sequester stalled proteasomes in neurons. *EMBO Reports* **23**, e53890 (2022).
320. Guo, Q. *et al.* In Situ Structure of Neuronal C9orf72 Poly-GA Aggregates Reveals Proteasome Recruitment. *Cell* **172**, 696-705.e12 (2018).
321. Zhao, D. Y. *et al.* Autophagy preferentially degrades non-fibrillar polyQ aggregates. *Molecular Cell* **84**, 1980-1994.e8 (2024).
322. Lambert, J.-P., Tucholska, M., Go, C., Knight, J. D. R. & Gingras, A.-C. Proximity biotinylation and affinity purification are complementary approaches for the interactome mapping of chromatin-associated protein complexes. *J Proteomics* **118**, 81–94 (2015).
323. Branon, T. C. *et al.* Efficient proximity labeling in living cells and organisms with TurboID. *Nat Biotechnol* **36**, 880–887 (2018).

324. Freibaum, B. D., Chitta, R. K., High, A. A. & Taylor, J. P. Global Analysis of TDP-43 Interacting Proteins Reveals Strong Association with RNA Splicing and Translation Machinery. *J. Proteome Res.* **9**, 1104–1120 (2010).
325. Ling, S.-C. *et al.* ALS-associated mutations in TDP-43 increase its stability and promote TDP-43 complexes with FUS/TLS. *Proc. Natl. Acad. Sci. U.S.A.* **107**, 13318–13323 (2010).
326. Blokhuis, A. M. *et al.* Comparative interactomics analysis of different ALS-associated proteins identifies converging molecular pathways. *Acta Neuropathol* **132**, 175–196 (2016).
327. Feneberg, E. *et al.* An ALS-linked mutation in TDP-43 disrupts normal protein interactions in the motor neuron response to oxidative stress. *Neurobiology of Disease* **144**, 105050 (2020).
328. Schreiber, K. J., Kadijk, E. & Youn, J.-Y. Exploring Options for Proximity-Dependent Biotinylation Experiments: Comparative Analysis of Labeling Enzymes and Affinity Purification Resins. *J. Proteome Res.* **23**, 1531–1543 (2024).
329. Lee, Y. *et al.* Keap1/Cullin3 Modulates p62/SQSTM1 Activity via UBA Domain Ubiquitination. *Cell Reports* **19**, 188–202 (2017).
330. Gestaut, D., Limatola, A., Joachimiak, L. & Frydman, J. The ATP-powered gymnastics of TRiC/CCT: an asymmetric protein folding machine with a symmetric origin story. *Curr Opin Struct Biol* **55**, 50–58 (2019).
331. Iguchi, Y. *et al.* I $\kappa$ B kinase phosphorylates cytoplasmic TDP-43 and promotes its proteasome degradation. *Journal of Cell Biology* **223**, e202302048 (2024).
332. Oughtred, R. *et al.* The BioGRID database: A comprehensive biomedical resource of curated protein, genetic, and chemical interactions. *Protein Sci* **30**, 187–200 (2021).

333. Ferrari, V. *et al.* Valosin Containing Protein (VCP): A Multistep Regulator of Autophagy. *Int J Mol Sci* **23**, 1939 (2022).
334. Saha, I. *et al.* The AAA+ chaperone VCP disaggregates Tau fibrils and generates aggregate seeds in a cellular system. *Nat Commun* **14**, 560 (2023).
335. Mackenzie, I. R. A. & Neumann, M. Molecular neuropathology of frontotemporal dementia: Insights into disease mechanisms from postmortem studies. *J Neurochem* **138 Suppl 1**, 54–70 (2016).
336. Mackenzie, I. R. & Neumann, M. Subcortical TDP-43 pathology patterns validate cortical FTLD-TDP subtypes and demonstrate unique aspects of C9orf72 mutation cases. *Acta Neuropathol* **139**, 83–98 (2020).
337. Hiji, M. *et al.* White matter lesions in the brain with frontotemporal lobar degeneration with motor neuron disease: TDP-43-immunopositive inclusions co-localize with p62, but not ubiquitin. *Acta Neuropathol* **116**, 183–191 (2008).
338. Roden, C. & Gladfelter, A. S. RNA contributions to the form and function of biomolecular condensates. *Nat Rev Mol Cell Biol* **22**, 183–195 (2021).
339. Mann, J. R. & Donnelly, C. J. RNA modulates physiological and neuropathological protein phase transitions. *Neuron* **109**, 2663–2681 (2021).
340. Layne, E. [73] Spectrophotometric and turbidimetric methods for measuring proteins. in *Methods in Enzymology* vol. 3 447–454 (Elsevier, 1957).
341. Lightfoot, S., Salowsky, R. & Buhlmann, C. RNA integrity number: towards standardization of RNA quality assessment for better reproducibility and reliability of gene expression experiments. *Breast Cancer Res* **7**, P7.05, bcr1197 (2005).
342. Teyssou, E. *et al.* Novel UBQLN2 mutations linked to amyotrophic lateral sclerosis and atypical hereditary spastic paraplegia phenotype through defective HSP70-mediated proteolysis. *Neurobiol Aging* **58**, 239.e11-239.e20 (2017).

343. Cassel, J. A. & Reitz, A. B. Ubiquilin-2 (UBQLN2) binds with high affinity to the C-terminal region of TDP-43 and modulates TDP-43 levels in H4 cells: characterization of inhibition by nucleic acids and 4-aminoquinolines. *Biochim Biophys Acta* **1834**, 964–971 (2013).
344. Jutzi, D. *et al.* Aberrant interaction of FUS with the U1 snRNA provides a molecular mechanism of FUS induced amyotrophic lateral sclerosis. *Nat Commun* **11**, 6341 (2020).
345. Ayala, Y. M. *et al.* TDP-43 regulates its mRNA levels through a negative feedback loop. *EMBO J* **30**, 277–288 (2011).
346. Rao, S. *et al.* Three-step docking by WIPI2, ATG16L1, and ATG3 delivers LC3 to the phagophore. *Sci. Adv.* **10**, eadj8027 (2024).
347. Buchan, J. R., Kolaitis, R.-M., Taylor, J. P. & Parker, R. Eukaryotic stress granules are cleared by autophagy and Cdc48/VCP function. *Cell* **153**, 1461–1474 (2013).
348. Li, Q., Yokoshi, M., Okada, H. & Kawahara, Y. The cleavage pattern of TDP-43 determines its rate of clearance and cytotoxicity. *Nat Commun* **6**, 6183 (2015).
349. Zhang, Y.-J. *et al.* Aberrant cleavage of TDP-43 enhances aggregation and cellular toxicity. *Proceedings of the National Academy of Sciences* **106**, 7607–7612 (2009).
350. Walker, A. K. *et al.* An insoluble frontotemporal lobar degeneration-associated TDP-43 C-terminal fragment causes neurodegeneration and hippocampus pathology in transgenic mice. *Human Molecular Genetics* **24**, 7241–7254 (2015).
351. Kang, J., Lim, L., Lu, Y. & Song, J. A unified mechanism for LLPS of ALS/FTLD-causing FUS as well as its modulation by ATP and oligonucleic acids. *PLoS Biol* **17**, e3000327 (2019).

352. Thorpe, J. R., Tang, H., Atherton, J. & Cairns, N. J. Fine structural analysis of the neuronal inclusions of frontotemporal lobar degeneration with TDP-43 proteinopathy. *J Neural Transm (Vienna)* **115**, 1661–1671 (2008).
353. Zhao, D. Y. *et al.* Autophagy preferentially degrades non-fibrillar polyQ aggregates. *Mol Cell* **84**, 1980-1994.e8 (2024).
354. Farrawell, N. E. *et al.* Ubiquitin Homeostasis Is Disrupted in TDP-43 and FUS Cell Models of ALS. *iScience* **23**, 101700 (2020).
355. Zhang, Q. *et al.* Suppression of Linear Ubiquitination Ameliorates Cytoplasmic Aggregation of Truncated TDP-43. *Cells* **11**, 2398 (2022).
356. Klaips, C. L., Jayaraj, G. G. & Hartl, F. U. Pathways of cellular proteostasis in aging and disease. *J Cell Biol* **217**, 51–63 (2018).
357. Mauthe, M. *et al.* A chaperone-proteasome-based fragmentation machinery is essential for aggrephagy. *Nat Cell Biol* **27**, 1448–1464 (2025).
358. Herhaus, L. & Dikic, I. Ubiquitin-induced phase separation of p62/SQSTM1. *Cell Res* **28**, 389–390 (2018).
359. Dooley, H. C. *et al.* WIPI2 Links LC3 Conjugation with PI3P, Autophagosome Formation, and Pathogen Clearance by Recruiting Atg12–5-16L1. *Molecular Cell* **55**, 238–252 (2014).
360. Strong, L. M. *et al.* Structural basis for membrane recruitment of ATG16L1 by WIPI2 in autophagy. *Elife* **10**, e70372 (2021).
361. Ichimura, Y. *et al.* Phosphorylation of p62 activates the Keap1-Nrf2 pathway during selective autophagy. *Mol Cell* **51**, 618–631 (2013).
362. Lee, Y. *et al.* Keap1/Cullin3 Modulates p62/SQSTM1 Activity via UBA Domain Ubiquitination. *Cell Rep* **19**, 188–202 (2017).
363. Rasmussen, N. L., Kournoutis, A., Lamark, T. & Johansen, T. NBR1: The archetypal selective autophagy receptor. *J Cell Biol* **221**, e202208092 (2022).

364. Haslbeck, M. & Vierling, E. A first line of stress defense: small heat shock proteins and their function in protein homeostasis. *J Mol Biol* **427**, 1537–1548 (2015).
365. Cristofani, R. *et al.* The Role of HSPB8, a Component of the Chaperone-Assisted Selective Autophagy Machinery, in Cancer. *Cells* **10**, 335 (2021).
366. Meriin, A. B. *et al.* Hsp70-Bag3 complex is a hub for proteotoxicity-induced signaling that controls protein aggregation. *Proc Natl Acad Sci U S A* **115**, E7043–E7052 (2018).
367. Wu, J. J. *et al.* ALS/FTD mutations in UBQLN2 impede autophagy by reducing autophagosome acidification through loss of function. *Proc Natl Acad Sci U S A* **117**, 15230–15241 (2020).
368. Cascella, R., Fani, G., Bigi, A., Chiti, F. & Cecchi, C. Partial Failure of Proteostasis Systems Counteracting TDP-43 Aggregates in Neurodegenerative Diseases. *Int J Mol Sci* **20**, 3685 (2019).
369. Tashiro, Y. *et al.* Motor neuron-specific disruption of proteasomes, but not autophagy, replicates amyotrophic lateral sclerosis. *J Biol Chem* **287**, 42984–42994 (2012).
370. Sedlacek, J. Activation of the 26S Proteasome to Reduce Proteotoxic Stress and Improve the Efficacy of PROTACs. *ACS Pharmacol. Transl. Sci.* **8**, 21–35 (2025).
371. Yuste-Checa, P. *et al.* The extracellular chaperone Clusterin enhances Tau aggregate seeding in a cellular model. *Nat Commun* **12**, 4863 (2021).
372. Nachman, E. *et al.* Disassembly of Tau fibrils by the human Hsp70 disaggregation machinery generates small seeding-competent species. *J Biol Chem* **295**, 9676–9690 (2020).

373. Weiss-Sadan, T. *et al.* NRF2 activation induces NADH-reductive stress, providing a metabolic vulnerability in lung cancer. *Cell Metabolism* **35**, 722 (2023).
374. Kleijnen, M. F. *et al.* The hPLIC proteins may provide a link between the ubiquitination machinery and the proteasome. *Mol Cell* **6**, 409–419 (2000).
375. Deng, H.-X. *et al.* FUS-immunoreactive inclusions are a common feature in sporadic and non-SOD1 familial amyotrophic lateral sclerosis. *Ann Neurol* **67**, 739–748 (2010).
376. Matthews, A. M. & Whiteley, A. M. UBQLN2 in neurodegenerative disease: mechanistic insights and emerging therapeutic potential. *Biochem Soc Trans* **53**, 823–833 (2025).
377. Kampinga, H. H. & Craig, E. A. The HSP70 chaperone machinery: J proteins as drivers of functional specificity. *Nat Rev Mol Cell Biol* **11**, 579–592 (2010).

## 12. Curriculum Vitae

### Personal Information

Yongwon Suk

An der Schmidtsei 8a

Taunusstein 65232, Germany

(+49) 17634497852

Ysuk7154@gmx.de



**Date of Birth:** 10.03.1993

**Nationality:** South Korea

### Education & Training

04/2021 – present

**PhD Candidate – Molecular Biology and Neuroscience (Dormann Lab)**

*Johannes Gutenberg University Mainz / Institute of Molecular Biology (IMB), Mainz*

Research on Degradation of pathogenic TDP-43 condensates in neurodegenerative diseases

10/2016 – 11/2019

**Biochemistry and Biophysics Master's program student**

*Albert-Ludwigs-Universität Freiburg*

03/2019 – 10/2019

**Master Thesis (grade: 1.0) in Biochemistry and Molecular Biology (Jiou Wang Lab)**

*Johns Hopkins University, Bloomberg School of Public Health*

	Research on Characterization of a novel autophagy regulator
06/2018 – 10/2019	<p><b>Visiting Scholar at Johns Hopkins Bloomberg School of Public Health</b></p> <p>Research on Protein Quality Control</p>
01/2016 – 04/2016	<p><b>Bachelor Thesis at the Institute of Organic Chemistry (Tanja Weil Lab)</b></p> <p><i>Ulm University</i></p> <p>‘Functional DNA Design, Purification and Application’, dealing with biorthogonal protein modifications, synthetic oligonucleotide-protein hybrids and synthetic fusion proteins</p>
10/2012 – 04/2016	<p><b>Biochemistry Bachelor’s program student</b></p> <p><i>Ulm University</i></p>
09/2004 – 07/2012	<p><b>Higher Education Entrance Qualification (Abitur)</b></p> <p><i>Salier-Gymnasium, Waiblingen</i></p>
<b>Work Experience</b>	
08/2016 – 03/2017	<p><b>Voluntary Internship – Boehringer Ingelheim</b></p> <p><i>Department of Pharmaceutical Development Biologicals, Group Early Stage I (Biberach an der Riß)</i></p> <p>Working on Protein Purification (HPLC (SEC, IEC)), Lyophilization</p>

## Technical Skills

Process and physico-chemical Characterization (protein stability, osmotic virial coefficient, DLS, DSC etc.)

**Programming Language:** Python, R

**Imaging:** Live-cell Imaging, High-content microscopy, Confocal microscopy

**Image Analysis:** Harmony, Ilastik, Arivis, Napari, Zeiss Zen, Cellpose, Fiji/ImageJ

**Omics & Data Analysis:** Proximity Labeling Proteomics,

**Molecular Biology:** CRISPR, cloning

**Biochemical Assays:** Western blotting, Immunoprecipitation, Protein degradation assays

## Publications

Liu Y, Wang T, Ji YJ, et al. A C9orf72-CARM1 axis regulates lipid metabolism under glucose starvation-induced nutrient stress. *Genes Dev.* 2018;32(21-22):1380-1397. doi:10.1101/gad.315564.118

Strohm L, Hu Z, Suk Y, et al. Multi-omics profiling identifies a deregulated FUS-MAP1B axis in ALS/FTD-associated UBQLN2 mutants. *Life Sci Alliance.* 2022;5(11):e202101327. Published 2022 Jul 1. doi:10.26508/lsa.202101327

## Conference Attendance

**Integrating the molecular, mechanistic and physiological diversity of autophagy (2022 - Eger, Hungary)**

Poster presentation

**3<sup>rd</sup> Frankfurt Conference on Quality Control in Life Processes (2022 – Frankfurt, Germany)**

**Arturo Falaschi Conference on TDP-43 function and dysfunction in disease (2023 – Trieste, Italy)**

Poster presentation

**AD/PD™ 2024 Alzheimer’s & Parkinson’s Diseases Conference (2024 – Lisbon, Portugal)**

Poster presentation

**Autophagy across scales (2024 – Sorrento, Italy)**

Poster presentation

Flash Talk

**Language Skills**

German native speaker

Korean native speaker

English fluent

**Personal Information**

Youth team volleyball player from 2002 – 2011 at the club SC Korb competing in the leagues D-Jugend, C-Jugend, B-Jugend and A-Jugend

Passionately working out in a gym 5 times a week since 2016

Competitive Athlete in Brazilian Jiu-Jitsu